The Astrophysical Journal, 717:289–322, 2010 July 1 doi:10.1088/0004-637X/717/1/289

THE STRUCTURE AND KINEMATICS OF THE CIRCUMGALACTIC MEDIUM FROM FAR-ULTRAVIOLET SPECTRA OF $z \simeq 2$–3 GALAXIES*

Charles C. Steidel[1], Dawn K. Erb[2,8], Alice E. Shapley[3,9,10], Max Pettini[4,5], Naveen Reddy[6,11], Milan Bogosavljević[1], Gwen C. Rudie[1], and Olivera Rakic[7]

[1] California Institute of Technology, MS 249-17, Pasadena, CA 91125, USA
[2] Department of Physics, University of California Santa Barbara, Santa Barbara, CA 93106, USA
[3] Department of Physics and Astronomy, University of California Los Angeles, 430 Portola Plaza, Box 951547, Los Angeles, CA 90095, USA
[4] Institute of Astronomy, Madingley Road, Cambridge CB3 OHA, UK
[5] International Centre for Radio Astronomy Research, University of Western Australia, 35 Stirling Highway, Crawley, WA 6009, Australia
[6] National Optical Astronomy Observatories, 950 North Cherry Avenue, Tucson, AZ 85258, USA
[7] Leiden Observatory, Leiden University, P.O. Box 9513, 2300 RA Leiden, The Netherlands
Received 2010 February 22; accepted 2010 May 11; published 2010 June 10

ABSTRACT

We present new results on the kinematics and spatial distribution of metal-enriched gas within ∼125 kpc of star-forming ("Lyman break") galaxies at redshifts $2 \lesssim z \lesssim 3$. In particular, we focus on constraints provided by the rest-frame far-ultraviolet (far-UV) spectra of faint galaxies, and demonstrate how galaxy spectra can be used to obtain key spatial and spectral information more efficiently than possible with QSO sightlines. Using a sample of 89 galaxies with $\langle z \rangle = 2.3 \pm 0.3$ and with both rest-frame far-UV and Hα spectra, we re-calibrate the measurement of accurate galaxy systemic redshifts using only survey-quality rest-UV spectra. We use the velocity-calibrated sample to investigate the kinematics of the galaxy-scale outflows via the strong interstellar (IS) absorption lines and Lyα emission (when present), as well as their dependence on other physical properties of the galaxies. We construct a sample of 512 close (1″–15″) angular pairs of $z \sim 2$–3 galaxies with redshift differences indicating a lack of physical association. Sightlines to the background galaxies provide new information on the spatial distribution of circumgalactic gas surrounding the foreground galaxies. The close pairs sample galactocentric impact parameters 3–125 kpc (physical) at $\langle z \rangle = 2.2$, providing for the first time a robust map of cool gas as a function of galactocentric distance for a well-characterized population of galaxies. We propose a simple model of circumgalactic gas that simultaneously matches the kinematics, depth, and profile shape of IS absorption and Lyα emission lines, as well as the observed variation of absorption line strength (H I and several metallic species) versus galactocentric impact parameter. Within the model, cool gas is distributed symmetrically around every galaxy, accelerating radially outward with $v_{\rm out}(r)$ increasing with r (i.e., the highest velocities are located at the largest galactocentric distances r). The inferred radial dependence of the covering fraction of cool gas (which modulates the absorption line strength) is $f_c(r) \propto r^{-\gamma}$ with $0.2 \lesssim \gamma \lesssim 0.6$ depending on transition. We discuss the results of the observations in the context of "cold accretion," in which cool gas is accreting via filamentary streams directly onto the central regions of galaxies. At present, we find little observational evidence for cool infalling material, while evidence supporting the large-scale effects of superwind *outflows* is strong. This "pilot" study using faint galaxy spectra demonstrates the potential of using galaxies to trace baryons within galaxies, in the circumgalactic medium, and ultimately throughout the intergalactic medium.

Key words: cosmology: observations – galaxies: evolution – galaxies: high-redshift

Online-only material: color figures

1. INTRODUCTION

Observational studies of the galaxy formation process are reaching a critical juncture, where the accumulation rate of new data may be overtaking our ability to reach new understanding. There are now many large surveys designed to study galaxy formation and evolution over ever-increasing volumes and redshift ranges, backed by the unquestionable power of multiwavelength observations from X-rays to the far-infrared (far-IR)/submillimeter and radio. Interpretation of survey data is aided by a multitude of theoretical results based on simulations and/or semi-analytic calculations. However, many of the most fundamental remaining questions in galaxy formation involve complex baryonic processes that are difficult to model, are not well constrained by current observations, or involve physics that are not yet well understood.

While there is general agreement about the development of structure in the dark matter component on scales larger than that of galaxies, the astrophysics of the baryonic response to the dark matter structure, the subsequent feedback of energy from star formation, supernova explosions, and accretion energy from the growth of supermassive black holes, and the flow of gas into and out of galaxies, remain largely unconstrained—and thus subject to substantial debate. "Feedback" has become a buzzword, universally acknowledged as something important to understand, but there is little agreement about what it really means and how it affects the "big picture." Nevertheless, some kind of feedback is invoked to explain many otherwise-

* Based on data obtained at the W. M. Keck Observatory, which is operated as a scientific partnership among the California Institute of Technology, the University of California, and NASA, and was made possible by the generous financial support of the W. M. Keck Foundation.
[8] Spitzer Fellow.
[9] Alfred P. Sloan Fellow.
[10] Packard Fellow.
[11] Hubble Fellow.

inexplicable observations: the cessation of star formation in massive galaxies at high redshift; the small number of low-mass galaxies relative to the dark matter halo mass function predicted by the otherwise successful ΛCDM cosmology; the correlation between galaxy spheroid mass and the mass of central supermassive black holes; the general absence of cooling flows in clusters of galaxies; and the metal enrichment of intracluster gas, just to name a few. The most obvious sources of the energy and/or momentum required to explain these phenomena are massive stars, supernovae, and active galactic nucleus (AGN) activity, all of which must have exerted most of their influence in the distant past, when these processes were at their peak intensity.

One route to understanding the relevant baryonic processes is via simultaneous study of galaxies and the intergalactic medium (IGM), in the same cosmic volumes during the epoch when they were arguably exerting the greatest influence on one another—near the peak of both universal star formation and supermassive black hole growth in the redshift range $3 \gtrsim z \gtrsim 1.5$. Combining two powerful lines of investigation provides complementary information on the state of baryons, both those collapsed into galaxies and those residing outside of galaxies. The IGM and "circumgalactic medium" (CGM; by which we mean the gas-phase structures found within $\lesssim$300 kpc (physical) of galaxies) together present a laboratory in which the effects of galaxy formation and AGN accretion (e.g., radiative and hydrodynamical "feedback" and its recent history) can be measured on scales that are not accessible using direct observations of galaxies. Similarly, galaxy distribution relative to the lines of sight to background objects tells us more about how the physical information garnered from the absorption line studies should be interpreted. These ambitious science goals—to observe both diffuse gas and galaxies/AGNs in the same survey volume at high fidelity and down to small scales—require a different approach compared to most spectroscopic surveys of the distant universe. Whereas the movement of most galaxy surveys has been toward larger and larger scales, the most vexing remaining uncertainties are related to phenomena occurring on ∼1–10 Mpc scales, where the figure of merit is *information density* and not total survey volume.

It has been known for some time that galactic-scale outflows with velocities of several hundred km s^{-1} are ubiquitous in star-forming galaxies at all redshifts for which interstellar (IS) absorption features are accessible (e.g., Steidel et al. 1996; Franx et al. 1997; Pettini et al. 2000, 2001; Shapley et al. 2003; Martin 2005; Rupke et al. 2005; Tremonti et al. 2007; Weiner et al. 2009). Evidence is found in the offsets between the redshifts of the nebular emission lines, IS absorption lines, and Lyα emission (Pettini et al. 2001), in the relative velocities of stellar, IS, and nebular lines in composite ultraviolet (UV) spectra (Shapley et al. 2003), and in the correlation of C IV systems seen in absorption in QSO spectra with the positions of the galaxies themselves (Adelberger et al. 2003, 2005a). The outflowing gas has been observed in detail for only a handful of lensed galaxies (Pettini et al. 2002; Quider et al. 2009, 2010); in the best observed of these, MS1512-cB58, the IS absorption is distributed over a very wide range of velocities, $-800\,\mathrm{km\ s^{-1}} \lesssim v \lesssim +200\,\mathrm{km\ s^{-1}}$, with a centroid velocity of -255 km s^{-1} (Pettini et al. 2002). Such outflows are also a general feature of starburst galaxies in the local universe, where rest-UV spectroscopic studies reveal similarly complex velocity structure and gas in multiple phases (e.g., Heckman et al. 1990; Lehnert & Heckman 1996; Martin 1999; Strickland et al. 2004; Schwartz et al. 2006; Grimes et al. 2009; Chen et al. 2010). However, the outflow phenomenon is so much more widespread at high redshifts that it is influencing essentially *every* galaxy, and potentially every galaxy's local environment. It must have an influence on both the chemical evolution of the galaxies and of the IGM, it may well regulate the maximum star formation rate (SFR) attainable by a galaxy, and without doubt it is an essential ingredient to basic understanding of the circulation of baryons as galaxies are forming.

In spite of the substantial observational evidence for galaxy-scale outflows, most of the recent theoretical work has focused instead on the *infall* of cool gas ("Cold Accretion" or "Cold Flows") via filaments, directly onto the central regions of forming galaxies. According to much of the recent work, this mode of gas accretion is what feeds (and regulates) high SFRs in high-redshift galaxies until they attain a particular mass threshold ($M_{\rm tot} \gtrsim 10^{12}\,M_{\odot}$) at which point virial shocks develop and accretion of cold material is suppressed (Kereš et al. 2005, 2009; Dekel et al. 2009; Brooks et al. 2009; Ceverino et al. 2010). This transition is believed to be at least partially responsible for producing massive "red and dead" galaxies as early as $z \sim 2.5$. Similarly, the phenomenon of spatially extended Lyα emission, including giant Lyα "blobs" (Steidel et al. 2000) has been ascribed to cooling radiation from the denser portions of the cold streams as they are accreting directly onto the galaxy's central regions (e.g., Haiman et al. 2000; Furlanetto et al. 2005; Dijkstra & Loeb 2009; Goerdt et al. 2009). Although the cold accretion picture may be attractive, the predictions of the observational consequences for CGM gas are rather model-dependent for both absorption lines and Lyα emission. The simulations which predict cold accretion generally do not account for IS gas that may have been carried to large galactocentric radii by outflows, nor for Lyα photons produced by photoionization in a galaxy's H II regions which then scatter their way in space through CGM gas before escaping. It may well be that the observational signatures of infall by cold accretion and outflows via supernova-driven winds are very subtle, and perhaps indistinguishable. Possibly the most telling differences would be kinematic—absorption line signatures of infalling material in galaxy spectra would be expected to be primarily *redshifted*, while outflowing material would be blueshifted and could reach much higher velocities with respect to the galaxy systemic redshift. Thus, accurate determination of the galaxy systemic redshift is an essential part of understanding the nature of the CGM.

The *spatial* distribution of the blueshifted high-velocity material seen in absorption against the galaxy continuum is not yet established. We know that virtually every $z > 2$ galaxy bright enough to be observed spectroscopically is driving out material at velocities of at least several hundred km s^{-1}, but we do not know how far this material travels, or even where it is with respect to the galaxy as we observe it. The mass flux associated with such flows has been measured in only one case at high redshift, MS1512-cB58 (Pettini et al. 2000), and even in this case the result depends very sensitively on the assumed physical location of the absorbing material responsible for the bulk of the observed absorption. The best hope for constraining the location of outflowing gas is by observing objects lying in the background, but at small angular separation, relative to the galaxy of interest. In this case, the challenge is to find background objects bright enough in the rest-frame far-UV but close enough to the foreground galaxy to provide interesting constraints. A great deal of effort, over a large range of redshifts,

has been invested using QSOs as background sources, where absorption by metallic ions or H I in the spectrum of the QSO is compared with galaxies with known redshifts and projected separations (e.g., Bergeron & Boissé 1991; Steidel et al. 1994, 2002; Chen et al. 2001; Lanzetta et al. 1995; Danforth & Shull 2008; Bowen et al. 1995; Bouché et al. 2007; Kacprzak et al. 2010); most of this work has focused on redshifts $z < 1$ because of the increasing difficulty obtaining spectra of the foreground galaxies at higher redshifts. Even if galaxies are identified and have redshifts that correspond closely with observed absorption, the association of particular absorption systems with identified galaxies is almost always ambiguous, since the dynamic range for identifying faint galaxies is limited, and often the bright background QSOs make it challenging to observe galaxies within a few arcsec of the QSO sightline. Finally, there is the controversial issue of whether metals seen near, but outside of, galaxies are a direct result of recent star formation or AGN activity, or are simply tracing out regions of the universe in which some galaxies, perhaps in the distant past, polluted the gas with metals (e.g., Madau et al. 2001; Scannapieco et al. 2002; Mori et al. 2002; Ferrara 2003; cf. Adelberger et al. 2003, 2005a).

In this paper, our goal is to try to understand the spatial distribution of cool gas seen in absorption against the stellar continuum of every galaxy observed at high redshift. The objective is to empirically track the kinematics and structure in the CGM from the central parts of galaxies all the way to large galactocentric radii. In this work, we use only galaxy spectra, primarily in the rest-frame far-UV, but we calibrate the velocity zero-point using a set of nearly 100 Hα measurements in the observed-frame near-IR for galaxies in the redshift range $1.9 \lesssim z \lesssim 2.6$. The near-IR measurements are drawn primarily from the sample of Erb et al. (2006c), after which we use a much more extensive set of rest-UV spectra from a nearly completed UV-selected galaxy survey targeting the same range of redshifts.

The paper is organized as follows: in Section 2 we examine the statistics of the kinematics of the outflows using a subsample of galaxies for which both near-IR nebular Hα spectroscopy and reasonably high-quality optical (rest-UV) spectra are available. We also present new empirical formulae for estimating galaxy systemic redshifts for the typical case in which only low signal-to-noise ratio (S/N) rest-UV spectra are available. In Section 3, we seek correlations between the IS absorption line kinematics, in particular the bulk velocities measured from strong low-ionization transitions, and other measured galaxy properties. Section 4 describes further inferences on the structure and kinematics of outflowing material from high S/N composite far-UV spectra, while Section 5 examines the observed behavior of Lyα emission and its relationship to the IS absorption features, and attempts to understand the observations with simple models. We introduce in Section 6 the use of close angular pairs of galaxies at different redshifts for mapping the spatial distribution of the circumgalactic gas around the foreground galaxies, while Section 7 develops a simple geometrical and kinematic model for outflows consistent with both the line profiles in galaxy spectra and the larger-scale distribution of gas in the CGM. Section 8 discusses the observational results and their interpretation in the context of the models, and Section 9 summarizes the conclusions and discusses the prospects for improvement in the future.

We assume a ΛCDM cosmology with $\Omega_m = 0.3$, $\Omega_\Lambda = 0.7$, and $h = 0.7$ throughout, unless specified otherwise.

2. BULK OUTFLOW VELOCITIES ASSOCIATED WITH $z \sim 2$–3 GALAXIES

2.1. Spectra in the Hα Galaxy Sample

The rest-frame far-UV spectra of star-forming galaxies include numerous absorption features which (in principle) provide detailed information on the young OB stars responsible for the bright continuum, as well as the IS and circumgalactic atomic and ionized gas associated with the galaxy (see, e.g., Pettini et al. 2000, 2002). The strongest stellar features are due to stellar winds from massive stars, producing broad P-Cygni profiles in higher-ionization lines such as N V λλ1238,1242, C IV λλ1548,1550, and Si IV λλ1393, 1402. The absorption is broad ($\Delta v \gtrsim 2000$ km s^{-1}) and shallow, with depth dependent on the metallicity of the O-stars. Photospheric lines from the same OB stars are also present, but the lines are generally much weaker than the wind features, and so can be difficult to discern in the spectra of individual high-redshift galaxies. The IS lines are superposed on the integrated stellar spectrum, where absorption features of abundant species (e.g., H I, O I, C II, C IV, Si II, Si III, Si IV, Fe II, Al II) can be extremely strong—strong enough to be useful for redshift identification in low S/N spectra. Unfortunately, the most accessible absorption features—the IS and wind features—are not useful for accurate measurements of galaxy redshifts because of the non-gravitational origin of their kinematics. Similarly, Lyα emission, which is observed in ≃50% of a continuum-selected sample at $z \sim 2$–3 (e.g., Shapley et al. 2003; Steidel et al. 2004; Kornei et al. 2010) is resonantly scattered, altering the emergent kinematics in a manner that depends on both the optical depth and velocity distribution of the gas doing the scattering.

Fortunately, nebular emission lines originating in a galaxy's H II regions are also relatively accessible observationally, with the strongest lines (e.g., Hα, Hβ, [O III]) found in the observed-frame near-IR at the redshifts of interest. The Hα line, which is not resonantly scattered and whose strength is strongly dependent on both the ionizing UV radiation field and the density, is likely to provide a reasonable estimate of the systemic redshift of the stars, as well as a measure of gravitationally induced motion within the galaxy (Pettini et al. 2001; Erb et al. 2006c). The only disadvantage of the nebular spectra is that their numbers are currently small in comparison with the available rest-UV spectra.

The quality of rest-UV survey spectra for typical high-redshift galaxies is generally not sufficient for detailed spectral analysis, and so much of what we know about general trends between spectral properties and other physical parameters of galaxies is based on composites (e.g., Steidel et al. 2001; Shapley et al. 2003; Erb et al. 2006a). In order to form these composites for the far-UV spectra, one must assume a relationship between the velocities of measured spectral features and the object's systemic redshift $z_{\rm sys}$; as discussed above, this task is made difficult by the fact that the strong lines of resonance transitions in the far-UV are seldom closer than a few hundred km s^{-1} to the objects' true redshifts.

With the current, enlarged sample of $z \sim 2$ galaxies, including generally higher-quality UV spectra than available in the past, we revisit the measurement of galaxy systemic redshifts using far-UV spectral features, building on previous results (Pettini et al. 2001; Adelberger et al. 2003, 2005a). In this section, we examine in detail the relationship between observed far-UV IS lines, Lyα emission, and the redshifts defined by the Hα line

in the rest-frame optical, including careful attention to possible systematic errors.

The redshifts (both Hα and UV-based) for all but eight of the galaxies have been presented in Erb et al. (2006c), where the observations are described in detail. The new Hα spectra were obtained in the same manner using NIRSPEC (McLean et al. 1998) in 2005 June. Using a 0.″76 entrance slit, the typical spectral resolution achieved with NIRSPEC is $R \simeq 1400$, or FWHM $\simeq$ 215 km s^{-1}, so that the typical Hα line widths of $\sigma_v \sim 100$ km s^{-1} (FWHM $\simeq$ 240 km s^{-1}) are marginally resolved. The rest-UV spectra were obtained with the LRIS-B spectrograph on the Keck 1 telescope, primarily using a 400 line mm^{-1} grism blazed at 3400 Å with a dichroic beam splitter sending all wavelengths $\lambda < 6800$ Å into the blue channel, as described in Steidel et al. (2004). As discussed in detail below, the typical effective spectral resolution achieved in this mode is $\simeq$370 km s^{-1} (FWHM), or $\sigma_{\rm res} \simeq 160$ km s^{-1}.

For objects whose UV spectra show detectable IS absorption lines, we have included only those measurements deemed to be of sufficient quality to yield reasonably precise measurements. We have also excluded the handful of objects from the Erb et al. (2006c) sample with $z < 1.9$ in order to avoid systematic biases caused by differential atmospheric refraction (discussed below), and to focus on the redshift range for which we have the highest-quality ancillary data.

The resulting Hα sample consists of a total of 89 galaxies with $\langle z \rangle = 2.27 \pm 0.16$, of which 48 (54%) have UV spectra in which only an IS absorption line redshift was measured, 38 (43%) have measurements of both Lyα emission and IS absorption, and 3 (3.5%) have only Lyα emission redshifts measured. These fractions are comparable to those obtained from the full spectroscopic sample of $\simeq$1600 galaxies in the same range of redshifts, $1.9 \leqslant z \leqslant 2.6$ (see Steidel et al. 2004). Most (87%) of the galaxies in the parent sample satisfy the "BX" photometric selection criteria (Adelberger et al. 2004; Steidel et al. 2004), with the remainder satisfying the "MD" color criteria defined in Steidel et al. (2003). These galaxies selected on the basis of their UV color have been shown to include all but the dustiest star-forming galaxies in the redshift range of interest (Adelberger & Steidel 2000; Reddy et al. 2008).

2.2. Redshift Uncertainties

As discussed in detail by Shapley et al. (2003), a large number of IS absorption lines is commonly observed in far-UV spectra of star-forming galaxies. In general, all of the detected lines are used to verify that the assigned redshift is correct, but the positions of only three lines, C II λ1334.53, Si IV λ1393.76, and Si II λ1526.72, have been used to measure $z_{\rm IS}$. Of the strong resonance lines in the rest-wavelength range 1000–1600 Å (the range in common for almost all of the spectra discussed in this paper), these lines are the least likely to be blended with other strong lines and most likely to yield a consistent measure of $z_{\rm IS}$. Clearly, the accuracy of each measurement of $z_{\rm IS}$ depends on the strength and width of the lines, and on the quality of the spectra. The S/N of the spectra used for the current study varies considerably. Empirically, from internal agreement of different absorption lines in the same spectrum, and from repeated measurements of the same galaxy on different slitmasks, we estimate that the typical measurement uncertainties are ∼100 km s^{-1} for $z_{\rm IS}$ redshifts and ∼50 km s^{-1} for $z_{{\rm Ly}\alpha}$.

Unfortunately, systematic uncertainties can be more difficult to quantify. For example, the measured wavelengths of features depend on the illumination of the spectrograph slit by the object, whereas the wavelength solutions are determined from calibration lamps and night sky spectra which illuminate the 1.″2 slits uniformly. This source of error can also be wavelength-dependent due to the effects of differential atmospheric refraction. The features used for redshift measurement generally fall in the observed wavelength range ∼3750–5200 Å for the Hα sample considered here, with $\langle z_{\rm H\alpha} \rangle = 2.27 \pm 0.16$. Over this wavelength range, the differential refraction[12] would be ∼0.″7 at an airmass of $\sec z = 1.3$. Slitmasks were almost always observed within ∼10°–15° of the parallactic angle when the airmass was significantly different from 1.0, but even so, the amplitude of differential refraction perpendicular to the slit could be as large as ∼0.″2, which could map into a velocity shift of up to $\sim \pm 75$ km s^{-1} depending on the seeing and the spatial profile of the galaxy.

The measurements of $z_{\rm H\alpha}$ are subject to a different set of systematic uncertainties. Differential refraction in the near-IR is negligible for our purposes, but the observations were obtained using a 0.″76 slit after applying a blind offset from a nearby star to the position of the galaxy measured from either an optical or near-IR continuum image (see Erb et al. 2003, 2006c). While the observations were taken in a way that should minimize any systematic offsets in the resulting $z_{\rm H\alpha}$ due to pointing or astrometric inaccuracies, they of course measure the velocity of only the flux that entered the slit. Empirically, we found that repeated observations of the same galaxy (using different slit position angles) suggest an accuracy of ±60 km s^{-1} for $z_{\rm H\alpha}$ (rms), with the largest excursions from consistency applying to objects known to be spatially extended. Another direct comparison of the redshifts for 14 objects from the NIRSPEC sample of Erb et al. (2006c) is provided by observations of the same objects with the integral-field spectrometer SINFONI at the Very Large Telescope (Förster Schreiber et al. 2006). The SINFONI redshifts are based on the velocity centroid of all detected Hα flux from the object, and are not affected significantly by pointing errors or by slit losses. This comparison shows a level of agreement similar to our estimate from multiple observations with NIRSPEC: $\langle z_N - z_S \rangle = -34 \pm 59$ km s^{-1} (rms), where z_N is the NIRSPEC redshift and z_S is the SINFONI redshift. The average offset is marginally significant ($\simeq 2\sigma$), but the scatter is consistent with our NIRSPEC experience. Eleven of the galaxies in the present Hα sample were also observed using OSIRIS with Laser Guide Star Adaptive Optics (LGSAO) on the Keck 2 telescope (Law et al. 2009); the average redshift difference $z_N - z_O = 8 \pm 41$ km s^{-1}, indicating no evidence for a systematic difference.

In summary, adopting an uncertainty in $z_{\rm H\alpha}$ of 60 km s^{-1}, the typical uncertainties in the measured values of $\Delta v_{\rm IS} = c(z_{\rm IS} - z_{\rm H\alpha})/(1 + z_{\rm H\alpha})$ and $\Delta v_{{\rm Ly}\alpha} = c(z_{{\rm Ly}\alpha} - z_{\rm H\alpha})/(1 + z_{\rm H\alpha})$ for a given galaxy are ∼130 km s^{-1} and ∼90 km s^{-1}, respectively.

2.3. Sample Statistics

Figure 1 shows a histogram of the IS and Lyα emission velocities with respect to the systemic redshift defined by $z_{\rm H\alpha}$. The distributions have $\langle \Delta v_{\rm IS} \rangle = -164 \pm 16$ km s^{-1} and $\langle \Delta v_{{\rm Ly}\alpha} \rangle = 445 \pm 27$ km s^{-1}, where the quoted uncertainties are errors in the mean. Figure 2 illustrates the same sample as in

[12] All of the spectroscopic observations of the Hα sample were obtained before the commissioning of the Cassegrain ADC on Keck 1. We are excluding for the moment galaxies at redshifts where key features fall at wavelengths shorter than 3750 Å due to the rapidly increasing amplitude of differential refraction.

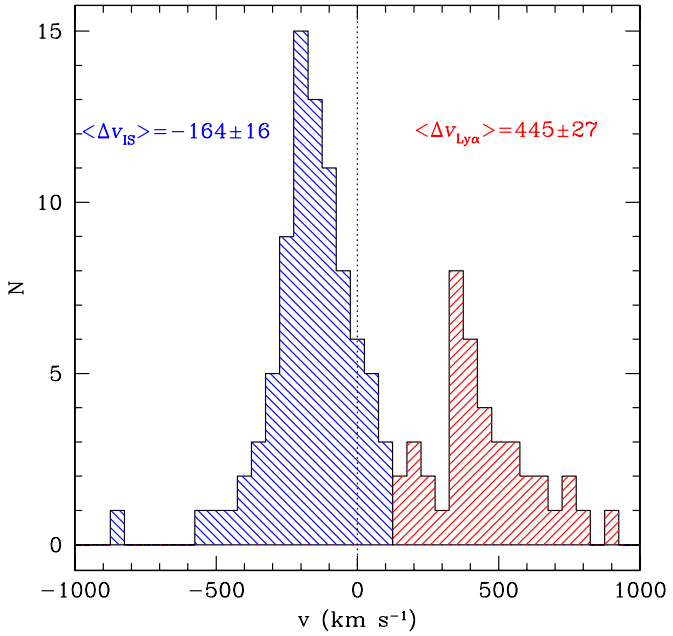

Figure 1. Histogram of the measured (centroid) velocities of IS absorption lines (blue) and Lyα emission (red) with respect to the galaxy nebular redshift as defined by the centroid of the Hα emission line, for a sample of 89 galaxies with $\langle z \rangle = 2.27 \pm 0.16$. The sample includes only those galaxies having both nebular line redshifts and rest-UV spectra of adequate quality to measure absorption line centroids. In this sample, 86 of the 89 galaxies have measured values of $z_{\rm IS}$, 3 have only $z_{\rm Ly\alpha}$, and 39 have both. The mean values of the velocity offsets are indicated.

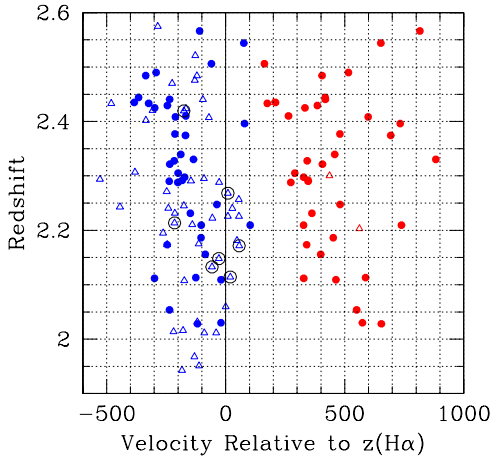

Figure 2. Plot showing the IS absorption line centroid velocities (blue) and centroid Lyα emission velocities relative to the redshift defined by Hα for the same sample as in Figure 1. Galaxies for which both IS absorption redshifts and Lyα emission redshifts are available are indicated with blue (absorption) and red (emission) solid dots; open triangles show systems for which one or the other measurements are not available. The circled objects are ones which exhibited measurable velocity shear in the sample of Erb et al. (2006c; see the text for discussion).

Figure 1, where different symbols are used depending on the UV spectral morphology of the galaxies.

In light of the current Hα sample of $z \sim 2.3$ galaxies, it is worth re-examining the "rules" that one would use to estimate the true systemic redshift of the galaxies given only information contained in their rest-UV spectra, and assuming that $z_{\rm H\alpha}$ defines the rest frame. Using a linear regression form similar to that used by Adelberger et al. (2005a), for galaxies with both $z_{\rm Ly\alpha}$ and $z_{\rm IS}$ measurements,

$$z_{\rm H\alpha} = z_{\rm IS} + 0.00289 - 0.0026(2.7 - z_{\rm IS});\ \sigma_z = 0.00127, \quad (1)$$

$$z_{\rm H\alpha} = z_{\rm Ly\alpha} - 0.0054 + 0.0001(2.7 - z_{\rm Ly\alpha});\ \sigma_z = 0.00193, \quad (2)$$

corresponding to velocity offsets of $\Delta v_{\rm IS} = -170 \pm 115$ km s^{-1} and $\Delta v_{\rm Ly\alpha} = +485 \pm 175$ km s^{-1}, respectively, at the mean redshift of $z_{\rm H\alpha} = 2.27$. For objects with a measurement of $z_{\rm IS}$ only,

$$z_{\rm H\alpha} = z_{\rm IS} + 0.00303 - 0.0031(2.7 - z_{\rm IS});\ \sigma_z = 0.00145, \quad (3)$$

or $\Delta v_{\rm IS} = -165 \pm 140$ km s^{-1} (error is the standard deviation) at the mean redshift of the sample.

Using all 86 Hα galaxies with measured $z_{\rm IS}$, the best-fit single relation of the form in Equations (1)–(3) is

$$z_{\rm H\alpha} = z_{\rm IS} + 0.00299 - 0.00291(2.7 - z_{\rm IS});\ \sigma_z = 0.00138 \quad (4)$$

or $\Delta v_{\rm IS} = -166 \pm 125$ km s^{-1} at $\langle z_{\rm H\alpha} \rangle = 2.27$. We find that including $z_{\rm Ly\alpha}$ in the above regression formulae increases the rms redshift uncertainty over that obtained using only $z_{\rm IS}$, in contrast to similar estimates at somewhat higher redshift by Adelberger et al. (2005a). One possible explanation for the difference could be the generally weaker Lyα lines in the $z \simeq 2.3$ sample compared to that at $z \simeq 3$ (Reddy et al. 2008). We return in Section 5 to a discussion of the kinematics of the Lyα emission line. In any case, using only the absorption redshift, with a constant offset of $\simeq$+165 km s^{-1}, would provide an estimate of $z_{\rm H\alpha}$ accurate to $\sim$125 km s^{-1} (rms).

There are too few objects (3 of 89) in the Hα sample having only $z_{\rm Ly\alpha}$ to define a significant relationship for such objects (which are also quite rare in the full $z \gtrsim 2$ spectroscopic sample), although these three objects have $\langle \Delta v_{\rm Ly\alpha} \rangle = 400 \pm 183$, consistent with Equation (2) above. For this reason, we use Equation (2) for subsequent estimates of $z_{\rm H\alpha}$ when only Lyα emission is available.

Figures 1 and 2 show that a significant fraction of the galaxies have an IS absorption line centroid velocity shift $\Delta v_{\rm IS}$ consistent with zero. Given the uncertainties in $\Delta v_{\rm IS}$, this is not particularly significant for individual objects, but we discuss the issue further because of the intriguing behavior of $\Delta v_{\rm IS}$ and $\Delta v_{\rm Ly\alpha}$ with respect to one another and because of the greater significance of the result in higher S/N composite spectra discussed below. Three of the eleven galaxies with measured $\Delta v_{\rm IS} \geqslant 0$ also have Lyα emission, and have $\langle \Delta v_{\rm Ly\alpha} \rangle = +708 \pm 50$ km s^{-1}, $\sim$250 km s^{-1} higher than the average of the full sample; however, the average $\langle \Delta v_{\rm Ly\alpha} - \Delta v_{\rm IS} \rangle = 622 \pm 40$ km s^{-1} for this set of objects is nearly identical to that of the full sample. The relative consistency of the difference $\Delta v_{\rm Ly\alpha} - \Delta v_{\rm IS}$ in the Hα sample, as well as in much larger samples without the benefit of Hα spectroscopy (e.g., Shapley et al. 2003; Steidel et al. 2004), suggests a situation in which $\Delta v_{\rm Ly\alpha}$ moves in concert with $\Delta v_{\rm IS}$ irrespective of whether the centroid of the absorption line velocities are blueshifted with respect to systemic.

Interestingly, three other galaxies out of the eleven (see Figure 2) with $\Delta v_{\rm IS} \geqslant 0$ are among those with spatially resolved velocity shear in the Hα emission line, meaning that the Hα spectrum exhibits a significant velocity offset as a function of spatial position; see Erb et al. (2006c) for details. Given the overall detection rate of shear in the sample of Erb et al. (2006c), we would expect to find $\sim$1 such object in a sample of 11. Furthermore, of the 14 objects with tilted Hα emission lines in the Erb et al. (2006c) sample, 8 have high-quality

absorption redshifts with $\langle \Delta v_{\rm IS} \rangle = -47 \pm 35$ km s^{-1}; 6 of 8 have $\Delta v_{\rm IS} > -60$ km s^{-1}.

The apparent connection between decreased $|\Delta v_{\rm IS}|$ and observation of measurable velocity shear in Hα can be interpreted in at least two ways. If the velocity shear indicates an unresolved merger, infalling gas (or an unusual amount of gas near zero velocity) could significantly reduce the average blueshift of the IS lines. The IS and nebular redshifts could also arise from different pieces of a merger, or even from different galaxies altogether (see Quider et al. 2010 for a possible example). Alternatively, if the tilted emission lines are caused by rotation that is most easily detected in nearly edge-on configurations, the outflows in these objects may be loosely collimated perpendicular to the disk as for many local starburst galaxies. If this were the case, one might expect to observe lower outflow velocities and perhaps stronger IS absorption near the galaxy systemic redshift for objects with smaller inclination angles to the line of sight. Both of these effects appear to play a role in the Na D IS line kinematics observed in a large sample of nearby star-forming galaxies (Chen et al. 2010). While possible inclination effects would not naturally account for highly redshifted Lyα emission, none of the objects with velocity shear identified from their Hα spectra happen to have Lyα in emission. Inclination effects could be present in our sample, although the significant bulk outflows observed in the vast majority of the sample argue against collimation and projection effects being a major factor in most cases.

As we will show in Section 4 below, we favor an explanation for many of the observed trends discussed in this section that hinges on the quantity of gas at or near zero velocity (and not on the overall outflow speed).

3. THE RELATION BETWEEN BULK OUTFLOWS AND OTHER GALAXY PROPERTIES

One of the advantages of the sample of $z \sim 2$ galaxies discussed in this paper is that a large number of other galaxy properties are available to look for trends with respect to the bulk outflow properties. Most of the measurements and inferred quantities used here are tabulated in Erb et al. (2006b, 2006c). Among the parameters available are the Hα line widths σ_v, the SFRs inferred from the Hα line fluxes (corrected for extinction according to the method outlined in Erb et al. 2006b), the surface density of star formation $\Sigma_{\rm SFR}$, the dynamical mass $M_{\rm dyn}$ measured from a combination of σ_v and the observed physical size of the Hα emitting region, and the stellar mass M_* inferred from spectral energy distribution (SED) fitting from the rest-UV to the rest optical/IR. The cold gas mass $M_{\rm gas}$ is estimated by using the measured Hα surface brightness and galaxy size and assuming that the local Schmidt–Kennicutt (Kennicutt 1998) relation between gas surface density and SFR applies. Finally, the total baryonic mass $M_{\rm bar} = M_* + M_{\rm gas}$ and the fraction of the inferred baryonic mass in the form of cold gas, $\mu = M_{\rm gas}/M_{\rm bar}$, have been utilized.

Table 1 summarizes the results of Spearman correlation tests between $\Delta v_{\rm IS}$, $\Delta v_{{\rm Ly}\alpha}$, $\Delta v_{{\rm Ly}\alpha} - \Delta v_{\rm IS}$, and these other physical quantities. The number of galaxies available in the sample for each test, which is also given in Table 1, varies depending on the quantity being evaluated. The tests have been conducted against the absolute value of the quantities $\Delta v_{\rm IS}$ and $\Delta v_{{\rm Ly}\alpha}$ so that the sense of any correlations is positive when the bulk velocity differences increase with the other physical characteristic. None of the quantities considered is significantly correlated with $\Delta v_{{\rm Ly}\alpha}$ or $\Delta v_{{\rm Ly}\alpha} - \Delta v_{\rm IS}$ at more than the 95% (2σ) confidence level, although the measured Hα velocity dispersion σ_v may be marginally correlated, in the sense that $\Delta v_{{\rm Ly}\alpha}$ is larger for objects with larger σ_v.

Table 1
Correlations of Bulk Outflow Velocity and Galaxy Properties[a]

Quantity	$-\Delta v_{\rm IS}$	$\Delta v_{{\rm Ly}\alpha}$	$\Delta v_{{\rm Ly}\alpha} - \Delta v_{\rm IS}$
σ_v[b]	−2.08 (65)	+1.81 (29)	+0.74 (29)
SFR[c]	−1.52 (87)	−0.04 (42)	−0.08 (39)
$\Sigma_{\rm SFR}$[d]	+0.95 (81)	+0.82 (37)	+0.49 (35)
$M_{\rm dyn}$[e]	−2.24 (57)	+1.02 (24)	+0.14 (24)
$M_{\rm gas}$[f]	−1.68 (73)	+0.71 (36)	+0.85 (34)
M_*[g]	−1.93 (73)	−0.37 (36)	−0.48 (34)
$M_{\rm bar}$[h]	−2.66 (73)	−0.10 (36)	−0.10 (34)
μ[i]	+1.72 (73)	+0.64 (36)	+0.93 (34)

Notes.
[a] All values are the number of standard deviations from the null hypothesis that the quantities are uncorrelated, based on a Spearman rank correlation test. Negative values indicate anti-correlations between the quantities. The number in parentheses following each value is the number of galaxies in the sample used to evaluate the correlation.
[b] Velocity dispersion measured from the Hα emission line.
[c] Star formation rate, in $M_\odot$ yr^{-1}, measured from the intensity of the Hα emission line, and corrected for extinction as in Erb et al. (2006b).
[d] Average star formation surface density, as in Erb et al. (2006b).
[e] Dynamical mass, as tabulated in Erb et al. (2006a).
[f] Cold gas mass, estimated from the star formation surface density and the observed Hα size, as in Erb et al. (2006a, 2006b).
[g] Stellar mass, estimated from SED fitting, from Erb et al. (2006c).
[h] Total baryonic mass, $M_* + M_{\rm gas}$.
[i] Gas fraction, $M_{\rm gas}/M_{\rm bar}$, as in Erb et al. (2006a, 2006c).

The measured values of $\Delta v_{\rm IS}$, on the other hand, show greater than 2σ deviations from the null hypothesis (no correlation) for the quantities σ_v, $M_{\rm dyn}$, and $M_{\rm bar}$. While σ_v and $M_{\rm dyn}$ are correlated with one another by virtue of the fact that the former is used to calculate the latter (see Erb et al. 2006c), the two mass estimates $M_{\rm dyn}$ and $M_{\rm bar}$ are measured using completely independent methods. Erb et al. (2006c) show that these mass estimates track each other very well, inspiring some confidence that both are providing reasonable estimates of the true masses within the Hα emitting regions of the galaxies. Within the Hα sample considered here, the inferred value of $M_{\rm bar}$ ranges from $\simeq 1 \times 10^{10}$ to $\simeq 3 \times 10^{11}$ $M_\odot$, and was shown to track $M_{\rm dyn}$ much more tightly than M_*, the stellar mass. Figure 3 shows plots of $M_{\rm dyn}$ and $M_{\rm bar}$ versus $\Delta v_{{\rm Ly}\alpha}$ and $\Delta v_{\rm IS}$. The sense of the possible correlations of $\Delta v_{\rm IS}$ with galaxy mass is that $\Delta v_{\rm IS}$ (the centroid velocity of the IS absorption lines) tends to be closer to $v = 0$ for objects with higher mass. The more significant of the mass correlations, with $M_{\rm bar}$ (significant at the 99% confidence level), appears to arise because none of the galaxies with baryonic masses smaller than $\simeq 3 \times 10^{10}$ $M_\odot$ have measures of $\Delta v_{\rm IS}$ near zero, while at masses $M_{\rm bar} > 3 \times 10^{10}$ $M_\odot$, a significant fraction do.

There are no significant correlations between $|\Delta v_{\rm IS}|$ and parameters related to star formation. The lack of correlation is interesting in light of recent studies relating outflow velocity to galaxy properties in local starbursts; for example, both Martin (2005) and Rupke et al. (2005) find evidence for correlations of outflow speed with SFR and dynamical mass (represented by the circular velocity), in the sense that the outflow velocities increase with both quantities (i.e., apparently the opposite to what is observed in the $z \simeq 2$ sample). These relatively local galaxy samples have a dynamic range spanning

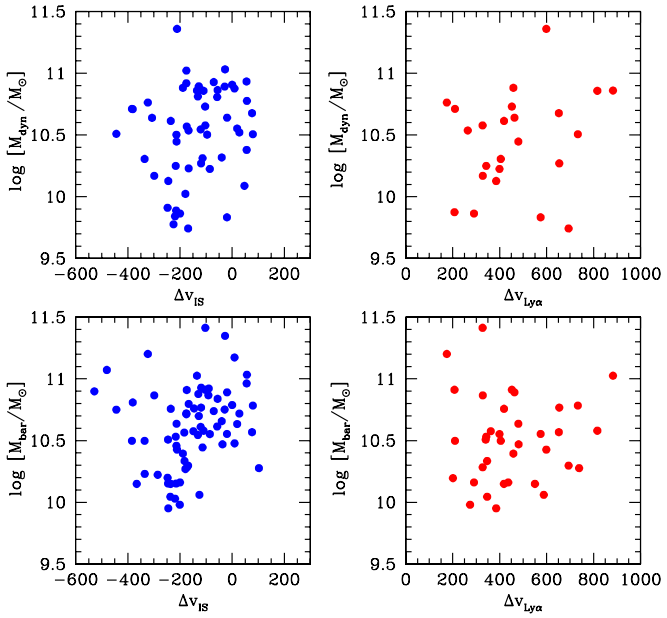

Figure 3. Plots showing the dependence of bulk outflow velocities on dynamical mass estimated from Hα line widths and observed sizes (top panels) and total baryonic mass (i.e., the sum of inferred stellar and cold gas masses; bottom panels).

(A color version of this figure is available in the online journal.)

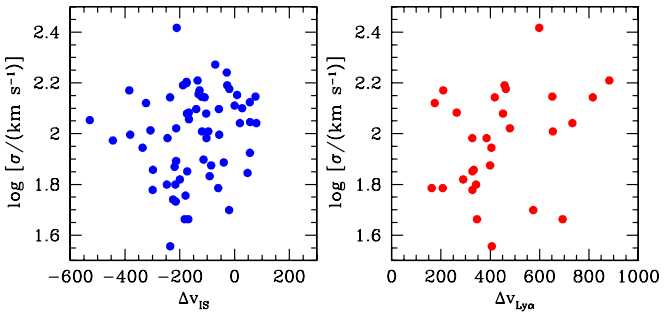

Figure 4. Dependence of the Hα velocity dispersion σ_v on centroid velocities $\Delta v_{\rm Ly\alpha}$ and $\Delta v_{\rm IS}$ measured from the far-UV spectra.

(A color version of this figure is available in the online journal.)

~4 orders of magnitude in SFR, and include dwarf starbursts with $v_c \sim 30$ km s^{-1} and SFR $< 1\,M_\odot$ yr^{-1}, i.e., a much larger range than present in our $z \sim 2.3$ sample. The observed correlations in the local sample flatten for galaxies with SFR $\gtrsim$ 10–100 $M_\odot$ yr^{-1} (Rupke et al. 2005), the approximate range of SFRs in our current sample. In other words, no trends are present in the low-redshift samples when only galaxies with parameters characteristic of our $z \sim 2$ galaxies are considered. Also, as we discuss below, other effects on the kinematics measured from centroid velocities would likely mask the presence of a weak correlation if it were present.

At higher redshift, Weiner et al. (2009) also found that the inferred outflow velocity in composite spectra of $z \simeq 1.4$ star-forming galaxies is a slowly increasing function of SFR, $v_{\rm out} \propto {\rm SFR}^{0.3}$. However, because their composite spectra are of relatively high spectral resolution, Weiner et al. (2009) measure $\Delta v_{\rm IS}$ as the velocity at which the IS absorption reaches 90% of the continuum value, i.e., close to the *maximum* blueshifted velocity rather than the centroid. They decompose the Mg II IS line into a "symmetric" and "outflowing" component, and find that the strength of the symmetric component is very steeply dependent on stellar mass—in fact, it is much *steeper* than the variation of the outflowing component. As in our sample, the lowest-mass galaxies are consistent with having *zero* symmetric component (see their Figure 13 and Table 1).

Clearly, the centroid velocity of strongly saturated IS absorption lines is in many ways a blunt tool for characterizing the velocity of outflowing gas. First, the lines may include a significant amount of IS gas at or near zero velocity with respect to the galaxy systemic redshift, which would have the effect of decreasing the measured value of $|\Delta v_{\rm IS}|$ even if outflow velocities were substantial. While Martin (2005), Rupke et al. (2005), and Weiner et al. (2009) removed a component of IS absorption centered at zero velocity before evaluating the velocity of outflowing material, it is generally not possible to do this for individual spectra in our $z \simeq 2$ sample because of more limited spectral resolution. It is also not clear that subtracting a symmetric $v = 0$ component of IS absorption is the best approach for evaluating the kinematics of circumgalactic gas. It is possible, or perhaps even likely, that the IS line profiles would be sensitive to infalling material, which when seen in absorption against the galaxy's UV continuum would tend to be redshifted by up to a few hundred km s^{-1} with respect to a galaxy's systemic redshift; if so, the observed redshifted wing of IS absorption could be substantially stronger than the blueshifted portion of the $v \simeq 0$ profile. As we have mentioned (see also Section 8.4 below), gas with positive (redshifted) velocities with respect to $z_{\rm sys}$ would be expected in at least a fraction of galaxies if infalling cool gas is present with a non-negligible covering fraction.

Finally, we address whether outflows influence the Hα line widths used to calculate dynamical masses (Erb et al. 2006c). In Figure 4, we show a comparison of $\Delta v_{\rm Ly\alpha}$ and $\Delta v_{\rm IS}$ with the Hα velocity dispersion σ_v. As mentioned above, there is a marginally significant ($\simeq 2\sigma$) tendency for $|\Delta v_{\rm IS}|$ to be smaller in galaxies with larger values of σ_v. The correlation is likely to be related to the trends with galaxy mass we have already noted. If strong outflows were significantly influencing the observed Hα lines, one might expect objects with the largest $|\Delta v_{\rm IS}|$ also to have larger σ_v, a trend opposite to what is observed. As further evidence of the disassociation of the observable Hα emission and the winds, composite UV spectra (discussed in Section 4) constructed by combining individual spectra shifted to the nebular redshift show that Hα is at the same redshift as the stars. Additionally, observations of local galaxies suggest that Hα emission from outflowing material would fall far below our detection threshold; for example, Lehnert et al. (1999) studied the extended Hα emission from the superwind in the starburst galaxy M82, finding that it has a total luminosity of 2.4×10^{38} erg s^{-1} and comprises only ~0.3% of the total Hα flux. Since the typical S/N of our $z \sim 2.3$ Hα observations is $\lesssim$10, it would be extremely difficult to recognize a component of emission coming from wind material. Finally, Colina et al. (2005) have also found, through integral field spectroscopy of Hα emission in local ULIRGs, that the central velocity dispersions are unaffected by outflows.

4. INFERENCES FROM COMPOSITE FAR-UV SPECTRA

4.1. The Use of $z_{H\alpha}$ to Measure Galaxy Systemic Redshifts

The existence of a large sample of galaxies for which both rest-frame optical (Hα) and rest-frame far-UV spectra are available provides an opportunity to evaluate high S/N composite UV spectra formed from unusually precise knowledge of the systemic redshifts of the galaxies. A stacked composite UV

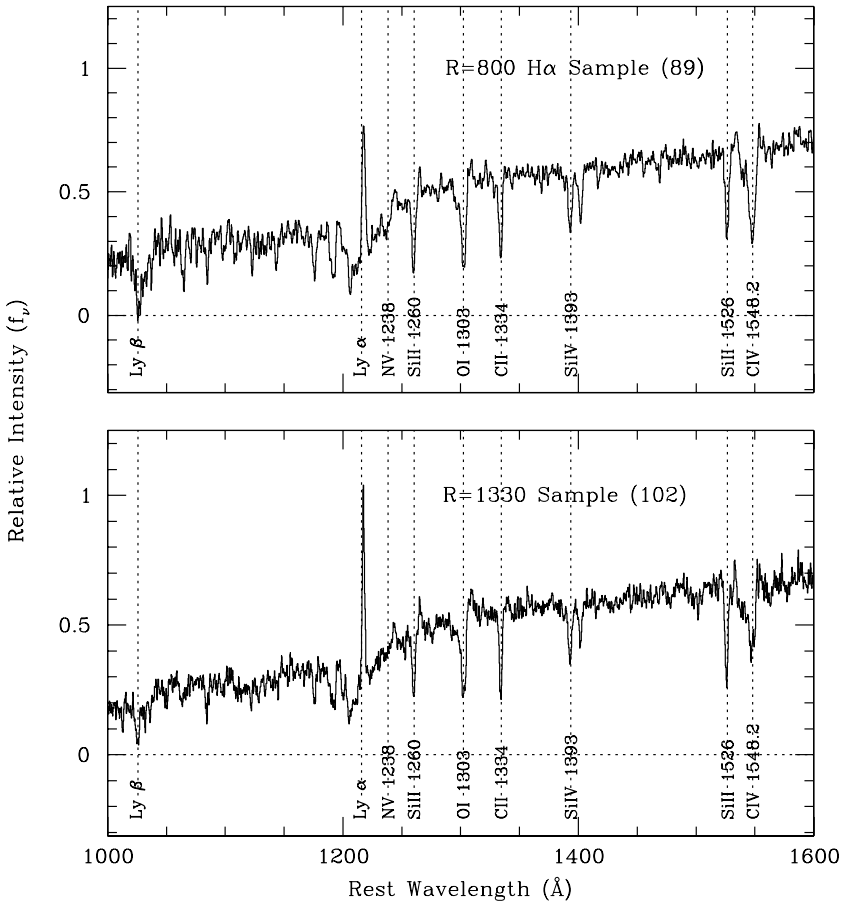

Figure 5. Composite rest-frame far-UV spectra for two independent samples of $z \sim 2.3$ galaxies. The top panel is an average of the 89 spectra in the Hα sample, with $R = 800$, after normalizing each to the same relative intensity in the range 1300–1500 Å. The bottom panel is a composite of 102 galaxy spectra obtained with higher spectral resolution ($R = 1330$), shifted into the rest frame using Equations (2) and (4), and scaled as the first sample before averaging.

spectrum was formed by shifting each spectrum into the rest frame using $z_{\rm H\alpha}$, scaling based on the flux density in the range 1300–1500 Å, re-sampling onto a common wavelength scale of 0.33 Å per pixel, and averaging at each dispersion point, with outlier rejection. Thus, the composite is an unweighted average of all 89 galaxies having both Hα spectra from NIRSPEC and high-quality UV spectra from LRIS-B; the result is shown in Figure 5. A measurement of the centroids of weak stellar photospheric absorption features (S V λ1501.76, O IV λ1343.354, and C III λ1171.76 were used for this purpose; see Shapley et al. 2003; Pettini et al. 2000) in the rest-frame composite spectrum verifies that the Hα redshifts are very close to the systemic redshifts of the stars in the galaxies, with a mean velocity of $v_* = 13 \pm 24$ km s^{-1}. Composites formed from various subsets of the data yield a similar level of agreement: for example, a composite formed from the subset of 28 galaxies with significantly deeper LRIS-B spectra (with total integration times ranging from 5 to 20 hr compared to the typical 1.5 hr) has $v_* = 2 \pm 36$ km s^{-1}.

4.2. Velocity Widths of IS Lines and the Maximum Outflow Velocity

One of the quantities that can be evaluated with increased confidence using the new sample is the velocity *extent* of the IS absorption lines and Lyα emission, in addition to the centroid velocities discussed in the previous section. Of particular interest are $\eta_{\rm IS}$, the FWHM of the IS absorption lines, and $\eta_{\rm Ly\alpha}$, the FWHM of the Lyα emission line, corrected for the instrumental resolution. Unfortunately, as discussed above, the instrumental resolution is not always known precisely because it depends on the seeing-convolved size of the galaxy compared to the 1.″2 slits used for all of the LRIS-B spectroscopy. For objects illuminating the slit uniformly, the spectral resolution is measured to be 450 km s^{-1} (FWHM) for the 400 line mm^{-1} grism used for almost all of the optical spectra of galaxies in the Hα sample; however, for typical seeing of ≃0.″6–0.″8, galaxies in our sample have FWHM ≃ 1.″0. Given this, we would expect that the actual spectral resolution is FWHM ≃ 370 km s^{-1} ($R = 800$). We have verified this for both the composite spectrum of all Hα galaxies, and for a smaller subset of galaxies with very deep spectroscopic integrations, by measuring the spatial size of each object in the slit direction. Assuming that the Hα redshift uncertainties are $\sigma_z \simeq 60$ km s^{-1} and that individual spectra have $\sigma_{\rm res} \simeq 160$ km s^{-1} (i.e., FWHM/2.355), the estimated *intrinsic* FWHM of IS absorption features and Lyα emission in the composite spectrum are $\eta_{\rm IS} \simeq 540$–570 km s^{-1} and $\eta_{\rm Ly\alpha} \simeq 620$–$650$ km s^{-1}, respectively.

We have recently obtained LRIS-B spectra of galaxies selected in the same way as the Hα sample, but observed using the 600 line mm^{-1} grism instead of the 400 line mm^{-1} grism used for the vast majority of the Hα sample. These observations provide spectral resolution 1.68 times higher for the same slit width and object size. As a test of our ability to measure line profiles with marginally resolved data, we assembled a sample of 102 spectra all obtained on the same observing run and with consistent observing conditions (seeing of ≃0.″6–0.″7 FWHM

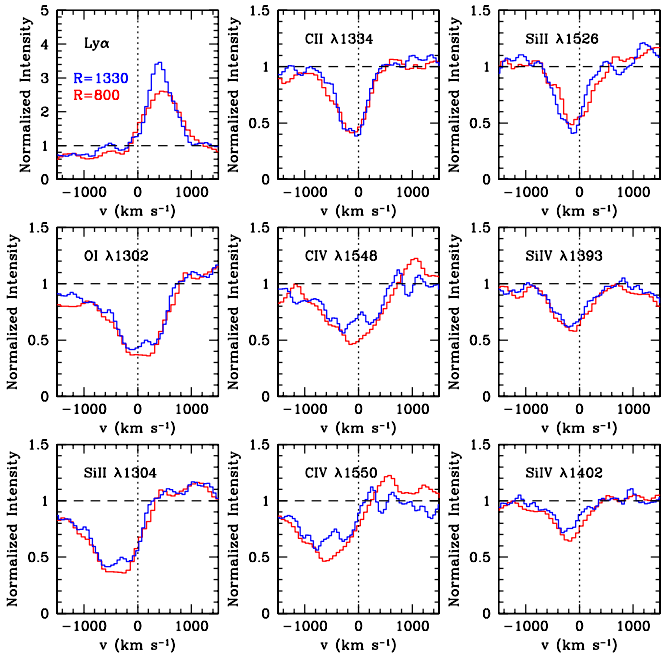

Figure 6. Comparison of the Lyα and IS line profiles for the full Hα sample (red) and the composite of 102 identically selected objects observed with higher spectral resolution (blue), where the latter have been shifted into the rest frame using the rules defined in Section 2. For blended features such as O I λ1302/Si II λ1304 and C IV $\lambda\lambda$1548, 1550, a separate panel is given for each; in both cases, one should look at the longer of the two components for the profile near $v \sim 0$ and the shorter one to gauge the extent of the most blueshifted velocities, due to the line blending. Note the very similar velocity profiles for the two independent samples, for both the minimum and maximum velocities.

(A color version of this figure is available in the online journal.)

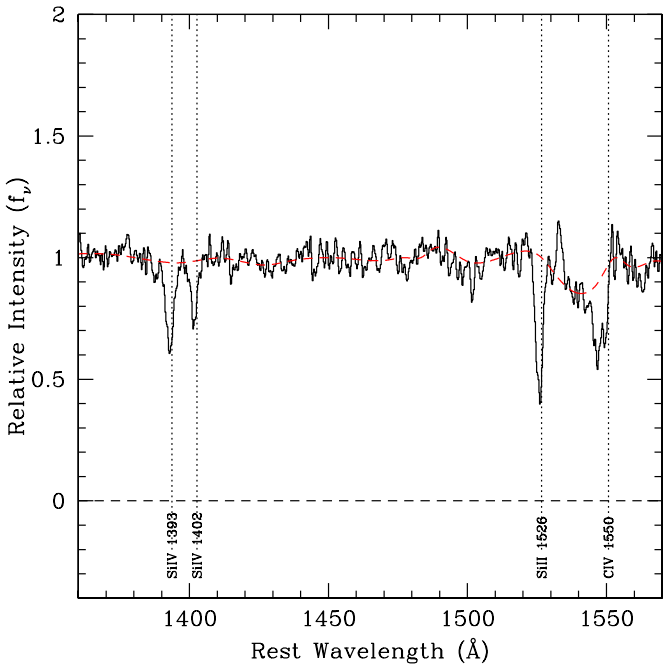

Figure 7. Portion of the composite spectrum shown in the lower panel of Figure 5 in the vicinity of the Si IV and C IV doublets. The dashed red curve is an example continuum fit used to normalize the spectrum for measuring the strength of the IS component of these lines. Note that the continuum has been adjusted to remove the broad absorption due to the stellar wind component of C IV; a similar adjustment was made to remove the stellar component of Si IV, though it is much weaker than the C IV feature. The weak emission line within the broad C IV wind absorption feature is nebular Si II* λ1533, one of several weak excited fine-structure emission lines observed in the spectra of $z \simeq 2$–3 galaxies (Shapley et al. 2003). The weak absorption line near 1501 Å is photospheric S V.

(A color version of this figure is available in the online journal.)

evaluated at 4800 Å) in a field which remained very close to the zenith at the Keck Observatory, thus minimizing issues of differential atmospheric refraction. We applied the rules given in Equation (4) above to shift the spectra into the rest frame, and produced a composite spectrum, shown in the bottom panel of Figure 5, with an effective spectral resolution of FWHM $\simeq$ 225 km s^{-1} ($R \simeq 1330$). The stellar photospheric absorption features in the stacked spectrum have $v_* = -2 \pm 10$ km s^{-1}, illustrating that the rules for estimating the systemic velocity from the UV spectra work very well on average, and that the higher resolution spectra are advantageous for producing more accurate wavelengths for weak (stellar and IS) features.

The line profiles of the $R = 800$ and $R = 1330$ composite spectra are remarkably similar for both Lyα emission and the strong IS absorption features, as shown in Figure 6. The spectra yield the same value of $\eta_{\mathrm{Ly}\alpha}$ and η_{IS} after accounting for the difference in spectral resolution. We are particularly interested in the asymmetry of the line profiles and the value of the maximum blueshifted velocity v_{max}, which we define as the velocity at which the blue wing of the IS absorption lines meets the continuum. We find that v_{max}, although difficult to measure for typical spectra of individual galaxies due to limited S/N, is not strongly dependent on spectral resolution; Figure 6 shows that $|v_{\mathrm{max}}| \simeq 700$–800 km s^{-1} for both composite spectra. As discussed above, the C IV and (to a lesser extent) Si IV doublets in galaxy spectra have contributions from both the IS lines and from the P-Cygni stellar wind lines from massive stars, and thus the IS component must be separated from the stellar feature in the process of fitting the local continuum. An example of a continuum fit near the Si IV and C IV features is shown in Figure 7. Fortunately, the P Cygni feature is generally both broader and shallower than the IS components of these lines, so that while the continuum uncertainties are larger than for unblended features, they do not prevent an accurate measurement in relatively high S/N composite spectra.

The velocity profiles of some of the strongest spectral features in the stacked spectrum of the galaxies observed with $R = 1330$ are overplotted in Figure 8. Evidently, $|v_{\mathrm{max}}| \simeq 700$–800 km s^{-1} is a generic feature of the spectra of these rapidly star-forming galaxies, in spite of the fact that the average centroid of the IS line profiles is more modest, with $\Delta v_{\mathrm{IS}} \sim -165$ km s^{-1} from the previous section. The apparent values of $|v_{\mathrm{max}}|$ are relatively insensitive to spectral resolution.

The line profiles in the spectra of individual galaxies can, of course, vary considerably. Figure 9 shows the spectra of two individual galaxies to illustrate the point: one is MS1512-cB58, the $z = 2.729$ lensed Lyman break galaxy (LBG) whose spectrum has been analyzed in detail by Pettini et al. (2000, 2002); the other is Q0000-D6 (Shapley et al. 2003), a bright LBG at $z = 2.966$ observed at a comparable spectral resolution of $\simeq$1500. These spectra show clear differences in the details of the profiles and with the apparent covering fraction of the continuum, particularly for the low-ionization species which differ in apparent optical depth by a factor of $\simeq$2. Clearly, Lyα emission is prominent in D6, but very weak in the spectrum of cB58 (see also Quider et al. 2009). The spectrum of Q0000-D6 also has an unusual high-ionization component that produces clear Lyα absorption in the apparent blue wing of the Lyα emission line, as well as in the high ions (but is less prominent

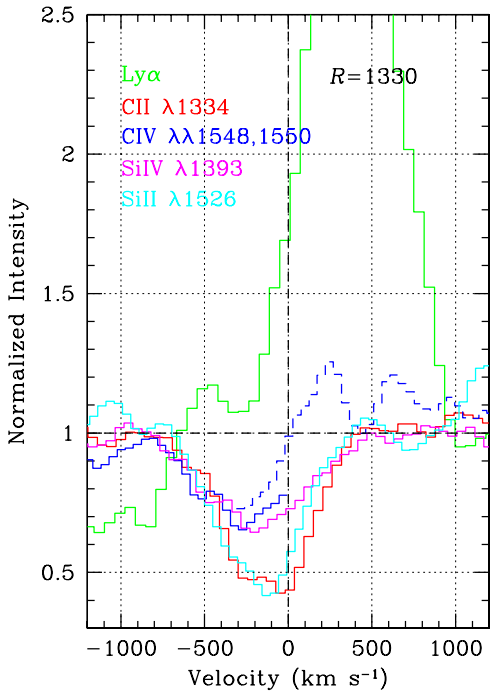

Figure 8. Velocity profiles of strong IS lines and Lyα emission features relative to systemic for the composite UV spectrum of the $R = 1330$ sample. The C IV profile is a solid blue histogram for the λ1548 component and dashed for λ1550.

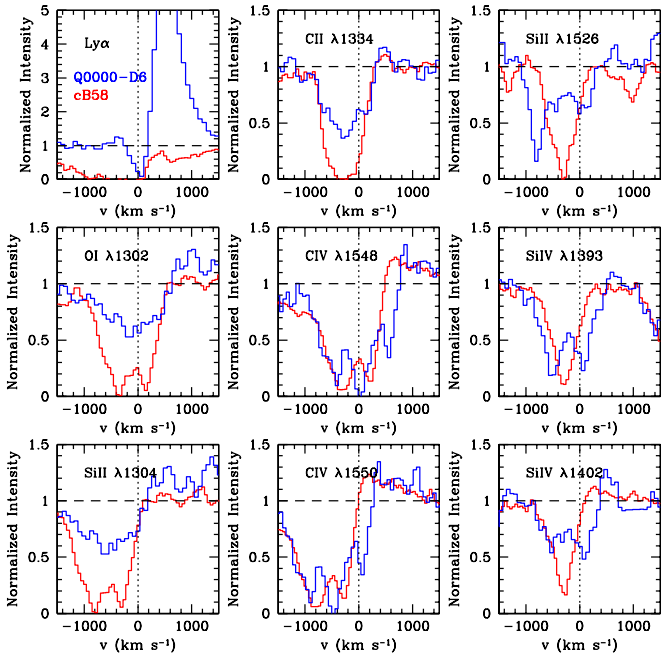

Figure 9. As for Figure 6, comparing the spectra of two individual objects having particularly high-quality UV spectra as well as accurate systemic redshifts from stellar absorption features. The spectrum of MS1512-cB58 (the $R \simeq 1600$ spectrum from Pettini et al. 2000) is in red, while the spectrum of Q0000-D6, obtained with $R \simeq 1300$, is in blue. Despite significant differences in spectral "morphology" (e.g., D6 has strong Lyα line emission, while cB58 has strong absorption, and the ratio of the strengths of high-ionization lines to low-ionization lines is quite different), the *range* of velocities spanned by the outflows is quite similar in both cases, with the maximum velocities of $v \simeq 800$ km s^{-1}. Note that the Si II λ1526 line of D6 is affected by absorption from another system in the blue wing of the profile. Both of these galaxies would be in the $M_{\rm bar} < 3.7 \times 10^{10}\,M_\odot$ (i.e., lower baryonic mass) subsample.

in the lower ions) near $v = 0$. Still, the velocity envelope for the blueshifted material is remarkably consistent with that seen in the composites presented above: maximum blueshifted velocities of $|v_{\rm max}| \simeq 800$ km s^{-1}, roughly independent of ionization level.

4.3. Trends with Baryonic Mass

Returning to the trends in the centroid velocities of the IS lines noted in the previous section, it is instructive to examine the mean line profiles of composite spectra selected by implied baryonic mass $M_{\rm bar}$, the parameter most significantly linked to the observed kinematics of the IS absorption features. Figure 10 shows the comparison between the halves of the Hα sample that are above and below an inferred $M_{\rm bar} = 3.7 \times 10^{10}\,M_\odot$, the sample median. There are clear differences in the Lyα emission line strength, which is similar to that seen for subsamples of different metallicity as in Erb et al. (2006a). The peak of the Lyα emission line profile is shifted by $\simeq +200$ km s^{-1} (from $\simeq +400$ to $\simeq +600$ km s^{-1}) for the higher-mass subsample relative to that of the lower-mass subsample.[13] The profiles of the low-ionization IS lines (C II λ1334 is in the cleanest spectral region and illustrates it best) may be indicating the root cause of the kinematic trends discussed in Section 3: the higher-mass sample exhibits stronger IS absorption at or near $v \sim 0$, while the profiles are nearly identical in their behavior near $v = -|v_{\rm max}|$. This "excess" low-velocity material in the higher-mass subsample—a shift of $\simeq$200 km s^{-1} in the red wing of the IS line profiles—systematically shifts the centroid of the IS velocity distribution by $\simeq +100$ km s^{-1} relative to the lower-mass subsample, while the blue wing of the profile exhibits no clear trend with $M_{\rm bar}$. The excess low-velocity material in the higher-mass subsample is not obvious in the C IV absorption profile, for which the two profiles appear to be nearly identical for $v \gtrsim 0$ (note that C IV was not used to measure $\Delta v_{\rm IS}$ for any of the galaxies in the sample because of the dependence of the rest wavelength for the blend on the relative strength of the lines of the doublet).

Figure 11 shows the residual apparent optical depth $\Delta\tau(v)$ for three relatively isolated low-ionization transitions for the high- and low-$M_{\rm bar}$ subsamples. By this we mean the additional optical depth as a function of velocity that when added to the line profiles of the low-$M_{\rm bar}$ subsample would produce line profiles identical to those of the high-$M_{\rm bar}$ subsample, i.e.,

$$I_{\rm hm}(v) = I_{\rm lm}(v)e^{-\Delta\tau(v)}, \quad (5)$$

where $I_{\rm hm}$ and $I_{\rm lm}$ are the spectral intensity of the high-$M_{\rm bar}$ and low-$M_{\rm bar}$ subsamples, respectively. The spectrum $\Delta\tau(v)$ has a peak at $v \simeq 0$, a centroid at $v = +154$ km s^{-1}, and a velocity width of $\sigma_v \simeq 120$ km s^{-1} after correcting for the effective instrumental resolution. The excess apparent optical depth $\Delta\tau$ in these transitions accounts for $\simeq$25% of the equivalent width of the full low-ion profiles of the high-$M_{\rm bar}$ subsample. The additional component of absorption in the high-$M_{\rm bar}$ subsample also changes the average IS line width from $\eta_{\rm IS} = 540$ km s^{-1} for the lower-mass subsample to $\eta_{\rm IS} = 660$ km s^{-1} for the higher-mass subsample.

We will return to a discussion of the possible implications of the baryonic mass dependence of the IS line kinematics in Section 8.

[13] No significant correlation was found between $M_{\rm bar}$ and $\Delta v_{{\rm Ly}\alpha}$ in Section 3, but many of the galaxies in the higher-mass subsample had Lyα emission that was too weak to measure, resulting in a very small sample.

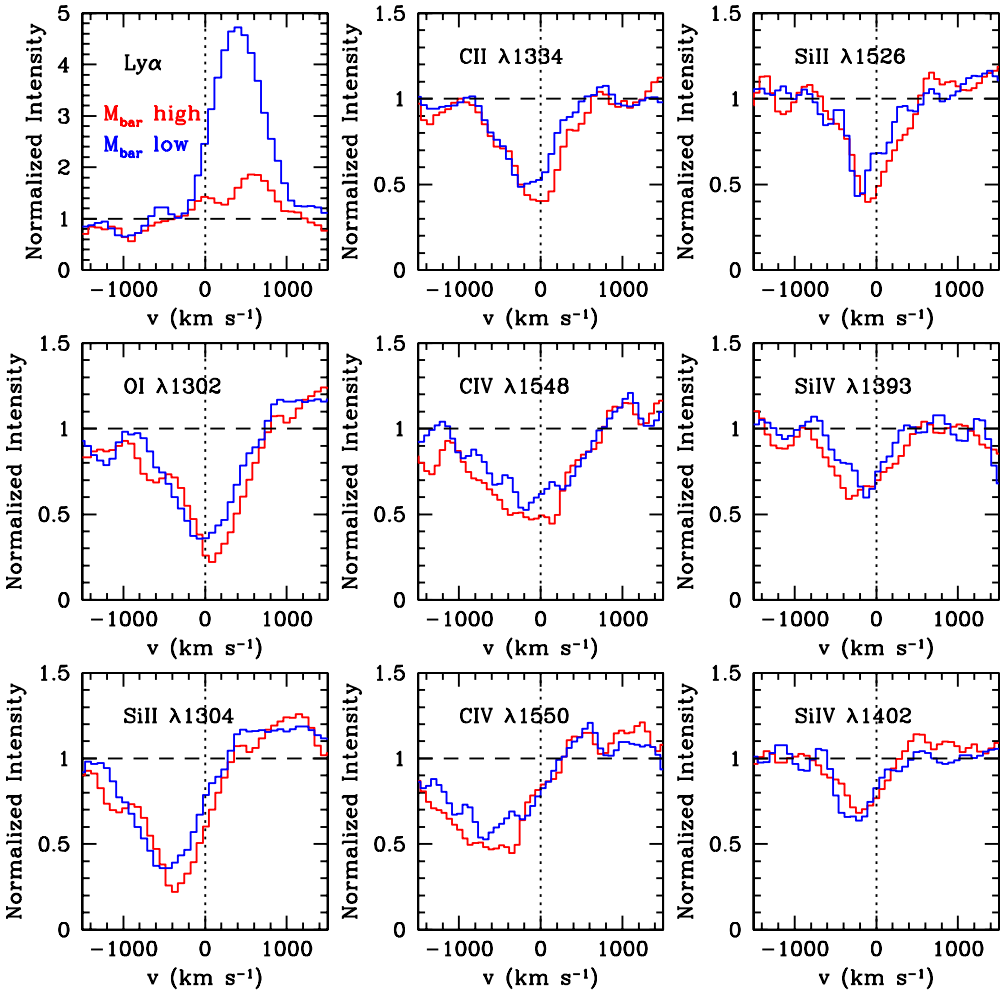

Figure 10. As for Figure 6, comparing the composites of subsets of the Hα sample depending on their inferred baryonic mass $M_{\rm bar}$. The composite from objects with $M_{\rm bar} > 3.7 \times 10^{10}\,M_{\odot}$ is plotted in red, and that from objects with $M_{\rm bar} < 3.7 \times 10^{10}\,M_{\odot}$ in blue. Note the differences in the profiles of the low ions (e.g., Si II, O I, C II) for $v \lesssim 0$, where the high baryonic mass objects appear to have stronger low-ion absorption at velocities closer to systemic. These differences do not seem to be present for the higher-ionization lines (e.g., see the C IV λ1550 panel), nor are there differences in the maximum blueshifted velocities.

(A color version of this figure is available in the online journal.)

5. LYα EMISSION

5.1. Observed Trends

We have shown in Section 2 that the centroid velocity of Lyα emission $\Delta v_{\rm Ly\alpha}$ exhibits larger scatter than $\Delta v_{\rm IS}$ relative to the systemic redshift defined by Hα emission, but that the relative consistency of $\Delta v_{\rm Ly\alpha} - \Delta v_{\rm IS}$ suggests a causal link between the two kinematic measures. In this section, we attempt to understand the nature of this relationship in greater detail.

In Section 4, we presented evidence that the kinematic profiles of strong IS lines in the spectra of rapidly star-forming galaxies exhibit greater variation near $v = 0$ than at large blueshifted velocities. Moreover, the presence of significant low-ion absorption at $v \gtrsim 0$ strongly affects both the apparent velocity of Lyα emission and the centroid velocity $\Delta v_{\rm IS}$ of the IS lines, though $v_{\rm max}$, the maximum blueshift, remains essentially unchanged.

A commonly adopted "toy model" (see, e.g., Pettini et al. 2002; Adelberger et al. 2003) used to interpret the kinematics of Lyα emission and IS absorption lines in starburst galaxy spectra involves a roughly spherically symmetric outflow resulting in generally blueshifted absorption as seen from Earth. Because Lyα photons resonantly scatter, they escape from the nebula only when they acquire a velocity such that the optical depth to scattering in the material which lies (physically) between the observer and the emitted Lyα photon becomes small. Perhaps the easiest way for an Lyα photon to reach Earth is to acquire the velocity of an outflowing material on the far side of the galaxy, but to be emitted in the observer's direction, so that the photon has been redshifted by several hundred km s^{-1} relative to the bulk of the material through which it must pass to reach us. This picture would explain qualitatively why the dominant component of Lyα emission *always* appears redshifted relative to the galaxy systemic velocity. Neglecting radiative transfer effects for the moment, if the range of velocities of outflowing gas is similar on the "far" side of the galaxy to what we observe (through the IS absorption lines) on the "near" side, then one would expect the maximum blueshifted velocity $|v_{\rm max}|$ to be comparable to the maximum velocity observed in the red wing of the Lyα emission line. One could then explain different spectral morphology near the Lyα line by altering the *distribution* of Lyα optical depth as a function of velocity for the material between the observer and the far side of the outflow.

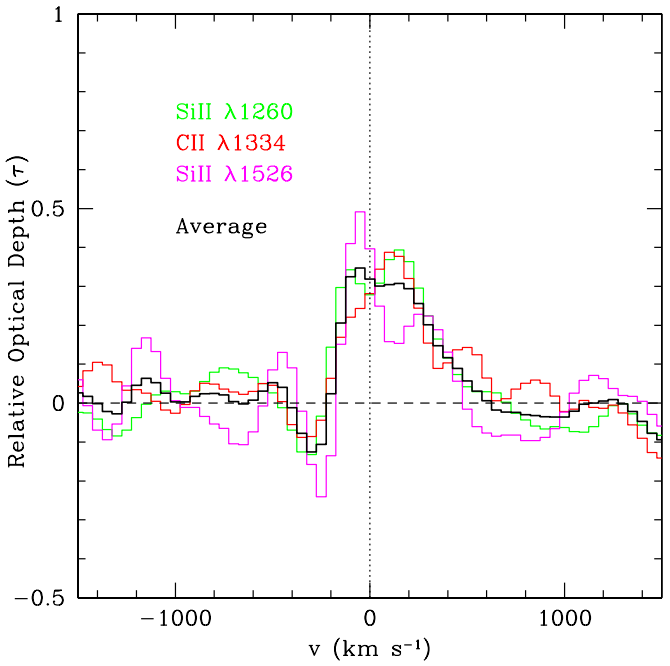

Figure 11. Relative optical depth $\tau_{\rm high}-\tau_{\rm low}$ for selected low-ionization absorption lines, vs. velocity relative to systemic, where these quantities refer to the composite spectra of the high-$M_{\rm bar}$ and low-$M_{\rm bar}$ subsamples. The histograms are for Si II λ1260 (green), C II λ1334 (red), and Si II λ1526 (magenta) IS line profiles, where the heavy black curve is the average residual optical depth for the three transitions. Note the absence of significant residuals at blueshifted velocities (with the possible exception of local "peak" near $v = -300$, which represents slightly deeper absorption in the spectrum of the low-$M_{\rm bar}$ subsample). The excess absorption in the $M_{\rm bar}$-high subsample has its centroid at $v = +154$ km s^{-1} and its peak near $v \simeq 0$.

(A color version of this figure is available in the online journal.)

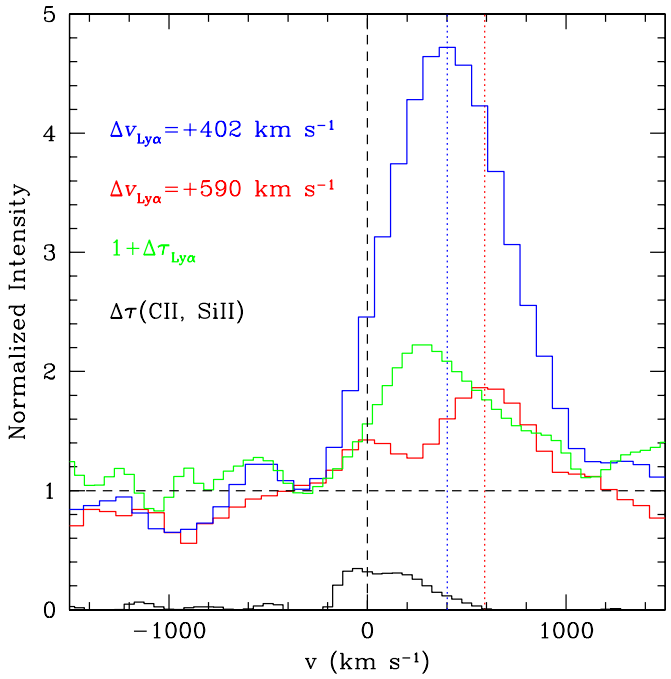

Figure 12. Comparison of the composite Lyα emission profiles of the same samples as in Figure 10. Also shown (green histogram) is the inferred function $1 + \Delta\tau_{\rm Ly\alpha}(v)$, where $\Delta\tau_{\rm Ly\alpha}(v)$ is the excess apparent optical depth in Lyα (as a function of velocity) required to produce the weaker of the two Lyα profiles from the stronger. The black histogram reproduces the low-ion residuals from Figure 11.

(A color version of this figure is available in the online journal.)

For example, in the simplest possible scenario, one could imagine that the difference in the Lyα line profiles shown in Figure 12 (or any other set of Lyα profiles) could be explained by altering the distribution of $\tau_{\rm Ly\alpha}(v)$ such that only the most-redshifted photons have an appreciable chance of making it through the intervening H I. It is then easy to see that increasing $\tau_{\rm Ly\alpha}(v)$ near $v = 0$ will shift the apparent peak and centroid of Lyα emission toward the red, since Lyα photons emitted from material with line-of-sight velocities near $v = 0$ will have no chance to reach the observer—only those with the most extreme redshifted velocities will find $\tau_{\rm Ly\alpha}$ low enough to make it through in our direction. Figure 12 shows the Lyα profiles for the two samples split by $M_{\rm bar}$ as in the previous section—the green histogram shows $1 + \Delta\tau_{\rm Ly\alpha}(v)$ with $\Delta\tau_{\rm Ly\alpha}$ defined so as to produce the red profile (high $M_{\rm bar}$) from the blue one (low $M_{\rm bar}$), i.e.,

$$I_{\rm hm}(v) = I_{\rm lm}(v)e^{-\Delta\tau_{\rm Ly\alpha}(v)}. \quad (6)$$

Here, $\Delta\tau_{\rm Ly\alpha}$ is the *excess* optical depth, over and above that already present for the low-$M_{\rm bar}$ subsample; the effective optical depth, including both scattering and dust opacity, must be very significant even for the latter, since the equivalent width of the observed Lyα emission line is ∼20–40 times smaller than that expected for Case-B recombination and a normal population of high-mass stars (e.g., Charlot & Fall 1991).

Figure 12 also reproduces the excess optical depth $\Delta\tau$(C II, Si II) in the low-ionization metallic species from Figure 11 for comparison to $\Delta\tau$(Lyα). While both have centroids with $v > 0$, $\Delta\tau$(Lyα) peaks at $v \sim +270$ km s^{-1}, close to the velocity at which $\Delta\tau$(C II, Si II) begins to decrease going toward higher positive velocity. The differences are probably due to a combination of generally much higher optical depths in the Lyα transition than for the low-ion metals (Lyα photons can only escape from regions having the lowest τ(Lyα)), as well as geometric effects relating to the possible location of gas seen in absorption (which must lie in front of the continuum source) versus emission (which may lie either in front of or behind the continuum source).

5.2. *Understanding Lyα Emission Line Kinematics*

The real situation is undoubtedly far more complicated. There have been several recent theoretical treatments of Lyα radiative transfer in the context of galactic outflows (Verhamme et al. 2006, 2008; Schaerer & Verhamme 2008; Hansen & Oh 2006; Dijkstra et al. 2006a, 2006b; Zheng & Miralda-Escudé 2002), and even in the highly idealized geometric configurations considered in these papers, a given line profile does not uniquely specify the combination of velocity field, H I column density, covering fraction, and dust opacity that applies to a given observation. For example, both bulk velocity fields and photon diffusion are capable of accounting for Lyα photons that acquire large redshifts before escaping from a model galaxy. The profiles of IS absorption lines, particularly in the highest-quality spectra of individual objects, indicate that material with velocities ranging from ∼+200 to ∼−800 km s^{-1} exists in most observed ions for most galaxies (as discussed above). Essentially all of the ions observed in spectra of the quality presented here are strongly saturated, so that line profiles are best thought of as maps of covering fraction (hereinafter f_c) versus velocity. The simultaneous presence of neutral and singly ionized species along with higher-ionization species like C IV, with similar overall velocity envelopes, reinforces the idea that

the interstellar medium (ISM) is a complex multiphase medium. To make matters worse, we do not know where, in physical space, IS absorption at a given observed velocity actually arises. Since Lyα photons must traverse this medium, experiencing typically thousands of scattering events, it is therefore extremely difficult to predict in detail what the emergent Lyα profile will look like.

Verhamme et al. (2006, 2008) consider a wide range of parameters, examining the effect on emergent Lyα line profiles, for models of central (monochromatic) point sources surrounded by an expanding shell of gas with varying H I column density and Doppler parameter (b). A generic prediction, as discussed above, is that Lyα emission (when present) will be very asymmetric, with the details of the line shape depending on the assumed shell velocity, Doppler parameter, and H I column density in the shell. For the expanding shell models, these authors predict that the peak of the Lyα emission line should appear near velocity $v \simeq -2 \times V_{\rm exp}$, where $v_{\rm exp}$ is the shell velocity, due to the combined effects of radiative transfer and the bulk velocity of the scattering medium. The red wings of the Lyα line are expected to be produced by photons scattering multiple times from the receding side of the expanding shell (as seen by an observer on Earth); most of the migration of Lyα photons toward large redshifted velocities arises from absorption in the Lorentzian wings associated with high values of N(H I). Larger values of $v_{\rm exp}$ and higher assumed values of N(H I) also accentuate the red wing of the Lyα line and suppress regions close to the systemic redshift, moving both the peak and the centroid of Lyα emission to higher velocities. A further prediction of the shell models is the presence of additional Lyα peaks that correspond to photons escaping in either the blue or the red wing of Lyα associated with the approaching side of the shell; photons emitted from the red wing of the Lyα line in the approaching side would then lie close to $v = 0$, while the blue wing would tend to form a peak with $v \lesssim -V_{\rm exp}$.

In a less-idealized situation, where the bulk velocity of the outflowing gas is not single-valued, but spans a more-or-less continuous velocity range of at least 800 km s^{-1}, the dominant mechanism for the migration of Lyα photons in both frequency space and real space becomes simpler, in some respects.[14] In a scenario with more gradual velocity gradients and a clumpy medium spread over a large range in galactocentric distance r (rather than a "shell") associated with an outflow, photons can achieve velocities off-resonance by scattering their way through gas with a range of v; when they escape the nebula and are observed as redshifted Lyα photons by the observer, they would generally exhibit Doppler shifts that directly reflect the velocity with respect to the systemic velocity of the gas from which they were last scattered. Since the medium is clumpy, the column density N(H I) for individual "clumps" becomes less relevant than their velocity distribution and covering fraction, since most Lyα photons will scatter off the "surfaces" of clumps, rarely encountering regions where absorption or emission in the broad wings of a line is important (see Neufeld 1991 for a discussion of this type of situation). Note that the clumpy geometry is qualitatively different from, e.g., the "Hubble expansion" model considered by Verhamme et al. (2006), which has v increasing smoothly with r. In this case, the radiative transfer is still important because the scattering medium is continuous and has associated with it a particular N(H I) through which all Lyα photons must pass on their way to larger r. The picture we are advocating has photons scattering from the τ(Lyα) $\sim$ 1 surfaces of discrete clumps; this causes most Lyα photons to emerge from scattering events near the line center, and thus to acquire a Doppler shift characteristic of the velocity (with respect to systemic) of the most recent clump. In other words, bulk-motion-induced velocity shifts, rather than radiative transfer effects, may be most responsible for the kinematics of the observed Lyα emission line.

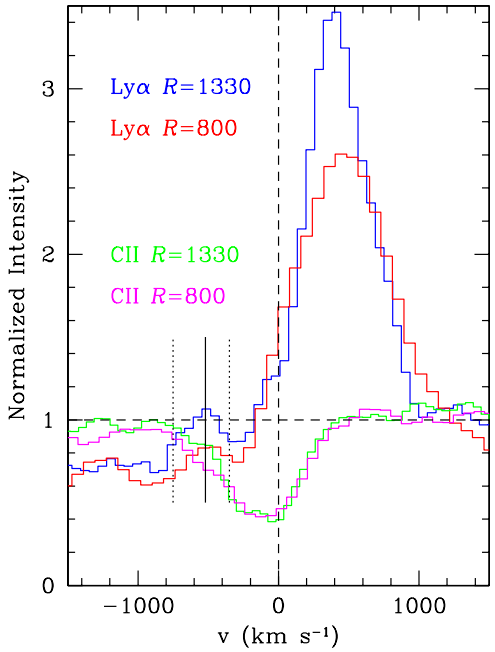

Figure 13. Comparison of two independent galaxy sample composites illustrating the presence of a weak blueshifted component of Lyα centered at $v = -520$ km s^{-1} (indicated with a solid vertical line). The blue and green histograms are the velocity profiles of Lyα and C II λ1334 for the $R = 1330$ sample, while the red and magenta histograms are the same lines for the $R = 800$ Hα sample. The position of the secondary Lyα peak corresponds to the maximum blueshifted wing of the IS line profiles.

(A color version of this figure is available in the online journal.)

In this context, the IS absorption lines provide a reasonable proxy for the velocity distribution of gas that will comprise the medium through which the Lyα photons must scatter in order to escape in the observer's direction.[15] If the flows are roughly spherically symmetric, it should be possible to seek consistency between the kinematics of Lyα emission (which would probe the kinematics of gas on the receding side of the flow) and that of the IS absorption, which samples the blueshifted, or approaching, side. The Lyα photons will be most successful in escaping the galaxy when they acquire velocity shifts well off resonance of whatever material lies between the last scattering surface and the observer. This effect would tend to produce emission from both the redshifted and blueshifted gas.

Figure 13 compares the velocity profiles of Lyα emission and C II λ1334 absorption for the same $R = 800$ and $R = 1330$ composite spectra shown in Figure 5. First, it does appear that both spectra exhibit a secondary blue peak in the Lyα emission line, with centroid velocity at $v \simeq -520$ km s^{-1} (although it is more evident in the spectrum with higher spectral resolution), close to a "mirror image" (in velocity) of the dominant redshifted emission. While the strength of this secondary feature in the composites is only $\sim$5% of the

[14] More general implications of this type of model are discussed in Section 7.

[15] Note that the velocity field information provided by the IS lines has not been exploited in any of the models mentioned above.

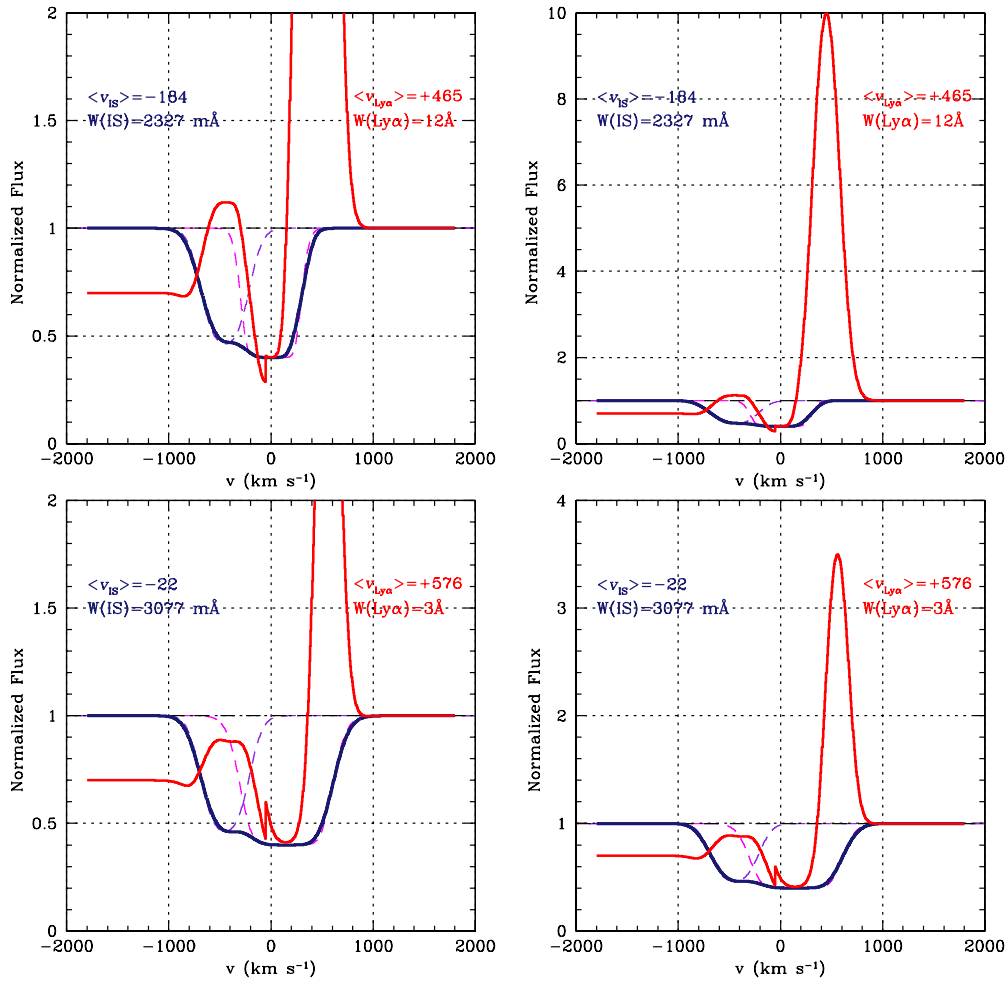

Figure 14. Examples of model spectra in which the velocity field of optically thick gas in the galaxy is assumed to be comprised of two Gaussian (in optical depth τ) components, both having a covering fraction of 0.6 (dashed profiles in each panel). The top two panels show the results for a model with one component outflowing with $v_1 = -450 \pm 150$ km s^{-1}, and an additional component with $v_2 = 0 \pm 120$ km s^{-1}; the bottom panels show a second example with $v_2 = 150 \pm 200$ km s^{-1}, with the velocity v_1 and optical depth of the outflowing component held fixed. Note how the kinematics of the material near $v = 0$ influences the measured centroids of the net absorption lines (heavy blue curve). If the same gas kinematics are assumed for H I, the predicted Lyα emission profiles as seen by an observer would resemble the red curves; the Lyα centroid is redshifted by an additional $\gtrsim$100 km s^{-1} in the bottom model as compared to the top.

(A color version of this figure is available in the online journal.)

primary redshifted component, it corresponds closely to the range of velocities seen in the most blueshifted portion of the IS C II profile, with -350 km s$^{-1} \gtrsim v \gtrsim -750$ km s^{-1}. This range also corresponds to that over which the apparent optical depth of the IS absorption is decreasing from its maximum, which extends in both composites over the velocity range -350 km s$^{-1} \lesssim v \lesssim 0$ km s^{-1}.

5.3. A Simple Kinematic Model for IS Absorption and Lyα Emission

In an attempt to produce simultaneously the salient features of the observed IS lines and Lyα emission lines, we have constructed a very schematic kinematic model following the line of reasoning outlined above, for the purposes of illustration. In the models, we assume that optically thick gas (for either low-ionization metallic species or Lyα) is present in two kinematic components, each of which is Gaussian in optical depth τ for a given transition: one component is centered near $v = 0$ and the other is outflowing with a velocity distribution $\langle v \rangle = -450 \pm 150$ km s^{-1}. We choose 450 km s^{-1} for the centroid of the outflowing component somewhat arbitrarily, but (in addition to producing line profiles that resemble the real ones) it is approximately equal to the escape velocity $v_{\rm esc}$ at the virial radius of a dark matter halo of total mass $\sim 9 \times 10^{11}\, M_\odot$ at $z \simeq 2.5$, believed to be typical of the galaxies in our spectroscopic sample (Adelberger et al. 2005b; Conroy et al. 2008; see Section 8). For the gas near the galaxy systemic redshift, we assume that the velocity distribution of the optically thick gas is similar to that of the H II regions traced by Hα emission, i.e., σ_v(Hα) $\sim$ 100 km s^{-1} (Erb et al. 2006b). All profiles have been convolved with an instrumental resolution of $R = 1330$.

Figure 14 shows example model line profiles for both IS absorption and Lyα emission, as seen by an observer on Earth (note that the right-hand panel in each case is just a zoomed-out view). One needs to provide the normalization of the τ distribution (i.e., the maximum optical depth τ_0) for both components; in the first example, the $v = 0$ component has a central optical depth of $\tau \simeq 20$, and the outflowing component has a peak at $\tau \simeq 5$.[16] The dark blue solid curve shows the expected absorption line profile (assuming that the covering fraction $f_c = 0.6$, for both components)

[16] The result is relatively insensitive to these numbers, so long as the lines are saturated.

for a saturated low-ion transition. The combination of the two assumed velocity components produces an absorption feature with a centroid $\langle \Delta v_{\rm IS} \rangle = -184$ km s^{-1} and a rest equivalent width $W_0 \simeq 2.2$ Å—close to the typical values measured for the real galaxies. A second example, in the bottom panels of Figure 14, has an identical outflowing component, but the $v \simeq 0$ component has been shifted to +150 km s^{-1} (to approximately mimic the "excess" optical depth observed in the high-$M_{\rm bar}$ sample discussed above; see Figure 11), and broadened to $\sigma_v = 200$ km s^{-1}. The centroid of the resulting absorption feature is $\langle \Delta v_{\rm IS} \rangle = -22$ km s^{-1}, in spite of the fact that the outflowing component is identical by construction, with maximum blueshifts of $v_{\rm max} \simeq -800$ km s^{-1}.

The predicted Lyα emission from the same galaxies is slightly more complex; for the moment we adopt a simple model in which the $\tau(|v|)$ distribution is assumed to be the same as for the IS absorption lines. The probability of a scattering event in which an Lyα photon is emitted by one atom and then absorbed by another with the same velocity (alternatively, one can think of it as the relative fraction of time an Lyα photon spends resonantly trapped in gas with optical depth $\tau(v)$) is roughly $\epsilon \propto \tau^2(v)$, since $\tau(v) \propto n_H(v)$, where $n_H(v)$ is the density of neutral H atoms with velocity between v and $v + dv$). The probability that a resonantly trapped Lyα photon escapes without being immediately scattered at or near the same velocity is $\propto \exp[-\tau(v)]$. Crudely, the probability that an Lyα photon is scattered by an atom with velocity v and is able to escape in the direction of an observer without additional scattering, as a function of v, is the Lyα emission profile $I(v)$,

$$I(v) \simeq C\tau^2(v)\exp\left[-\tau(v)\right], \quad (7)$$

where C is a scale factor that can be adjusted to roughly account for the destruction of Lyα photons due to dust, which we assume is proportional to the total path length traversed by a photon as it works its way out of the nebula. Finally, we assume that the Lyα photons reaching an observer who sees IS absorption profiles as in Figure 14 have been scattered toward the observer with probability of "escape" according to Equation (7). To be clear, we do not concern ourselves with how Lyα photons made it from the central H II regions to any part of the outflow—instead we simply assume that at any given moment, the relative probability for emission of an Lyα photon is proportional to $\tau^2(v)$. We do not know the spatial distribution of the outflowing gas on the redshifted side of the flow as a function of velocity, but we assume that it is spatially distinct (i.e., farther away from the observer) than the component of ISM near the galaxy systemic redshift, and that the blueshifted component is closer. Further, we assume that the outflow velocity $|v_{\rm out}|$ is a monotonic function of the galactocentric distance r on both the redshifted and blueshifted sides of the flow. We found this assumption to be necessary to obtain kinematics and spectral morphology consistent with observations; it would also follow from the assumption that the line depth at a given velocity is directly related to f_c, so that the highest-velocity material is farthest from the continuum source; see also Section 7 and Weiner et al. (2009) and Martin & Bouché (2009).

The red curves in the panels of Figure 14 were produced in this way and show the predicted Lyα emission profile for a galaxy whose absorption profile (Lyα or low-ionization metal lines) is given by the blue curve, as seen by the observer. It is worth noting that (to first order, in the absence of dust) the Lyα emission profile is not strongly dependent on gas covering fraction, since (as seen by an observer) the outflowing material is both the "source" and the "sink" for Lyα photons, both of which would be reduced by the same geometric factor. We note a number of interesting features of the predicted profiles: first, the centroids of Lyα emission and IS absorption nicely reproduce those typically observed in the galaxy sample; second, the extreme velocities of redshifted Lyα emission and blueshifted IS absorption reach 800 km s^{-1}, as for the observed galaxies; third, the model in the top panel produces a blueshifted component of Lyα emission near $v \simeq -500$ km s^{-1}—similar in both relative intensity and velocity relative to the redshifted component as in the composite spectra (see Figure 13). In the model, the secondary feature arises from photons scattered toward the observer from gas in the approaching part of the outflow; it is generally weaker than the redshifted component if there is any dust in the galaxy because photons coming from the near side of the outflow do not appear as redshifted relative to the scattering medium because they are moving in the same direction. As a consequence, blueshifted Lyα photons have generally experienced a larger number of scatterings in order to escape in the direction of the observer, thereby increasing the probability of being absorbed by dust. Finally, the apparent peak of Lyα emission is modulated primarily by the component of gas near $v = 0$—Lyα emission is more redshifted, and weaker, when the velocity range spanned by the ISM in the galaxy is broader (see also Mas-Hesse et al. 2003).

In summary, the apparent velocity of Lyα emission depends primarily on gas near the systemic redshift of the galaxy, while the extent of the red wing depends on the maximum velocity of material with appreciable column density and/or covering fraction f_c. The extent of the red wing of Lyα appears to be rather consistent over subsamples examined. The relative consistency of $\Delta v_{\rm Ly\alpha} - \Delta v_{\rm IS}$ reflects this dependency: as IS absorption lines shift toward more positive velocities, only the Lyα photons that scatter off very high velocity material on the far side of the galaxy can penetrate the H I gas in the foreground. In any case, it appears that the spectral morphology of Lyα and IS lines in rapidly star-forming galaxies may be more easily explained by the (observed) bulk velocities of outflowing IS gas, as compared to more subtle radiative transfer effects.

We return to a more physically motivated outflow model in Section 7.

6. WHERE IS THE ABSORBING GAS?

6.1. Mapping the Circumgalactic Medium

Lines-of-sight to star-forming galaxies can provide a great deal of information on the overall kinematics, chemical abundances, and (in some cases) estimates of the mass flux of cool material entrained in an outflow (e.g., Pettini et al. 2000, 2002; Quider et al. 2009, 2010). However, such observations contain little or no direct information about *where* the gas is located relative to the galaxy. A full appreciation for the physics of the outflows, and their effects on both the "host" galaxies and the local IGM, requires probing them along lines of sight from which the physical location of gas as a function of ionization level and velocity can be disentangled. In practice, this is very difficult.

In the absence of spatially resolved spectroscopy, each galaxy spectrum provides only a surface-brightness-weighted absorption profile in each observed transition, integrated along the entire line of sight from the "center" of the galaxy. Although ions of differing excitation appear to have similar velocity profiles when integrated along the line of sight, we do not have

any way of knowing, e.g., whether the bulk of the C IV ions at a particular v are distributed in the same general regions as those giving rise to C II absorption at the same velocity. The information available from the galaxy spectra themselves is necessarily crude given the relatively low S/N and spectral resolution of all but a handful of high-redshift galaxy spectra. The few high-quality spectra, of which MS1512-cB58 (Pettini et al. 2002) is perhaps the best example, show that the velocity profiles are complex, and that most of the lines accessible in lower-quality spectra are strongly saturated. If so, then interpretation of crude measures of line strength such as equivalent width (or apparent optical depth versus v) is ambiguous. The absorption arises in gas which may not be uniform across the entire continuum source. The absorbing gas may be close to the galaxy, which is typically several kiloparsecs across, and some lines of sight through the (outflowing) material may be completely absorbed, while others may be altogether free of absorption. As discussed by Shapley et al. (2003), the equivalent width of a strong line is modulated primarily by the fraction of the continuum source covered by gas giving rise to the particular transition (which controls the depth of the lines relative to the continuum) and the velocity range in the foreground gas.

Since the absorbing gas is almost certainly clumpy (e.g., the range of ionization level seen in absorption cannot coexist in the same gas, and yet they share a comparable overall velocity "envelope"), the apparent optical depth for saturated lines (as seen by an observer on Earth) arising from material at a given galactocentric radius r will depend on the characteristic physical scale of the "clumps" $\sigma_c(r)$, and their number density $n_c(r)$. The observed line strength (in the present case, the rest equivalent width W_0) will also depend on the distribution of line-of-sight velocity—large values of W_0 require a large line-of-sight velocity dispersion, the width of which depends on the sampled distribution of covering fraction. Clearly, any model for the outflows is underconstrained by the spectrum of the galaxy itself, even for high-quality spectra (e.g., Pettini et al. 2002; Quider et al. 2009).

However, high-resolution spectra of very closely spaced sightlines toward gravitationally lensed QSOs have provided constraints on the characteristic physical scales over which column densities of various transitions such as Lyα, C IV, and lower-ionization species vary significantly (Rauch et al. 1999, 2001; Ellison et al. 2004). These scales appear to be $\simeq$0.5–1 kpc for C IV (thus, comparable to the "beam footprint" of the galaxy) and $\simeq$50–100 pc for low-ionization metallic species (much smaller than the typical beam footprint). If it is assumed that the QSO spectra are sampling metal-enriched gas similar to that found near galaxies like the ones in the current sample, these scales, together with measures of covering fraction, provide some useful information on the structure of the gas in the flows. Information on the distribution of gas transverse to the line of sight breaks some of the remaining degeneracies hindering a full phase-space (velocity, position) understanding of the circumgalactic gas.

6.2. Galaxy–Galaxy Pair Samples

One method for probing the geometry of outflows is to observe foreground galaxies found near the lines of sight to background QSOs, and to compare the kinematics of absorbing gas in the galaxy spectrum with that seen in the QSO spectrum. A picture of the structure of the gaseous envelope surrounding galaxies can then be built up statistically, by observing a sample of galaxies with a range of projected galactocentric distances from the background QSOs (e.g., Adelberger et al. 2005a, 2003). This method has the advantage that one can choose the background QSOs to be very bright, so that very high S/N and spectral resolution is possible, but the disadvantage is that such QSOs are rare, and one is "stuck" with whatever galaxies happen to lie within $\simeq 1'$ of the QSO. Of course, the smallest separations (e.g., $\theta \leqslant 15''$, or a projected physical galactocentric radius of $\lesssim$120 kpc) will be especially rare. Ultimately, one is also limited by the quality of the (faint) galaxy spectrum if one is interested in a kinematic comparison using two different lines of sight through the galaxy.

An alternative and complementary method is to use close angular pairs of *galaxies* at discrepant redshifts to vastly increase the sample sizes, at the expense of information quality (because both the foreground and the background objects are faint). An initial attempt to use this method was presented by Adelberger et al. (2005a); here we investigate it using a significantly larger, higher-quality, sample of galaxy pairs drawn from an ongoing densely sampled spectroscopic survey (see Steidel et al. 2004 for early results; the full survey will be described in detail elsewhere).

The survey has been conducted over a total of 18 independent fields, 15 of which are centered on bright QSOs with $z_Q \simeq$ 2.6–2.8 (high-resolution spectra of the bright QSOs are used in Section 6.5). The spectroscopic sample includes $\gtrsim$2500 galaxy spectra in the redshift range $1.5 \leqslant z \leqslant 3.6$, with $\langle z \rangle = 2.28 \pm 0.42$. We used this galaxy survey catalog to identify pairs of spectroscopically confirmed galaxies in each of three bins in angular separation: $\theta < 5''$, $5'' < \theta \leqslant 10''$, and $10'' < \theta \leqslant 15''$, which will be identified as samples P1, P2, and P3, respectively (see Table 2). At the mean redshift of the foreground galaxies of $\langle z \rangle = 2.2$, the angular bins correspond to projected physical distances of $b \leqslant 41$ kpc, 41 kpc $< b \leqslant 83$ kpc, and 83 kpc $< b \leqslant 124$ kpc for samples P1, P2, and P3, respectively (see Table 2). The conversion from angular separation to physical impact parameter changes by only $\pm$2% over the full redshift range of the foreground galaxy samples, so that we will use angular separation and impact parameter interchangeably.

Within each pair sample, a number of additional criteria were imposed: (1) both galaxy spectra within the pair must have accurately determined redshifts; the redshift-space separation of the two galaxies in each pair must be $>$3000 km s^{-1} to ensure that their geometry is unambiguous (i.e., so that we know which galaxy is "behind" the other); and (2) the redshift separation $z_{\rm bg} - z_{\rm fg} \leqslant 1.0$ to ensure that the spectra contain a significant rest-wavelength interval in common after both are shifted to the rest frame of the foreground object. Redshifts were assigned to each galaxy using their Hα redshift if available, and otherwise using Equations (2) or (4), depending on spectral morphology. As discussed in Section 2.3, the uncertainty in the redshifts for the bulk of the galaxies in the samples is expected to be $\simeq$125 km s^{-1}. After culling, the final pair samples include 42, 164, and 306 pairs for samples P1, P2, and P3, respectively. The properties of these three angular pair samples are summarized in Table 2.

6.3. A Case Study: GWS-BX201 and GWS-BM115

Among these pair samples, there is a handful for which the spectra were of sufficient quality to be analyzed individually. One example, illustrated in Figures 15 and 16 (see also Figure 4 of Adelberger et al. 2005a), allows us to compare the IS absorption lines in the spectrum of the $z = 1.6065$ galaxy

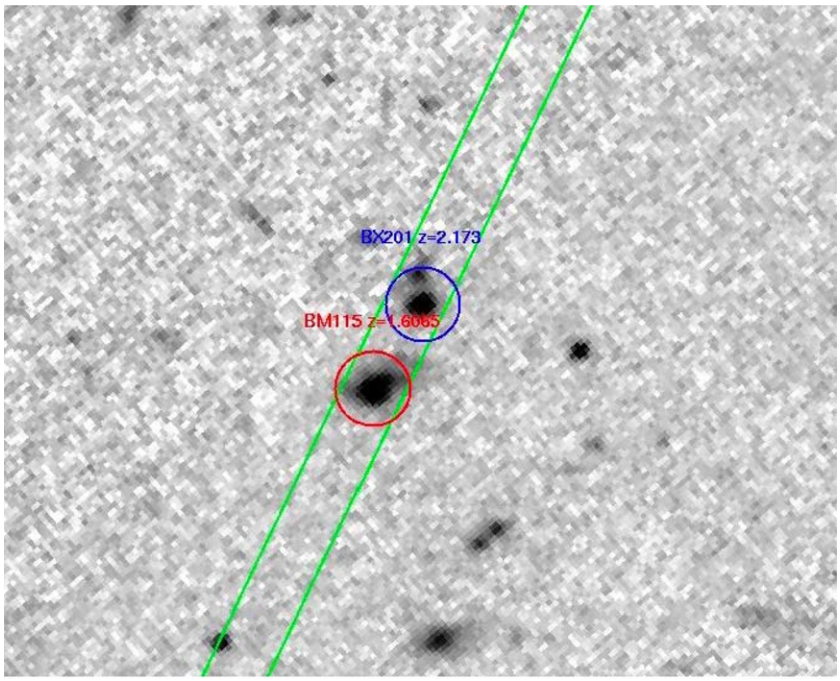

Figure 15. *HST*/ACS image of the GWS-BM115/BX201 galaxy pair, in the F814W filter. BM115 has $z_{sys} = 1.6065$, based on the Hα line observed with Keck/NIRSPEC. BX201 lies 1.″9 away on the plane of the sky, corresponding to an impact parameter at $z = 1.6065$ of $\simeq$16.1 kpc (physical). Figure 16 and Table 3 compare the IS lines observed in the spectrum of the foreground galaxy BM115 and those observed in the spectrum of BX201 at the redshift of BM115.
(A color version of this figure is available in the online journal.)

Table 2
Foreground/Background Galaxy Pair Statistics[a]

Sample	θ Range[b]	b Range[c] (kpc)	Number	$\langle\theta\rangle$	$\langle b\rangle$ (kpc)	$\langle z_{fg}\rangle$[d]	$\langle z_{bg}\rangle$[e]
P1	$< 5''$	10–41	42	$3.''8 \pm 0.''8$	31 ± 7	2.21 ± 0.32	2.64 ± 0.36
P2	$5''$–$10''$	41–82	164	$7.''6 \pm 1.''5$	63 ± 12	2.18 ± 0.36	2.64 ± 0.41
P3	$10''$–$15''$	82–125	306	$12.''5 \pm 1.''5$	103 ± 12	2.14 ± 0.33	2.65 ± 0.39

Notes.
[a] Galaxy pairs in the spectroscopic sample for which both the foreground and background galaxies have unambiguously measured redshifts which differ by > 3000 km s^{-1}.
[b] Range of angular separation of the galaxies, in arcseconds.
[c] Range of impact parameter, in physical kpc.
[d] Mean redshift for the foreground galaxies in pairs with the specified range of θ.
[e] Mean redshift for the background galaxies in pairs with the specified range of θ.

GWS-BM115 with the same features observed in the spectrum of a background galaxy projected only 1.″9 away on the plane of the sky, GWS-BX201 ($z = 2.173$). In this case, the systemic redshift of GWS-BM115 is known from Hα spectroscopy (Erb et al. 2006b), and the optical spectra of both objects were obtained with spectral resolution $R \simeq 1500$ (i.e., $\simeq$2 times higher than most of the other spectra in the sample). These galaxies have apparent magnitudes $g' = 23.5$ (BX201) and $g' = 23.7$ (BM115), $\simeq$1 mag brighter than typical galaxies in our sample. Using the systemic redshift of the foreground galaxy (GWS-BM115) measured from its Hα line, both spectra were shifted into the foreground galaxy's rest frame, and continuum normalized, to produce the comparison in Figure 16 which shows the Al II λ1670 and C IV $\lambda\lambda$1548,1550 transitions.[17] A summary of relevant measurements is given in Table 3.

[17] Because of the low redshift of BM115, there are fewer lines in common for these two galaxies than for most of the pairs in the three samples; the transitions shown are representative of low-ionization and high-ionization lines, respectively.

There are several points worth making for this particular case: first, the lines seen in the spectrum of the foreground galaxy have blueshifted centroids, with $\Delta v_{IS} \simeq -192$ km s^{-1}, which we have shown is typical of the objects in the Hα sample. Although the C IV lines are very broad (FWHM $\simeq 400$ km s^{-1} after correcting for the instrumental resolution), one can still discern a separation of the two components of the doublet. The line of sight to the background galaxy (GWS-BX201) passes the foreground galaxy at a projected physical distance (hereinafter "impact parameter," b) of $b = 16.1$ kpc. Along this line of sight, the centroids of Al II and C IV are consistent with $\Delta v_{IS} = 0$ relative to the foreground galaxy GWS-BM115—fitting the two lines of the C IV doublet and the Al II feature yields a velocity offset $\Delta v_{IS} = 0 \pm 15$ km s^{-1} and velocity width FWHM $\simeq 300$ km s^{-1} after accounting for the instrumental resolution. For both transitions, the "offset" line of sight produces lines which are significantly *stronger* (in terms of equivalent width) than those seen directly toward BM115 itself (see Table 3)! Of course, the path length through the galaxy is different in the two cases; one line of sight passes through only the "front

Table 3
Absorption Lines at z_{fg} in GWS-BX201/BM115 Pair[a]

Spectrum	$\langle b \rangle$ (kpc)	W_0(C IV 1549)[b] (Å)	W_0(Al II 1670) (Å)	Δv_{IS} [c] (km s^{-1})	FWHM[d] (km s^{-1})
GWS-BM115 ($z = 1.6065$)	0.0	2.78	1.11	-192 ± 15	400
GWS-BX201 (@$z = 1.6065$)	16.1	3.53	2.20	0 ± 18	270

Notes.
[a] For this galaxy pair, the spectra were both shifted to the rest frame of the foreground galaxy (BM115) and then evaluated with respect to $z = 1.6065$.
[b] Values include both components of the C IV doublet; the doublet ratios are 1.20 and 1.05, respectively.
[c] Velocity of IS line centroids relative to $z = 1.6065$.
[d] Velocity widths of IS lines, corrected for instrumental resolution.

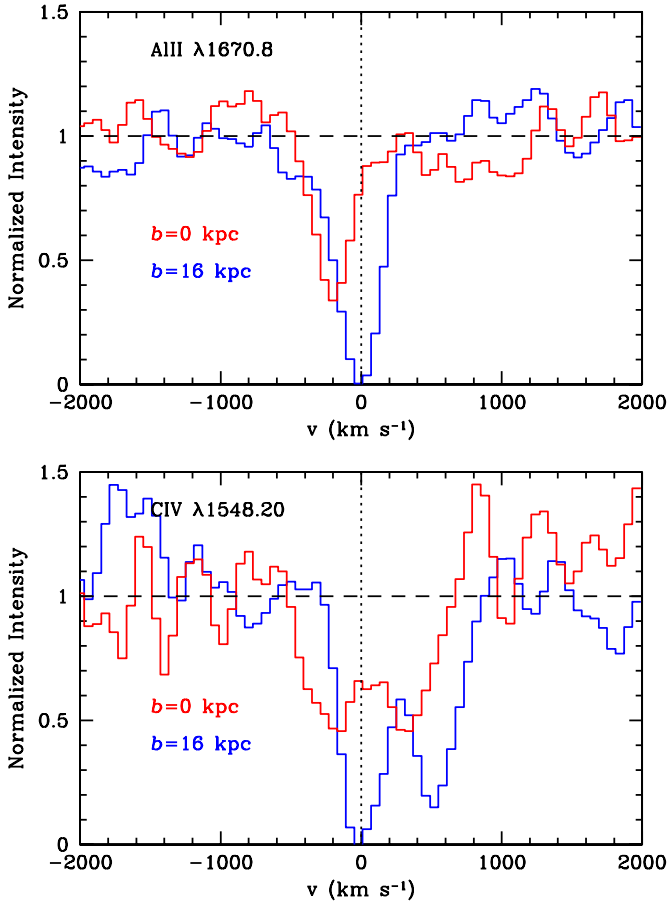

Figure 16. Comparison of the kinematics of representative IS absorption lines in the spectrum of the $z = 1.6065$ galaxy BM115 (red) to the absorption in the spectrum of the background galaxy BX201 ($z = 2.173$, 1.″9 on the plane of the sky, or a projected transverse separation of $\simeq$16 kpc at $z = 1.607$), shifted into the rest frame of BM115 using the same systemic redshift (blue). The rest wavelengths of the transitions shown are indicated (the C IV profiles are plotted with respect to $v = 0$ for the λ1548.20 line). Note that in both cases the absorption in the background galaxy spectrum is *stronger* and shifted by $\simeq +190$ km s^{-1} compared to the features in the foreground galaxy spectrum, placing the centroid very close to the foreground galaxy systemic redshift.
(A color version of this figure is available in the online journal.)

half" of whatever gas is associated with the foreground galaxy, while the sightline to the background object, although spatially offset, samples material both "behind" and "in front of" BM115 as seen by an observer on Earth. The fact that the centroid of the absorption has $\Delta v_{IS} \simeq 0$ is consistent with any picture in which material is distributed reasonably symmetrically around BM115; e.g., this would be expected for axisymmetric radial outflow from (or infall onto) BM115, reaching a galactocentric distance of at least $r_g \geqslant 16.1$ kpc.

As mentioned above, strong lines such as Al II λ1670 and C IV are very likely to be saturated; they clearly exhibit saturation along the $b = 16$ kpc line of sight, but the lines in the foreground galaxy spectrum itself do not reach zero intensity. Al II λ1670 and both components of the C IV doublet have approximately the same residual intensity of $\simeq$0.5 (Figure 16). The inference of $f_c < 1$ for cool outflowing material is not unusual, and in fact a covering fraction of $\sim$50% is quite typical of $z \sim 2$–3 galaxies (see, e.g., Shapley et al. 2003; Quider et al. 2009).

Based on the *Hubble Space Telescope* (*HST*)/Advanced Camera for Surveys (ACS) image (*I* band) shown in Figure 15, although the two galaxies have similar apparent magnitudes they have quite different surface brightness distributions: BX201 has FWHM $\simeq$ 0.″22 ($\simeq$1.8 kpc, physical), while the UV light of BM115 has FWHM $\simeq$ 0.″40 ($\sim$3.4 kpc, physical). Thus, the spectrum of BM115 itself indicates that, averaged over an area of $\simeq$10 kpc^2 centered at $b = 0$ (assuming that the intensity-weighted diameter of the light distribution is given approximately by the FWHM), but through only "half" of the outflow, only $\simeq$ 50% of the "beam" area intercepts appreciable outflowing low- and intermediate-ionization gas. The "offset" line of sight ($b = 16.1$ kpc) produces absorption reaching zero intensity in both relatively low (Al II) and relatively high (C IV) ionization gas, indicating $f_c \simeq 1$ when averaged on a scale of $\simeq$2.5 kpc^2, at a galactocentric radius of $\simeq$16.1 kpc.

It is difficult to know from observations of a single galaxy pair whether differences in the kinematics and/or depth of absorption lines arise from averaging over a smaller spatial region (e.g., a more compact background source might subtend a region within which the gas is optically thick everywhere) or from a changing gas-phase covering fraction with impact parameter *b* (such that the coherence scale of absorbing gas may be physically larger or smaller). This degeneracy is one of the disadvantages of resolved background sources. However, as we now demonstrate, it is possible to use a large *ensemble* of pairs to construct a physical picture of the size and structure of an average galaxy's circumgalactic gas distribution, again using stacked composite spectra.

6.4. Composite Spectra of Galaxy–Galaxy Pairs

Unfortunately, most of the galaxy pairs in the current spectroscopic sample are considerably fainter than the GWS-BX201/BM115 pair and were observed with somewhat lower spectral resolution. Nevertheless, the large size of the pair samples, coupled with the improved accuracy of systemic redshifts estimated from far-UV spectral features (most of the galaxies in pairs do not have Hα measurements), allow for

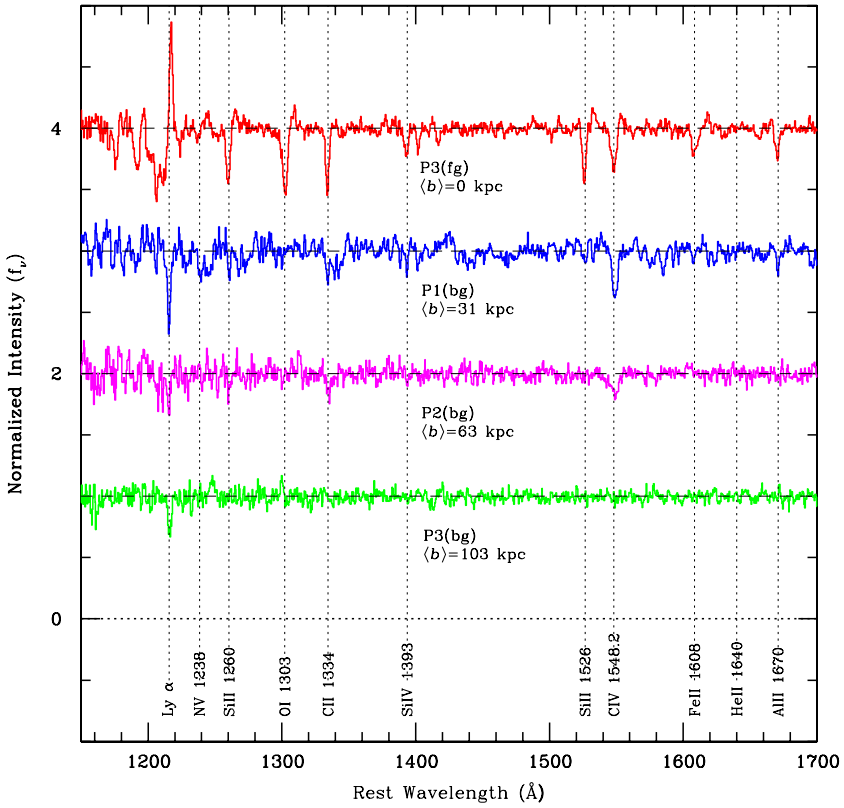

Figure 17. Comparison of the absorption lines in composite spectra formed from galaxy–galaxy pairs. The top spectrum is the composite of all foreground galaxies in pairs from sample P3 with redshift differences > 3000 km s^{-1}. The second spectrum is the composite of all *background* galaxies in pairs with angular separation $\Delta\theta \leqslant 5''$ (sample P1(bg)), formed by shifting each to the redshift of the foreground galaxy and averaging, as described in the text. The third and fourth spectra were formed the same way, for the background galaxies in pairs with $5''$–$10''$ and $10''$–$15''$ angular separations (samples P2(bg) and P3(bg)), respectively.

(A color version of this figure is available in the online journal.)

interesting measurements from composite spectra. For each angular pair of galaxies, the spectrum of the foreground galaxy in each pair was shifted to its own rest frame using the measured values of $\Delta v_{\rm IS}$ and the rules given in Equations (2) or (4), and continuum-normalized. The resulting foreground spectra were then averaged within each pair sample, producing stacked spectra which we refer to as P1(fg), P2(fg), and P3(fg), respectively. A similar approach was used to produce stacked spectra of the background galaxies: each individual background galaxy spectrum was shifted into the *foreground* galaxy's rest frame using the same systemic redshift applied to the foreground galaxy spectrum, and continuum normalized. The strong IS absorption features at the redshift of each background galaxy constitute a source of noise that can affect the composite spectrum of the background galaxies (after shifting the spectra to $z_{\rm fg}$, the lines will appear at different wavelengths for each spectrum). To minimize this effect, the strongest IS lines in each background galaxy spectrum (at the galaxy redshift, $z_{\rm bg}$) were masked when producing the average spectrum at $z_{\rm fg}$. The resulting composites P1(bg), P2(bg), and P3(bg) are shown in Figure 17, together with (for display purposes only; in the analysis below we use a distinct stack of the foreground spectra within each pair sample) the spectrum of the average of all foreground galaxy spectra in sample P3.

Figures 18, 19, and 20 show line profile comparisons of P1(bg) and P1(fg), P2(bg) and P2(fg), and P3(bg) and P3(fg), respectively, for selected transitions. Table 4 summarizes the measured rest-frame line equivalent widths for the same stacked spectra. The quoted errors on the equivalent widths in Table 4 account for sample variance, continuum uncertainties, and measurement errors based on repeated measurements with spectra formed from subsets of the data.

As might be expected, the composites P1(fg), P2(fg), and P3(fg) are very similar, since they are averages of galaxy spectra for three sets of galaxies selected using identical criteria, with very similar redshift ranges (see Table 2). Nevertheless, they are completely independent, having been formed from the spectra of distinct samples of galaxies. The differences in measured line strength for the foreground galaxy composites indicate the approximate level of sample variance ($< 10\%$ for the strongest absorption lines). It is of interest to predict what the absorption line profiles of the spectra of the foreground galaxies would look like if the line of sight were to probe the full galaxy rather than only the part in the foreground. If one assumes that the strong lines are saturated, and that the kinematics of outflowing gas are similar on the far side of the galaxy as observed on the near side, the full line profile should include a reflection of the portion of the line profile with $v < 0$ about $v = 0$. Generally, accounting for this effect increases the equivalent widths by a factor of 1.45 for low-ionization species (e.g., C II, Si II), 1.70 for Si IV, and $\simeq$2 for C IV. These factors vary because of the differing strength of the absorption near $v = 0$—typically low-ionization species have stronger $v \simeq 0$ absorption, while for C IV there is very little. The corrected values of the line strengths for the foreground galaxy spectra are also indicated in Table 4; in the discussion below, we adopt the corrected values for the $b \simeq 0$ sightlines.

The comparison in Figure 18 thus shows the difference in absorption line profiles for lines of sight at $b = 0$, and those offset by $1\farcs5$–$5''$ ($\langle\theta\rangle = 3\farcs8$, or $\langle b\rangle \simeq 30$ kpc), for

Table 4
Absorption Line Strengths at z_{fg} in Galaxy Pairs[a]

Sample	$\langle b \rangle$	Lyα	Si II 1260	C II 1334	Si IV 1393	Si II 1526	C IV 1549[b]	Al II 1670
P1(fg)	0	...	1.38 ± 0.12	1.79 ± 0.15	1.20 ± 0.12	1.34 ± 0.12	1.95 ± 0.15	0.97 ± 0.10
	0[c]	(4.7 ± 1.0)[d]	(2.01 ± 0.18)	(2.61 ± 0.22)	(2.04 ± 0.20)	(1.96 ± 0.18)	(3.90 ± 0.30)	(1.42 ± 0.15)
P1(bg)	31	2.01 ± 0.15	0.42 ± 0.06	0.90 ± 0.08	0.39 ± 0.08	0.37 ± 0.06	2.13 ± 0.15	0.40 ± 0.08
P2(fg)	0	...	1.42 ± 0.10	1.74 ± 0.15	1.12 ± 0.12	1.52 ± 0.12	1.90 ± 0.10	1.10 ± 0.12
	0[c]	(4.8 ± 1.0)[d]	(2.07 ± 0.15)	(2.54 ± 0.22)	(1.90 ± 0.20)	(2.22 ± 0.18)	(3.80 ± 0.20)	(1.61 ± 0.18)
P2(bg)	63	1.23 ± 0.20	0.41 ± 0.09	0.67 ± 0.12	0.19 ± 0.08	< 0.15	1.18 ± 0.15	< 0.20
P3(fg)	0	...	1.40 ± 0.10	1.62 ± 0.10	1.10 ± 0.12	1.41 ± 0.10	1.90 ± 0.10	1.01 ± 0.11
	0[c]	(4.9 ± 1.0)[d]	(2.04 ± 0.15)	(2.37 ± 0.15)	(1.87 ± 0.20)	(2.06 ± 0.18)	(3.80 ± 0.20)	(1.47 ± 0.22)
P3(bg)	103	0.92 ± 0.12	< 0.05	< 0.12	0.12 ± 0.06	< 0.04	0.13 ± 0.05	< 0.10

Notes.
[a] For each pair sample, the rest-frame equivalent width (in Å) for the stack of the foreground galaxy spectra are given in the first row; the results from the composite of the background spectra, shifted to rest frame of the foreground galaxy, are in the second row.
[b] Values include both components of the C IV doublet.
[c] Rest equivalent widths after applying corrections (see the text) to represent sightlines through the entire galaxy at $b = 0$.
[d] Values for Lyα at $b = 0$ are estimated from the observed strength of Lyβ absorption.

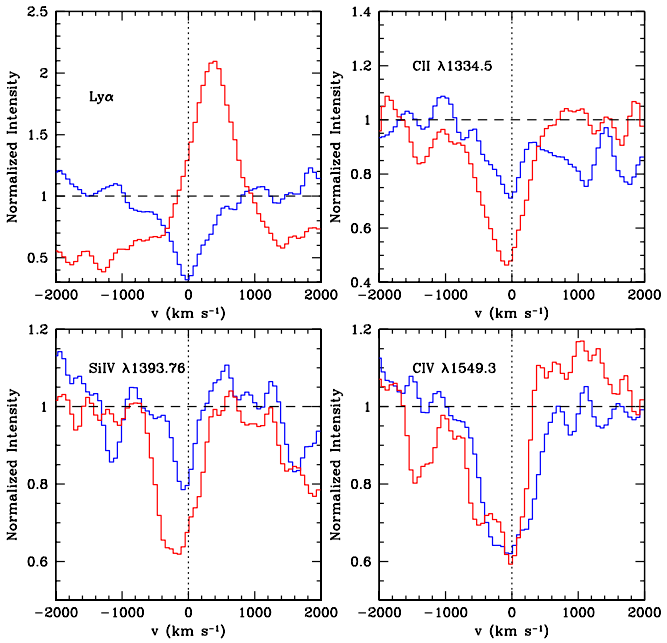

Figure 18. Comparison of the absorption profiles in the composite spectra of sample P1(fg) (red) and P1(bg) (blue). For each of the 42 pairs, the same foreground galaxy systemic redshift was used to shift both the foreground and background galaxy spectra to z_{fg}. Thus, the red curve represents the average galaxy absorption line spectrum (i.e., $b = 0$), while the blue curve is the average spectrum of the same ensemble of galaxies at mean impact parameter of $\langle b \rangle = 31$ kpc. (See Tables 2 and 4 for sample descriptions and statistics. Note that the rest wavelength of the C IV doublet blend has assumed $W_0(1548)/W_0(1550) = 1.4$.)
(A color version of this figure is available in the online journal.)

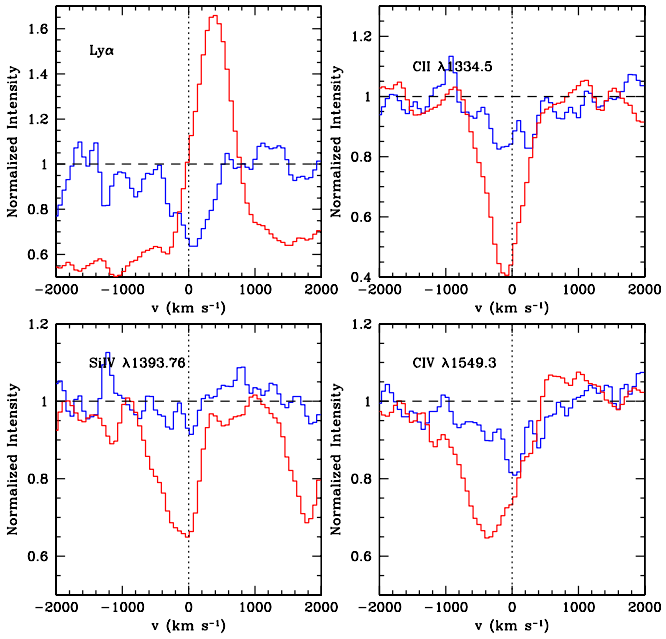

Figure 19. Same as for Figure 18, for samples P2(fg) (red) and P2(bg) (blue). In this case, the blue spectrum represents the average absorption profile at impact parameters $b = 41$–82 kpc, for the same 162 galaxies which comprise the mean galaxy spectrum in red. (See Tables 2 and 4 for sample descriptions and statistics.)
(A color version of this figure is available in the online journal.)

precisely the same set of 42 galaxies. As in the example of GWS-BM115/BX201 above, the absorption line centroids in the $\langle b \rangle \simeq 30$ kpc line of sight are close to the foreground galaxy systemic redshift. For instance, the observed Lyα absorption line in the P1(bg) spectrum has a measured wavelength of 1215.62 Å, only 12 km s^{-1} from $v = 0$; the estimated error in the line centroid from propagation of the uncertainties in z_{sys} for individual objects is $\sigma(\Delta v) \approx$ 20–25 km s^{-1}. The other lines in the P1(bg) spectrum show similar behavior, in the sense that their centroids are much closer to $v = 0$ than the same lines in the P1(fg) spectrum, which have $v \simeq -150$ to -200 km s^{-1}. It is also clear from Table 4 and Figure 18 that the strength of low- and intermediate-ionization absorption lines is significantly weaker for lines of sight with an average impact parameter of $\langle b \rangle = 31$ kpc (physical). Specifically, the strength of C II λ1334 is reduced by a factor of ∼3, and Si IV λ1393 by more than a factor of 5, for sample P1(bg) ($\langle b \rangle = 31$ kpc) relative to P1(fg). Interestingly, the strength of the C IV absorption falls much less steeply in P1(bg) versus P1(fg), declining by only a factor of ≃1.8.

The same general trend continues in the comparison of P2(fg) and P2(bg) (Figure 19 and Table 4), where P2(bg) represents an average spectrum for impact parameters $b = 41$–82 kpc with $\langle b \rangle = 63$ kpc. P3(bg), sensitive to absorption from gas with $b = 82$–125 kpc ($\langle b \rangle = 103$ kpc), has reached the point where the composite spectra formed from the low-resolution,

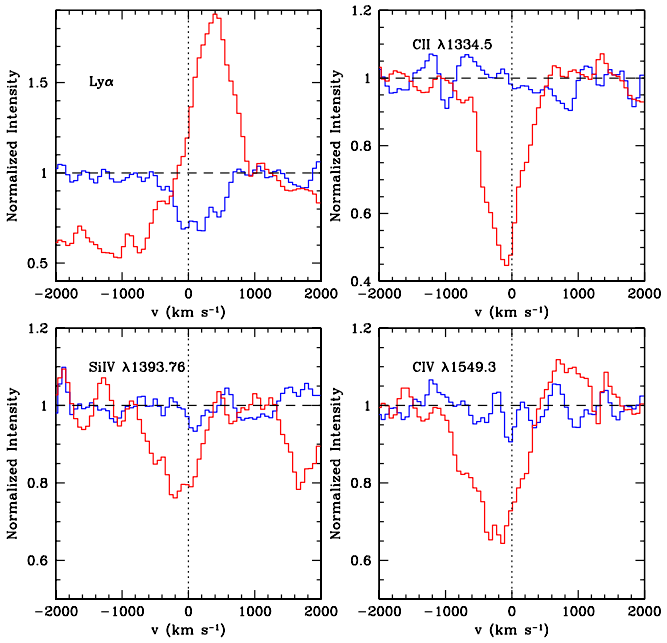

Figure 20. Same as Figure 18, for samples P3(fg) (red) and P3(bg) (blue). In this case, the blue spectrum represents the average absorption profile at impact parameters $b = 82$–125 kpc, for the same 306 galaxies which comprise the mean galaxy spectrum in red. (See Tables 2 and 4 for sample descriptions and statistics.)

(A color version of this figure is available in the online journal.)

low-S/N galaxy spectra are just barely sensitive enough to detect absorption lines other than Lyα. C IV absorption is detected with only marginal significance, and the low-ionization metal lines fall below the threshold of detectability. Interestingly, there is no significant change in the equivalent width for the Lyα absorption line between sample P2 and P3: both have W_0(Lyα) reduced by only a factor of $\simeq$2 relative to sample P1(bg). We will discuss possible explanations for this behavior in Section 7 below.

A graphical summary of the contents of Table 4 is shown in Figure 21. Points representing lines of sight with $b \simeq 0$ (i.e., P1(fg), P2(fg), and P3(fg)) have been averaged, the result of which is plotted near $b = 0$. The small error bars show that the scatter among the *independent* subsamples of foreground galaxy spectra is small. Lyβ has been used in lieu of Lyα for a measure of the strength of H I absorption in the foreground galaxy spectra, because of the contamination of Lyα absorption by Lyα emission. Because both lines probably fall on the flat part of the curve of growth, the strength of Lyα absorption is likely to be comparable to that of Lyβ.

In spite of the limited sensitivity to weak absorption lines in the composite spectra, there are several trends worth noting. The strength of Si IV and both Si II lines track each other very closely out to $b \sim 40$ kpc. This is noteworthy because it is to be expected when all three lines are strongly saturated and sample the same range of velocities; in particular, the two measured lines of Si II (λ1260, λ1526) have oscillator strengths $f = 1.18$ and $f = 0.133$, respectively. For a given column density N(Si II), the ratio of $\lambda^2 f$ for the two lines would differ by a factor of $\simeq$6.1; the fact that the equivalent widths of these two lines are equal out to $\sim$40 kpc indeed supports strong saturation. This suggests the trend toward weaker absorption with increasing b is dominated by either a decreasing velocity spread or a decreasing f_c; the galaxy spectra are not of high enough resolution to distinguish between the two. By $\langle b \rangle \simeq 63$ kpc, however, the measured Si II λ1526 line strength has decreased significantly with respect to Si II λ1260 (it is at least three times weaker) indicating that the λ1526 line is becoming unsaturated. The equivalent width ratio $W_0(\lambda1526)/W_0(\lambda1260)$ implies an average total Si II column density at $\langle b \rangle \simeq 63$ kpc of $\log N(\mathrm{Si\ II}) \simeq 13.3\ \mathrm{cm}^{-2}$. In principle, the two lines of the Si IV doublet should allow an assessment of the degree of saturation, but the Si IV λ1402 absorption line is sufficiently weak in the composite spectra that it cannot be measured with useful precision.

The other lines in Figure 21 exhibit trends similar to that of the Si lines, albeit with a shallower decline in line strength with increasing impact parameter. The equivalent widths for all of the ions in Figure 21 fall precipitously somewhere between $b \simeq 60$ and $b \simeq 90$ kpc, with the exception of Lyα. All of the species decline with galactocentric radius (or impact parameter) as $W_0 \propto b^{-\beta}$ with $0.2 \lesssim \beta \lesssim 0.6$ out to $b \sim 50$ kpc, whereas $\beta \gtrsim 1$ at larger b (again, Lyα excepted). Because of line saturation, and the fact that only relatively strong lines can be detected using low-resolution spectra of faint galaxies, we know that the trends seen in Figure 21 are dominated by a declining value of f_c with galactocentric radius, along with a smaller range of line-of-sight velocities with increasing b. Schematic models which reproduce the curves in Figure 21 are discussed in Section 7.1.

6.5. Lyα Absorption at Larger Impact Parameter

In order to trace the average Lyα absorption line strength to larger galactocentric radii ($b > 125$ kpc), we made use of the S/N $\simeq$ 40–100, high-resolution ($R \simeq 30,000$) spectra of bright QSOs lying in 15 of the galaxy survey fields introduced in Section 6.2. The QSO spectra were obtained using the HIRES spectrograph on the Keck 1 telescope, with the UV cross-disperser providing simultaneous wavelength coverage from 3100–6000 Å with very high throughput. For the time being, we degrade these QSO spectra (using only their high S/N) in order to obtain absorption line measurements analogous to those using the galaxy pairs above. As for the galaxy pairs, foreground galaxy redshifts were assigned based on Equations (2) or (4), and the spectral regions of the QSO spectra corresponding to the Lyα transition at the redshift of the foreground galaxy were extracted. The foreground galaxies were chosen to lie in two impact parameter bins: 125 kpc $\leqslant b \leqslant$ 200 kpc and 200 kpc $\leqslant b \leqslant$ 280 kpc. Within each bin, 21 QSO spectral regions were shifted into the rest frame of 21 distinct foreground galaxies, i.e., so that $v = 0$ lies at the galaxy redshift. The spectra within each bin were then averaged to obtain the mean Lyα absorption profile. The resulting composites were then continuum normalized[18] and averaged to obtain the mean Lyα absorption profile. Although the background QSOs are point sources, and therefore not suitable for measuring gas covering fraction in a single line of sight, the ensemble of QSO sightlines should provide an average absorption profile equivalent to what would be obtained using resolved background galaxies. The two new points have been added to Figure 21 to extend the measurement to $b = 280$ kpc, or an angular separation of $\simeq$34″ at $\langle z \rangle = 2.2$. The averaged spectra in the galaxy rest frame for the two bins are shown in Figure 22; the centroids of the resulting Lyα absorption features are remarkably close to $v = 0$, another indication that the estimated galaxy redshifts are relatively free of systematics (Adelberger et al. 2003).

[18] The strength of the absorption associated with the galaxies is measured relative to a new effective continuum level reduced by $\simeq$20%, the average Lyα forest decrement at $z \sim 2.2$.

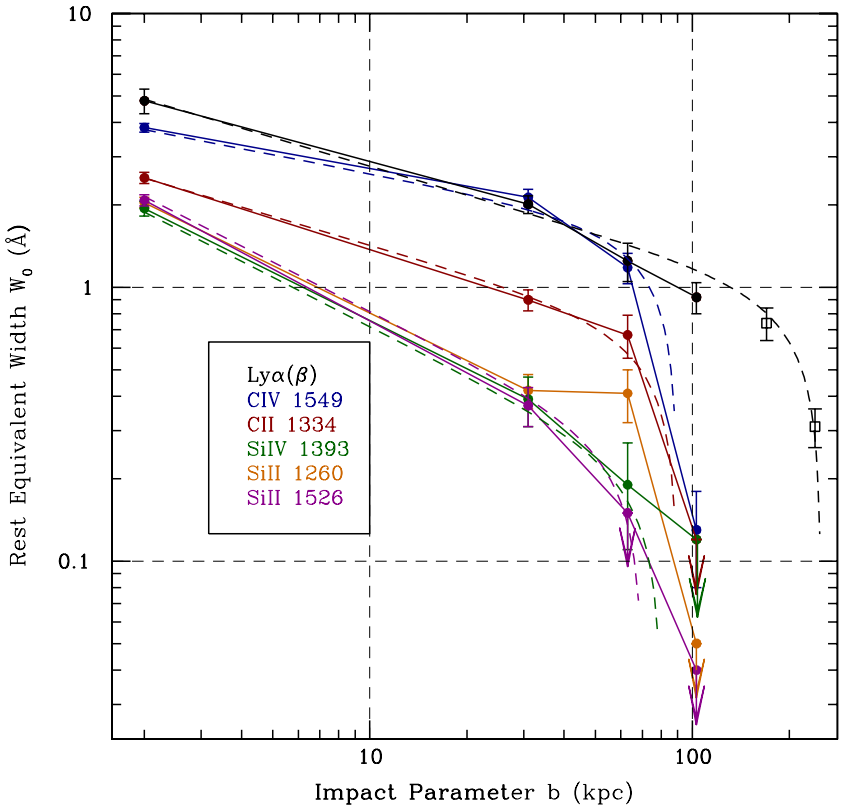

Figure 21. Dependence of IS absorption line strengths on the galactocentric impact parameter in physical kpc, for the galaxy–galaxy pair samples outlined in Tables 2 and 4. The values near $b \simeq 0$ are an average of the points for the three distinct foreground galaxy samples P1(fg), P2(fg), and P3(fg). These values have each been corrected upward to account for the estimated contribution to the line strength from the "far side" of the gas distribution, assuming symmetric kinematics of outflowing material. Each color (for points and connecting line segments) represents a different ISM transition as indicated in the box legend; downward arrows on points indicate upper limits. The dashed curves using the same color coding are predictions for $W_0(b)$ using the model described in the text (summarized in Table 5). The two points for Lyα represented by open squares were measured from HIRES spectra, as described in the text. The corresponding spectra are plotted in Figure 22.

Returning to Figure 21, the high-quality HIRES spectra have allowed us to extend the W_0 versus b relation for Lyα to see the point where the line strength decreases rapidly, evidently $b \simeq 250$ kpc. It seems likely that the rapid falloff in W_0 indicates that Lyα is becoming optically thin. Indeed, under this assumption, the line strength in the bin with the largest b is $W_0 = 0.31 \pm 0.05$ Å, which would correspond roughly to log N(H I) $\simeq$ 13.25. Thus, as for the metal line transitions, a combination of decreasing covering fraction and linear curve of growth effects steepens the W_0 versus b relation.

We now explore the possibility that a simple schematic outflow model might reasonably reproduce the observations of both the $b = 0$ constraints (line strength and line shape in galaxy spectra) and the observed variation of absorption line strength with impact parameter.

7. A SIMPLE MODEL FOR OUTFLOWS AND CIRCUMGALACTIC GAS

7.1. Line Strength and the Spatial Extent of Circumgalactic Gas

Assuming a spherically symmetric gas flow with (galactocentric) radial velocity outward, $v_{\rm out}(r)$ (note that this is not a "shell"), the strength of absorption lines produced by material along an observer's line of sight at impact parameter b will depend on the line-of-sight component of $v_{\rm out}$ and on the radial and velocity dependence of the covering fraction, $f_c(r, v)$. For the moment, we characterize the rapid falloff at some galactocentric radius $R_{\rm eff}$ (which may differ for each ionic species) as an "edge" beyond which no absorption would be detected.

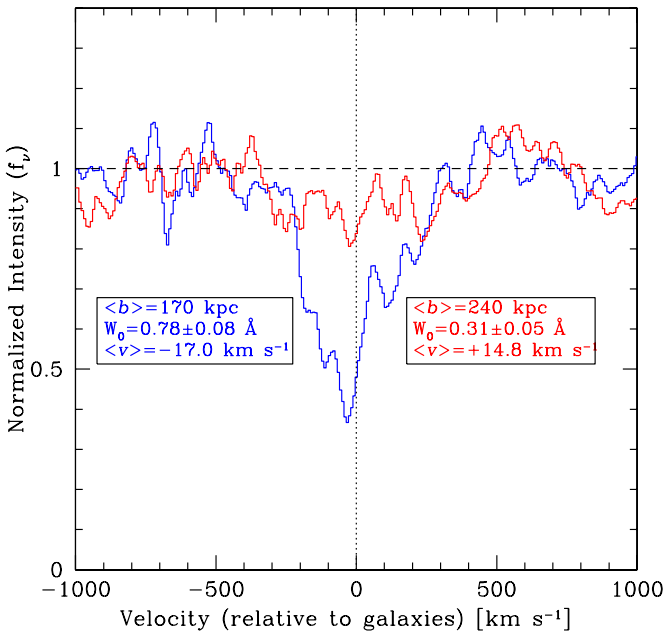

Figure 22. Average spectrum near Lyα in regions of HIRES spectra centered on the systemic redshifts of galaxies with QSO line-of-sight impact parameters of 120 kpc $\leqslant b \leqslant$ 200 kpc (blue; $\langle b \rangle = 170$ kpc) and 200 kpc $< b \leqslant$ 280 kpc (red; $\langle b \rangle = 240$ kpc). Each spectrum represents an average of 21 galaxy–QSO sightline angular pairs. The centroid velocities are very close to $v = 0$, indicating that our estimates of the galaxy systemic redshifts are accurate. The equivalent widths fall on an extrapolation to larger b of the relationship obtained from galaxy pairs.

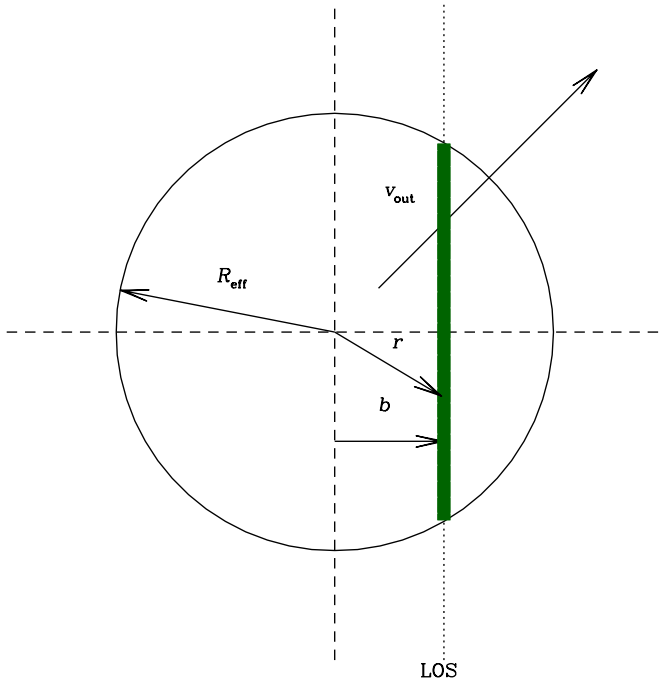

Figure 23. Diagram illustrating the simple model for estimating the relative IS absorption line strength W_0 as a function of impact parameter b used to produce the model curves in Figure 21. R_{eff} is the characteristic size of the gas distribution producing saturated lines of a particular transition. Any systematic dependence of v_{out} on radius has not been included in this model, but the covering fraction f_c of gas giving rise to the transition of interest is assumed to have a radial dependence $f_c(r) \propto r^{-\gamma}$ (see the text for additional details).
(A color version of this figure is available in the online journal.)

Modeling the effective value of the covering fraction (and the resulting line equivalent width) for gas along an observed line of sight must include an assumption about the radial dependence of the outflow velocity of absorbing material $v_{out}(r)$ and $f_c(r, v)$, where the radial coordinate r takes on values between b and R_{eff}, as illustrated in Figure 23. For a saturated transition, the observed line profile (normalized intensity I versus velocity) is given by

$$I(v) = 1 - \int f_c(r, v) dl, \quad (8)$$

where v is the line-of-sight component of $v_{out}(r)$ relative to the galaxy systemic redshift, and the integral is evaluated along the line of sight (shaded region in Figure 23). If the form of $v_{out}(r)$ is assumed, one can then associate a line-of-sight component of velocity (v) with each value of r along the sightline so that $f_c(r, v)$ becomes a function of only one variable (either r or v). The line strength is then given by the integral of $I(v)$ evaluated between the minimum and maximum line-of-sight velocity expected. For a velocity field which has v_{out} increasing with r, the extreme velocities expected would be

$$|\Delta v_{\max(b)}| = v_{out}(R_{eff})\left[1 - b^2/R_{eff}^2\right]^{1/2} \quad (9)$$

and the associated equivalent width (with continuum normalized to unity) is just

$$W_0(v) = 2\int_0^{\Delta v_{max}} f_c(v) dv \quad (10)$$

which can be integrated over the wavelength to give the expected absorption line equivalent width. Assuming for the moment that

Table 5
W_0 versus b Model Parameters[a]

Line	γ[b]	R_{eff} (kpc)	v_{out}	$f_{c,max}$[c]
Lyα(1216)	0.37	250	820	0.80
C IV(1549)	0.23	80	800	0.35/0.25[d]
C II(1334)	0.35	90	650	0.52
Si II(1526)	0.60	70	750	0.40
Si IV(1393)	0.60	80	820	0.33

Notes.
[a] Parameters used to produce the model curves shown in Figure 21.
[b] Power-law exponent in the expression $f_c(r) = f_{c,max} r^{-\gamma}$.
[c] Maximum value of the covering fraction for each transition, measured from the composite spectrum (see Figure 8).
[d] Includes contributions from C IV λ1548 and C IV λ1550 of 0.35 and 0.25, respectively.

$f_c(r) = f_{c,max} r^{-\gamma}$, and that $v_{out}(r)$ is constant, one can adjust the values of v_{out}, γ, and R_{eff} in order to reproduce the observed $W_0(b)$ for each species. The maximum covering fraction $f_{c,max}$ can be measured from the stacked spectra of the foreground galaxies—it is just the maximum depth of the absorption lines relative to the continuum for each species. These have been measured from an average of all three foreground galaxy samples, P1(fg), P2(fg), and P3(fg), and collected in Table 5. Table 5 also contains the parameter values used to produce the model curves shown in Figure 21 for each species.

The examples plotted using dashed lines in Figure 21 show that the model does a reasonable job reproducing the relatively shallow dependence of W_0 on b, and the steep decline at $b \simeq 70$–250 kpc (depending on the transition). The best values of γ are in the range $0.2 \leqslant \gamma \leqslant 0.6$, depending on the transition (Table 5); note that the assumption of $f_c(r) \propto r^{-2}$, which would apply if the absorbing clouds retained the same characteristic physical size as they move to larger r, appears strongly ruled out by the relatively shallow observed dependence of W_0 on b.[19] Obviously, a distinct "edge" to the gas distribution at some radius R_{eff} is not physical; however, this radius could, e.g., mark the point at which a transition is becoming optically thin, so that both declining covering fraction and decreasing optical depth lead to a rapid diminution of W_0 with b. This explanation could also account for the fact that Lyα does not exhibit a break in the near-power-law dependence of W_0 on b until $b \sim 250$ kpc: Lyα remains strongly saturated as long as $\log N(\mathrm{H\,I}) \gtrsim 14.5$, so that geometric dilution dominates over changes in optical depth to radii beyond the limit of sensitivity for the galaxy–galaxy pair samples; even with unity covering fraction a rest equivalent width of $\simeq$0.9 Å would correspond to a saturated Lyα line.

For this particular model in which v_{out} is independent of galactocentric radius r, the combination of the measured $f_{c,max}$ and v_{out} control the overall normalization, while the slope of the W_0 versus b function is dictated entirely by the choice of γ. As shown in Table 5, Lyα, C IV, and Si IV are best matched if $v_{out} = 800$ km s^{-1}, while Si II and C II suggest $v_{out} = 750$ km s^{-1} and $v_{out} = 650$ km s^{-1}, respectively. The fact that the latter two values are somewhat lower may be related to the influence of (non-outflowing) absorption near $v = 0$ on the measurement of $f_{c,max}$ (see discussion in Section 4); for example, changing the

[19] It turns out (perhaps counter-intuitively) that the power-law slopes relating W_0 and b in the model curves in Figure 21 are very close to the power-law index γ assumed in the expression for $f_c(r)$ because of the relationship between impact parameter b and the line-of-sight dependence of the sampled velocity range.

value of $f_{c,\max}$ for C II from 0.52 to 0.42 (i.e., by less than 20%) favors $v_{\rm out} = 800$ km s^{-1} rather than $v_{\rm out} = 650$ km s^{-1}.

So far, the model has made a number of idealized assumptions: spherical symmetry, uniform outflowing velocity field (we will assess the validity of this assumption in Section 7.3), radial dependence of the covering fraction $f_c(r) \propto r^{-\gamma}$, and saturated lines whose equivalent widths are controlled by the covering fraction coupled with the range of velocities expected to be sampled along the line of sight. It is worth a cautionary reminder at this point that $W_0(b)$ for a particular transition cannot be converted unambiguously into a map of total column density versus b so long as the lines remain optically thick. Instead, one measures the average covering fraction of gas hosting that particular ion; conversely, when the optical depths become of order unity it becomes feasible to measure total column density, but at that point the constraints on covering fraction are diminished.

As mentioned above, C IV, with $\gamma \simeq 0.20$, has a much more gradual decline with b than Si II and Si IV. This behavior might be attributed to a changing ionization state of more diffuse gas entrained in the outward flow, so that "new" pockets of gas become more likely to absorb in C IV as the flow becomes more diffuse at larger radii (i.e., it is not just the same "clouds" with larger cross section). The strength of C IV absorption often appears "de-coupled" from the strength and depth of the lower-ionization species in galaxy spectra (see Shapley et al. 2003), which may be related to the very different radial distribution of absorbing gas inferred above, as well as to the much larger physical coherence scale of C IV-absorbing gas compared to gas giving rise to lower-ionization species observed in high-resolution studies of very small separation lines of sight. Nevertheless, C IV absorption usually spans a very similar range of blueshifted velocities in the galaxy spectra, strongly suggesting that it is being carried in the same outflow. The quality of the present data does not justify a more detailed analysis.

7.2. Total Absorption Cross Section

A very simple (and model-independent) calculation that can be made using the information collected in Figure 21 is the expected incidence of absorption lines exceeding a particular threshold in W_0 associated with extended gas around galaxies similar to those in the current sample. This exercise is the converse of one undertaken many times in the past for various types of QSO absorbers; typically, one takes an observed value of dN/dz, the number of systems observed per unit redshift, and calculates the galaxy cross section and number density required to account for the rate of incidence, assuming the cross section is all contributed by galaxies. In the present case, we have a well-defined population of galaxies, uniformly selected, with a well-established far-UV luminosity function. Reddy & Steidel (2009) have produced the most up-to-date luminosity function, determined from the same data set and using the same selection criteria as the galaxies used in the galaxy–galaxy pair analysis. They found that a Schechter function with $\phi^* = (2.75 \pm 0.54) \times 10^{-3}$ Mpc^{-3}, $M^* = -20.7$, and $\alpha = -1.73 \pm 0.07$ is a good description of the rest-frame 1700 Å luminosity function of UV-selected galaxies in the redshift range $1.9 \leqslant z \leqslant 2.7$. Integrating this function only over the luminosity range of the actual spectroscopic sample (i.e., to $\mathcal{R} \leqslant 25.5$, which corresponds to $L \sim 0.3L^*$ at $\langle z \rangle = 2.3$), the number density is $n_{\rm gal} \simeq 3.7 \times 10^{-3}$ Mpc^{-3}. Taking $b \simeq 90$ kpc as the point where W_0(C IV λ1548) $\simeq 0.15$ Å (see Figure 21), at the mean redshift of the foreground galaxies, the co-moving cross section for absorption per galaxy is $\sigma_{\rm gal} \simeq 0.26$ Mpc^2. The relevant co-moving path length per unit redshift at $\langle z \rangle = 2.20$ is $l \simeq 1320$ Mpc, so that the expected number of W_0(C IV) > 0.15 Å absorption systems[20] per unit redshift is

$$\frac{dN}{dz}(\text{C IV, pred}) \simeq (3.7 \times 10^{-3}) l \sigma_{\rm gal} \simeq 1.1. \quad (11)$$

The observed incidence of C IV systems at the same equivalent width threshold at $z \simeq 2.2$ is $dN/dz(\text{obs}) = 2.44 \pm 0.29$ (Sargent et al. 1988; Steidel 1990a), so that galaxies *in the current spectroscopic sample alone* account for ∼45% of strong C IV systems at $z \sim 2$. Although the statistics for the incidence of other lines are not as well established, Steidel & Sargent (1992) found that, for the C II λ1334 absorption with $W_0 \geqslant 0.15$ Å and $\langle z \rangle = 2.35$,

$$\frac{dN}{dz}(\text{C II, obs}) \simeq 0.94 \pm 0.33. \quad (12)$$

At face value, since the extent of C II is approximately the same as C IV (Table 5 and Figure 21), comparison with Equation (12) suggests that essentially all C IIλ1334 absorption with $W_0 > 0.15$ Å is within ≃90 kpc (physical) of a galaxy similar to those in the sample used here. The presence of strong C II absorption generally depends on the self-shielding provided by H I with $\log N \gtrsim 17.2$ (e.g., Steidel 1990b), so that although we cannot measure N(H I) from the galaxy pair spectra, one might expect a similar cross section for Lyman limit system (LLS) absorption. According to Steidel (1992),

$$\frac{dN}{dz}(\text{LLS, obs}) \simeq 1.4 \quad (13)$$

at $z \simeq 2$, suggesting that the total absorption cross section of these galaxies accounts for as much as ∼70% of all LLS absorption at similar redshifts.

It is important to emphasize that the absorption line statistics obtained using galaxies as background sources should be identical to what would be obtained using QSOs, in the limit of a suitably large number of QSO sightlines. In other words, a given average rest-frame equivalent width would be obtained at the same characteristic impact parameter from a galaxy, independent of the morphology of the background probes. It follows from the above discussion that most of the cross section for strong low-ionization metal-line absorption (and by extension, LLSs) is provided by rapidly star-forming galaxies, at least at $z \simeq 2.2$. A very similar connection between strong QSO absorbers and rapid star formation has been observed recently by Ménard et al. (2009), who used a very large sample of $W_0 > 0.7$Å Mg II absorbers (in Sloan Digital Sky Survey (SDSS) QSO spectra) over the redshift range $0.4 \lesssim z \lesssim 1.2$, and compared with the stacked [O II] λ3727 emission signature detected within the SDSS fibers. These authors conclude that the strong absorption is tightly correlated with the presence of a rapidly star-forming galaxy within ≃50 kpc of the QSO sightline. By way of comparison, the statistical impact parameter for producing C II absorption with $W_0 \geqslant 0.7$ Å at $\langle z \rangle = 2.2$ is $b \leqslant 60$ kpc.

We now turn to additional consistency checks by combining the spatial information from the preceding discussion with information extracted from the profiles of the IS absorption lines in the $b = 0$ spectra of typical LBGs.

[20] This equivalent width threshold is roughly equivalent to systems having $\log N$(C IV) $\gtrsim 13.5$ cm^{-2}.

7.3. Constraints from IS Absorption Line Profiles

From the previous section, the galaxy pair data indicate a covering fraction of absorbing gas with a radial dependence $f_c(r) \propto r^{-\gamma}$, with $0.2 \lesssim \gamma \lesssim 0.6$. All measured lines except Lyα have dropped below the current detection limit for W_0 by $b \simeq 100$ kpc; for larger impact parameters, spectra of higher resolution and S/N are required—these measurements are being made using the bright QSO sightlines in each of the survey fields (e.g., O. Rakic et al. 2010, in preparation; G. C. Rudie et al. 2010, in preparation). If we focus for the moment on scales $r \leqslant 125$ kpc, the dominant importance of the covering fraction in modulating absorption line strength means that there are only weak constraints on changes in total column density with radius. However, the kinematics of the absorption lines observed along sightlines at $b = 0$—the spectra of the galaxies themselves—provide a means of checking the models for consistency. Ideally, one should be able to reproduce the absorption line shape (i.e., covering fraction as a function of velocity) using a model for $v_{\rm out}(r)$ and $f_c(r)$ consistent with the observations of both direct and offset lines of sight.

The boundary conditions provided by the direct line-of-sight ($b = 0$) observations are that the maximum observed $|\Delta v_{\rm IS}|$ should be $\simeq$800 km s^{-1}, the maximum covering fraction is typically smaller than unity, and the line shapes generally imply that larger blueshifted velocities are associated with gas having smaller covering fraction. As we have shown, the simplest (although probably not unique) physical explanation would be that the higher-velocity gas is located predominantly at larger radii[21] (see also Weiner et al. 2009; Martin & Bouché 2009). Since the outflows are believed to be driven by energy and/or momentum originating in the inner regions of the galaxy, a plausible model might have the acceleration experienced by a gas cloud depend on the galactocentric distance r. The details of this dependence are likely to be complex, since the force experienced by cool gas clouds would depend on the energy and/or momentum acquired by the gas, the ambient pressure gradient, the radial dependence of the clouds' physical sizes,[22] and the entrainment of ambient gas in the flow (sometimes referred to as "mass-loading") as it moves outward.

In an idealized picture of a multiphase outflow, gas clouds, perhaps pressure confined by a hotter, more diffuse gaseous medium, are accelerated by thermal and/or radiation pressure to larger radii and higher velocities. The fact that the inferred radial dependence of the absorbing gas covering fraction remains at $f_c(r) \propto r^{-\gamma}$ with $\gamma \leqslant 0.6$ (at least for radii $r < R_{\rm eff}$) implies that the clouds must expand as they move out (otherwise $f_c(r) \propto r^{-2}$). Even the most steeply declining species, with $\gamma \simeq 0.6$, requires that the total cross section for absorption per cloud increases as $\sigma_c \propto r^{4/3}$, or that the characteristic cloud size $R_c(r) \propto r^{2/3}$. For clouds of constant mass $M_c = 4/3\pi R_c^3 \rho_c$ and assumed pressure gradient $p(r) \propto r^{-2}$, maintaining local pressure equilibrium leads to the same dependence, $R_c \propto r^{2/3}$; thus, the behavior of $f_c(r)$ for Si II and Si IV is very close to what one might expect for cooler, denser "cloudlets" confined by a hotter medium whose pressure decreases with galactocentric radius. One might think of the clouds giving rise to low-ionization absorption as "expanding bullets," surviving as long as there is sufficient ambient pressure to confine them, or until they expand to the point that they no longer produce significant low-ionization absorption (see Schaye et al. 2007 for additional observational evidence of such phenomena).

D.K. Strickland (2009, private communication) has suggested that the force experienced by cool clouds in a wind model obeying local pressure equilibrium would have radial dependence $F(r) \propto r^{-4/3}$; this is precisely what would be expected under the circumstances described above (i.e., $R_c \propto r^{2/3}$ and $p(r) \propto r^{-2}$). For clouds of constant mass, the radial dependence of cloud acceleration $a(r)$ would have the same form as $F(r)$; if additional mass (e.g., ambient ISM) is entrained in the wind, then $a(r)$ would decrease more rapidly with increasing radius. Once the radial dependence of cloud acceleration is specified, one obtains $v_{\rm out}(r)$, and thus $f_c(v)$, the expected velocity dependence of the covering fraction.

Rather than develop a more detailed model for the physics of the multiphase outflowing material (which is beyond the scope of the current work), for simplicity we parameterize the cloud acceleration $a(r)$ as

$$a(r) = Ar^{-\alpha}, \tag{14}$$

where A is a constant, and seek the value of α that can reproduce the IS line profiles given $f_c(r)$ inferred from the galaxy–galaxy pair data (Figure 21 and Table 5). Using this parameterization of $a(r)$,

$$a(r) = Ar^{-\alpha} = \frac{dv(r)}{dt} = \left[\frac{dv(r)}{dr}\right]\left(\frac{dr}{dt}\right) = v(r)\left(\frac{dv}{dr}\right). \tag{15}$$

Assuming the clouds are "launched" from $r = r_{\rm min}$, Equation (15) can be rearranged and integrated to provide an expression for $v_{\rm out}(r)$:

$$v_{\rm out}(r) = \left(\frac{2A}{\alpha - 1}\right)^{0.5}\left(r_{\rm min}^{1-\alpha} - r^{1-\alpha}\right)^{0.5}. \tag{16}$$

The constant A can be obtained by using the boundary condition provided by $|v_{\rm max}|$, which is the velocity at which $f_c(r)$ approaches zero[23] and the value of $R_{\rm eff}$ estimated for the transition of interest (Table 5).

We are now in a position to attempt to match observed IS absorption line profiles while simultaneously adhering to the observationally inferred form of $f_c(r)$. For simplicity, we assume that the spectra of galaxies sample their own outflow kinematics at $b = 0$ (i.e., we ignore the spatial extent of the galaxy continuum and treat observed spectra as a spatial average over a region typically 2–3 kpc in diameter).

For demonstration purposes, an absorption component is added to the outflow profile at $v = 0$ with a maximum covering fraction varied to reproduce the $v > 0$ portion of the line profile. The width assigned to this component is taken to be the same as the nebular line width associated with the H II regions in a typical galaxy ($\sigma \simeq 100$ km s^{-1}). Figure 24 shows a comparison of the predicted velocity profiles for an IS line given the above model (assuming that $r_{\rm min} = 1$ kpc), compared to the observed velocity profile of the C II 1334.53 line in the composite spectrum of $z \sim 2$–3 LBGs with $R \simeq 1330$. Also shown in Figure 24 are the

[21] Note that the simple models presented in Section 5 assumed a monotonic relationship between physical location and velocity to simultaneously explain the kinematics of observed Lyα emission and IS absorption.

[22] Recall that the radial dependence of the covering fraction is inconsistent with clouds maintaining the same size; we show below that the cloud dimensions R_c must increase with r.

[23] In other words, this is the maximum velocity beyond which the covering fraction is too small to produce absorption that can be distinguished from the continuum.

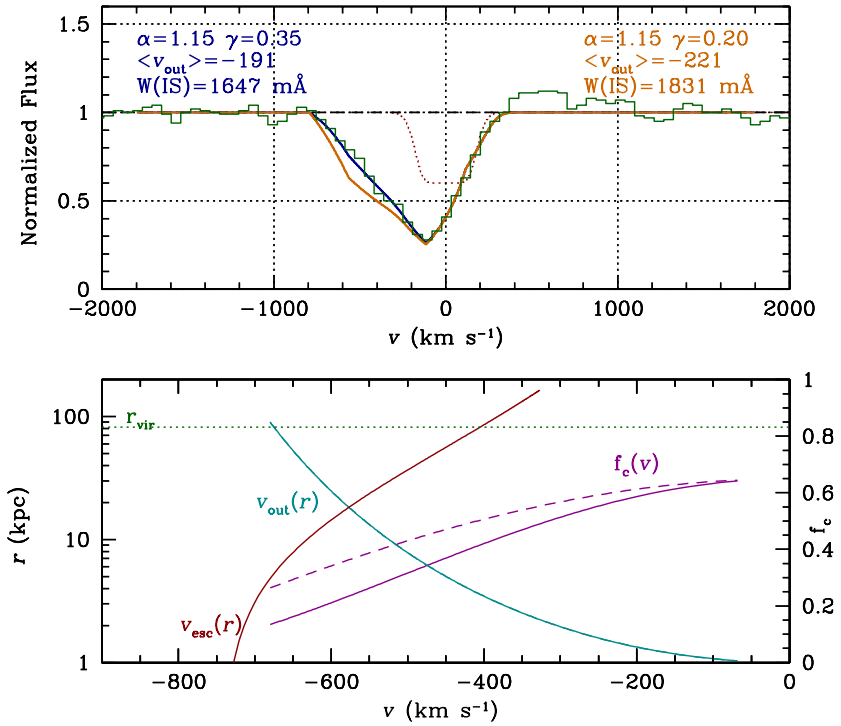

Figure 24. Top: model line profiles (convolved with the appropriate instrumental resolution) for an IS absorption line with radial covering fraction $f_c(r) \propto r^{-\gamma}$, maximum covering fraction for outflowing material $f_{c,\max} = 0.59$, and radial cloud acceleration $a(r) \propto r^{-\alpha}$, compared to the C II λ1334.53 profile from a composite of $R = 1330$ galaxy spectra. Two models are plotted, both of which include an absorption component with $v = 0$, $\sigma_v = 80$ km s^{-1}, and $f_{c,\max} = 0.4$: the dark blue profile assumes $\gamma = 0.35$ as inferred from the galaxy pair measurements for the C II line, and $\alpha = 1.15$, which provides a good match to the observed line shape. The orange curve represents the model line profile if $\gamma = 0.2$ and all other parameters are held fixed. Note that the relatively small change in γ produces a line profile inconsistent with the data, with a high-velocity wing that is too strong. Both are constrained to have $v_{\max} = -700$ km s^{-1} at the point where the line profile becomes indistinguishable from the continuum. The covering fraction of outflowing material is assumed to go to zero at $r = R_{\rm eff} = 90$ kpc. Bottom: dependence of the covering fraction (purple, right-hand axis) $f_c(v)$ and the relation between $v_{\rm out}$ and galactocentric radius r (cyan, left-hand axis). The solid curves correspond to the dark blue profile, with the dashed curves indicating values for the orange profile. Note that the velocity profiles are identical for the two models, since they use the same value of α. The red curve shows the estimated escape velocity as a function of galactocentric radius r for an NFW halo of mass $9 \times 10^{11}\ M_\odot$; the green dotted line is the virial radius $r_{\rm vir}$ for the same halo. Note that at $r = r_{\rm vir}$ (in the context of this model) the outflow velocity exceeds $v_{\rm esc}(r_{\rm vir})$.

resulting relationships between r and v and between f_c and v. The values of γ were chosen based on the models (Table 5) that adequately describe how W_0 varies with b for the relevant ion: a self-consistent kinematic model may be obtained for $\gamma = 0.35$ (the value inferred for C II λ1334; see Table 5) if $\alpha = 1.15$. To provide some intuition on how the line profile would be altered with different parameter values, the predicted profile with α held fixed and $\gamma = 0.20$ instead of $\gamma = 0.35$ is also plotted. It shows that assuming an incorrect value for the radial dependence of f_c leads (in this case) to an absorption feature that has too much apparent optical depth at high values of $|v|$ and therefore significantly overpredicts the values of $|\langle v_{\rm out}\rangle|$ and W_0.

By altering the maximum covering fraction of the outflowing gas and the optical depth and covering fraction of the $v = 0$ component, it is possible to reproduce a wide range of observed line profiles. Figure 25 (dark blue model profile) shows another example with α chosen to produce a very strong line with a large blueshifted centroid such as those observed in the spectrum of the lensed LBG MS1512-cB58 (Pettini et al. 2002). In this case, it was necessary to change $f_{c,\max}$ to unity and to adjust the function $a(r)$ to be steeper than for the example in Figure 24. Since the line is again C II λ1334.53, once again $\gamma = 0.35$. The orange model profile is that obtained when all parameters are held fixed but α is reduced to the value that provided a good fit to the profile in Figure 24. Qualitatively, as the function $a(r)$ becomes steeper, the covering fraction at high velocity increases along with the line equivalent width (given the imposed boundary conditions); the physical meaning of a steeper $a(r)$ is that material is accelerated more rapidly, such that it reaches high velocity before it becomes geometrically diluted.

The bottom panels of Figures 24 and 25 are also interesting to consider. They show that, at least in the context of the current models, the outflowing gas attains close to its maximum velocity within ∼3–10 kpc (depending on the model) of the center of the galaxy, where whatever mechanism is at work in accelerating the clouds is most effective. At larger radii, the outflow velocities change slowly with increasing radius. Recall that our simple model for inferring $f_c(r)$ from W_0 versus b assumed that $v_{\rm out}$ is independent of r. Since the current model requires $a(r) = dv_{\rm out}(r)/dt \propto r^{-\alpha}$ with $1.15 \lesssim \alpha \lesssim 1.95$, most of the acceleration up to the maximum observed velocity occurs when $r \ll 10$ kpc. Thus, we conclude that having assumed a fixed $v_{\rm out}$ as in Section 7.1 was justified, given other sources of uncertainty.

We caution that in the particular family of models described above, the parameters γ and α are covariant and combinations of the two can usually be found that will adequately reproduce observed IS line profiles. It is only because we have information on the radial dependence of $f(r)$ from the galaxy–galaxy pairs (constraining γ) that anything like a unique solution results. Since the value of γ is statistical (and so may not apply for particular individual galaxies) it would be unwise to read too

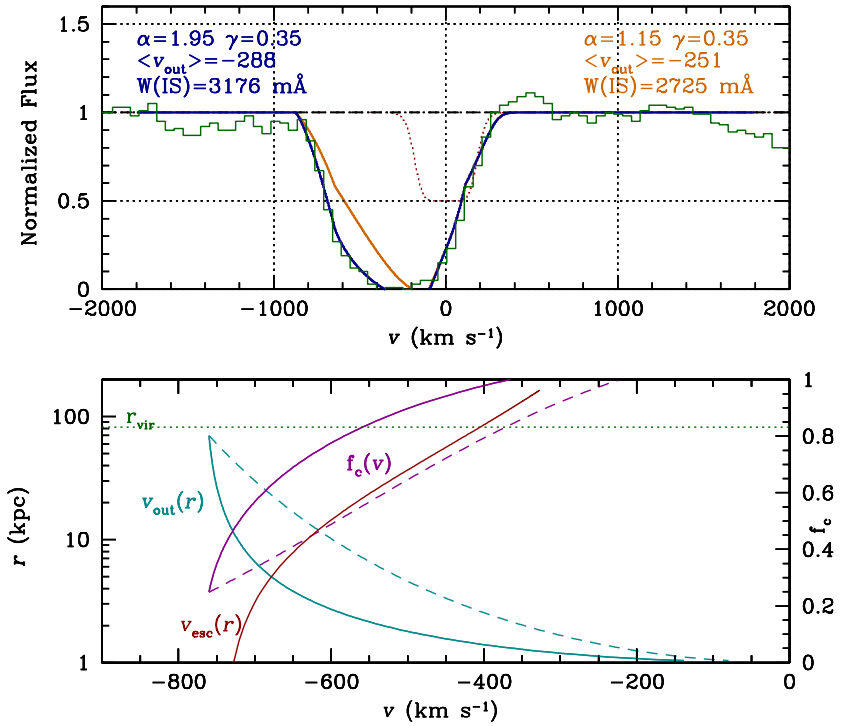

Figure 25. Same as Figure 24, but with increased maximum covering fraction of the outflowing gas $f_{c,\max} = 1$, and a slightly larger covering fraction $f_{c,\max} = 0.5$ for the component at $v = 0$. The cyan and magenta dashed curves in the lower panel refer to the model parameters listed in the upper right of the top panel, while the solid curves of the same colors refer to the model parameters in the upper left. The dark blue model profile shows that for $\gamma = 0.35$, a good match to the observed C II line in the spectrum of the lensed LBG MS1512-cB58 ($R \simeq 1500$, to match Figure 24; see Pettini et al. 2000) is obtained if $\alpha = 1.95$. The orange curve illustrates the change in the model line profile if $\alpha = 1.15$ is assumed instead, with all other parameters held fixed. Clearly, the latter model fails to produce the depth of the absorption at high values of $|v|$. As for the example in Figure 24, the outflow velocity is significantly higher than $v_{\rm esc}$ at the virial radius of the assumed halo.

much physical significance into the inferred values of α needed to fit a particular line profile. For example, the C II line profile in Figure 24 can be well fit a model with the parameters $(\alpha, \gamma) = (1.33, 0.60)$, and that shown in Figure 25 can be equally well fit by the combination $(\alpha, \gamma) = (1.25, 0.20)$.

8. DISCUSSION

8.1. Connection between $b = 0$ and $b \gg 0$ Sightlines

The models discussed above are schematic only, and probably not unique in adequately describing the relatively crude observations. Nevertheless, we have seen that a reasonably successful model for the kinematics and overall geometry of the outflows includes a characteristic asymptotic velocity of $\simeq$700–800 km s^{-1}. Such high velocities are required to explain the shapes of IS absorption line profiles "down the barrel" for $b = 0$ sightlines, as well as the strength of the IS absorption and its relatively shallow dependence on impact parameter for sightlines with $b \geqslant 10$ kpc. This suggests that the absorption at large b is *causally related* to the outflowing material observed at $b = 0$, in which case the gas at large r would most naturally be identified with cool gas carried out in an earlier phase of the current episode of star formation. If this were the case, one might expect the geometry of the metal-enriched gaseous envelope of a galaxy to be time-dependent.

For example, galaxies with spectral morphology similar to that of MS1512-cB58 (and represented by the model shown in Figure 25) tend to be those with estimated stellar population ages (star formation episodes) of $t_{\rm sf} < 100$ Myr (Shapley et al. 2001; Kornei et al. 2010). Even for gas moving at 800 km s^{-1}, reaching $r \sim 100$ kpc requires $\sim$120 Myr, i.e., longer than the inferred duration of the current star formation episode and $\simeq$20% of $t_{\rm sf}$ typical of UV-selected galaxies at $z \simeq 2$–3 (Shapley et al. 2005). Since the inferences about the CGM geometry from the galaxy–galaxy pairs are statistical, and the subset of the pair sample having ancillary information on stellar populations is small, we are not in a position at present for a definitive test. Significant variations in SFR or of the mass flux of outflowing material might also be expected; if star formation were to shut down completely, the corresponding diminution of outflowing gas might eventually be recognized as "gaps" in the CGM near to the galaxy, but lingering high-velocity material at larger radii. Such remnant wind material may have been observed in the spectra of massive post-starburst galaxies at intermediate redshift (Tremonti et al. 2007). At $z \simeq 2$–3, our sample does not currently include galaxies without significant star formation, though it does include some galaxies with small inferred gas fractions and low specific star formation rate SFR/$M*$ (Erb et al. 2006b). Unfortunately, these, too, do not have high enough surface density to have contributed significantly to our galaxy–galaxy pair samples.

One of the expectations of the simple kinematic model outlined above is that most of the absorption seen in the spectrum of a LBG is due to gas located within $\simeq$10 kpc, while most of the absorption observed in offset lines of sight is due to gas that makes a relatively small contribution to the line profile in the $b = 0$ spectra. At large r, because gas giving rise to a particular absorption line transition has lower f_c, the constraints on its velocity from the $b = 0$ line profiles become progressively weaker. This means that there could be lower- or higher-velocity material at large radii and small covering fraction that might go unnoticed compared to material with the same velocity but much smaller galactocentric radius (because it would have a less-diluted f_c).

In this context, it is interesting to consider what is responsible for the "extra" IS absorption in the higher baryonic mass subsample discussed in Section 4 above. It is intriguing that the strength of the $v \sim 0$ components of IS absorption is such a strong function of galaxy mass in both the current sample and in the $z \sim 1.4$ sample of Weiner et al. (2009). A comparison of the highest and lowest stellar mass bins in Table 1 of Weiner et al. (2009) shows that the line strength of the symmetric component increases with stellar mass by a factor of at least 16.6. Weiner et al. (2009) argue that the absorption near $v = 0$ is due primarily to stellar photospheric Mg II absorption. However, the set of far-UV transitions used for our $z \sim 2.3$ sample are not contaminated by significant stellar photospheric absorption, and yet the line profiles exhibit a very similar trend with galaxy mass. We therefore conclude that the "excess" absorption near $v = 0$ arises from IS gas, at least in our $z \sim 2$–3 sample.

There is generally little evidence for infalling (redshifted) gas in the far-UV spectra of the galaxies, and even less evidence that $v(r)$ could be decreasing with increasing r (the line shapes would be very different if this were the case). It would also be difficult to explain the spectral morphology of Lyα emission (see Section 5) if the relationship between $v_{\rm out}$ and r were inverted, as might be expected if stalling winds and/or infall dominated the gas flows. The expected signature of infall as seen in the galaxy spectra is IS absorption velocities redshifted with respect to the galaxy systemic velocity. Such absorption would be expected if gas were prevented from escaping the galaxy potential and eventually began to fall back onto the central regions; a similar signature could also result from "fresh" (rather than recycled) infalling cool gas that is expected to have physical conditions ($T \simeq 10^4$–10^5 K; e.g., Goerdt et al. 2009) very similar to the cool outflowing gas. The absorption line strength for the metallic species we have been able to measure would be relatively insensitive to the metal abundance of infalling material, once again due to the high degree of saturation in the strong IS lines. In other words, the presence of infalling gas should be easily detected in the galaxy spectra (both at $b = 0$ and at large galactocentric radii). Redshifted absorption should be observed in the velocity range $0\,{\rm km\,s^{-1}} \lesssim v \lesssim +300$ km s^{-1} as long as the covering fraction is within a factor of a few of that inferred for outflowing gas. Under the current model, infalling gas should have increasingly redshifted velocities as its covering fraction *increases* (i.e., as r becomes smaller); the expected line profiles would then be inverted with respect to the observations, in the sense that line profiles would be deepest at the high-velocity end of the distribution.

We have discussed evidence from the composite spectra in Section 4 that galaxies with higher baryonic mass are more likely to have stronger absorption at $v \gtrsim 0$, which could possibly be a signature of stalled outflowing material and/or infalling gas. This possibility is discussed further in Section 8.4 below.

8.2. The CGM and Dark Matter Halos

Figure 21 shows that among the strong lines we can measure from the composite galaxy spectra, all except Lyα appear to become much weaker at impact parameters of $b \gtrsim 70$–100 physical kpc even though the rate of decline of $W_0(b)$ (at smaller values of b) varies among the observed lines. It is interesting to ask whether this particular scale has physical significance (as opposed to being an artifact of the limited sensitivity of the data) given that we know something about the properties of the galaxies associated with the extended gas. The particular objects in the present sample, drawn from a spectroscopic survey of "BX" UV-color-selected galaxies, have been well characterized in terms of their spatial clustering (Adelberger et al. 2005b) and stellar population parameters (Erb et al. 2006c; Shapley et al. 2005; Reddy et al. 2005). Conroy et al. (2008) have used the observational results of Adelberger et al. (2005b) to match these $z \simeq 1.9$–2.6 galaxies to dark matter halos in the Millennium simulation (Springel et al. 2005). They find a good match to both the clustering strength and the space density of the "BX" galaxies with dark matter halos having $M_{\rm halo} > 4.2 \times 10^{11}\,M_\odot$ and $\langle M_{\rm halo}\rangle = 9.0 \times 10^{11}\,M_\odot$. If we assume that the dark matter halos "formed" several hundred million years prior to the epoch of their observation (e.g., a galaxy observed at $z \sim 2.4$ might have formed at $z \sim 2.8$ for a typical inferred stellar population age of $\simeq$500 Myr), one can estimate the corresponding virial radius,[24] which is $\sim$64 kpc for the minimum halo mass of $4.2 \times 10^{11}\,M_\odot$ and $\simeq$82 kpc for a halo with the expected average mass of 9×10^{11}. These values of $r_{\rm vir}$ would increase by $\simeq$10%–15% if the "formation" redshift were assumed to be $z = 2.3$ instead. It is possible that the similarity of $r_{\rm vir}$ and the radius at which the W_0 versus b curve begins to steepen for some of the low-ionization absorption lines is not a coincidence. If the clouds are confined by the pressure of a hotter, more diffuse medium, then $r_{\rm vir}$ may be approximately the radius at which the clouds become too diffuse and highly ionized to produce significant columns of low-ionization metals.

By assuming a radial density profile for the characteristic dark matter halo, we can estimate the "escape velocity" $v_{\rm esc}(r)$ from a point at radius r relative to the center of mass. Assuming a Navarro et al. (1997) (NFW) dark matter density profile,

$$\rho_{\rm DM}(r) \propto \frac{1}{(1 + cr/r_{\rm vir})^2\, cr/r_{\rm vir}}, \tag{17}$$

the corresponding escape velocity from radius r is given by

$$v_{\rm esc}^2(r) = \frac{2GM_{\rm vir}}{r} \frac{\ln(1 + cr/r_{\rm vir})}{\ln(1 + c) - c/(1 + c)}, \tag{18}$$

where c is the NFW concentration parameter. Assuming a "formation" redshift of $z = 2.8$, $M_{\rm vir} = 4.2 \times 10^{11}\,M_\odot$, and $r = 1$ kpc, $v_{\rm esc} \simeq 561$ km s^{-1}, while for the expected average halo mass from above, $v_{\rm esc} \simeq 730$ km s^{-1}, both assuming $c = 7$.[25] Perhaps more relevant, the escape velocity for material at $r = r_{\rm vir}$ is significantly lower, $v_{\rm esc} \simeq 310$ km s^{-1} for the minimum mass halo ($r_{\rm vir} = 64$ kpc) and $v_{\rm esc} \simeq 400$ km s^{-1} for the average mass halo ($r_{\rm vir} = 82$ kpc). The lower panels of Figures 24 and 25 show the estimated $v_{\rm esc}$ as a function of r; note that in the context of the model both cases have $v_{\rm out}(r_{\rm vir}) > v_{\rm esc}(r_{\rm vir})$.

8.3. Comparison to Observations at Lower Redshifts

The observed value $|v_{\rm max}| \sim 800$ km s^{-1} so common among the galaxies in the UV-selected samples discussed above suggests that much of the outflowing gas is destined to become unbound from the parent galaxy. One might naturally ask why $v_{\rm max}$ seems to be so consistent within the current $z \sim 2$–3 spectroscopic samples. For halos forming at a given redshift,

[24] Here we are assuming that the virial radius is the radius within which the average halo matter density is $\simeq$178 times higher than the mean density of the universe at the time of initial collapse.

[25] $v_{\rm esc}$ is relatively insensitive to c, changing by $< 10\%$ as c goes from 5 to 9, but is somewhat more sensitive to the value assumed for z_f (e.g., assuming $z_f = 4$ changes the velocities for the same halos above to $v_{\rm esc}(r = 1) \simeq 640$ km s^{-1} and 830 km s^{-1}, respectively).

the expected dependence of $v_{\rm esc}$ on mass is fairly shallow, $v_{\rm esc}(r_{\rm vir}) \propto M_{\rm vir}^{0.3}$. The inferred range of baryonic mass $M_{\rm bar}$ (stars + cold gas) among the "BX" sample at $z \simeq 2$–2.6 is reasonably described by a log-normal distribution with $\log M_{\rm bar} = 10.61 \pm 0.34$ (Erb et al. 2006c); assuming the cosmic baryon-to-dark matter ratio for all of the galaxies, the expected range in $v_{\rm esc}$ among the sample would then be ±25%, which is marginally compatible with the observed consistency of $v_{\rm max}$ among the BX sample of galaxies. Similarly, the range of SFRs among the NIRSPEC Hα sample is SFR $\simeq 30 \pm 15\,M_\odot$ yr^{-1} (Erb et al. 2006b) meaning that if the correlation of $v_{\rm max} \propto {\rm SFR}^{0.25}$ (found by Weiner et al. 2009 for galaxies at $z \sim 1.4$) applied to the $z \sim 2$–3 galaxies, the expected variation of $v_{\rm max}$ would be ±6%, which is indistinguishable from "constant" given the uncertainties in the measurement.

Strickland & Heckman (2009) have emphasized that outflow velocities observed in cool gas entrained in superwind-driven outflows will be significantly smaller than that of the hot "wind fluid," which for M82 they infer to have characteristic velocity of 1400–2200 km s^{-1} based on hard-X-ray observations. The highest velocity observed in cool material (via Hα filaments) in M82 is $v_{\rm out} \simeq 500$–600 km s^{-1}. The typical galaxy in our sample has a bolometric luminosity of $\simeq 3 \times 10^{11}\,L_\odot$, roughly five times higher than that of M82 (cf. Reddy et al. 2006; Sanders et al. 2003). Applying the scaling expected for momentum-driven winds[26] (Murray et al. 2005), $v_{\rm max} \propto L^{0.25}$, by analogy with M82 one would expect the cool component of the outflows for a typical $z \sim 2$–3 galaxy in our sample to reach 750–900 km s^{-1}. This range is clearly consistent with the observations.

8.4. Evidence for "Cold Accretion"?

It is clearly of interest to understand the expected observational signature of the accretion of gas in the context of the proposed schematic model of the CGM. The current models of cold accretion predict characteristic gas temperatures of $\sim(1$–$5) \times 10^4$ K (e.g., Goerdt et al. 2009), which is the same range of temperatures expected for the cool outflowing material seen in absorption against the galaxy far-UV continuum. The bulk of the cool accreting gas is predicted to lie within $\simeq$100 kpc for halos of mass $10^{12}\,M_\odot$. According to Dekel et al. (2009), absorption due to cold stream accretion should have a covering fraction as seen by background sources of $\simeq$25% for 20 kpc $\leqslant r \leqslant$ 100 kpc with $N({\rm H\,I}) > 10^{20}$ cm^{-2}, with infall velocities $\sim$200 km s^{-1}. Along lines of sight with $b \gg 0$, one might expect absorption centered near $v_{\rm los} \simeq 0$ relative to the galaxy systemic redshift (because on average the sightlines should intersect both blueshifted and redshifted IS material), with velocity range of perhaps ±150 km s^{-1}. Sightlines with $b \simeq 0$ (i.e., in the spectra of the galaxies themselves) should intersect inflowing gas with $0 \lesssim v_{\rm los} \lesssim +200$ km s^{-1}.

As mentioned in Section 4.3 above (and illustrated in Figure 11), the "excess" absorption in the composite spectrum of galaxies with $M_{\rm bar} \gtrsim 4 \times 10^{10}\,M_\odot$ may be consistent with both the expected kinematics and optical depth (or covering fraction) for infalling gas. It is notable that the $v_{\rm los} \geqslant 0$ component of absorption is seen in low-ionization species, but not in more highly ionized species such as C IV that are otherwise present over all velocities $v_{\rm los} < 0$ km s^{-1}. This may imply that the gas in the $v_{\rm los} > 0$ kinematic component is more self-shielded than the IS material that contributes most of the observed line equivalent width, suggesting it lies primarily at small r. In any case, even when it is present, a putative infalling IS component cannot account for the observation of strong absorption in both Lyα and metal lines whose strength requires high-velocity dispersion and covering fraction. Nor can accretion explain the observed kinematics of Lyα emission discussed extensively in Section 5. Nevertheless, we *know* that galaxies with halo masses of $\simeq 10^{12}\,M_\odot$ must accrete material in some form over the typical star formation timescale of $\sim$500 Myr in any reasonable hierarchical model; infall of low-metallicity gas may also be necessary for producing the observed mass–metallicity relation at $z \simeq 2$ (e.g., Erb 2008).

Possibly more intriguing than the dominance of outflowing IS material is the observation (both in the present $\langle z \rangle = 2.3$ sample and in the $z \sim 1.4$ sample of Weiner et al. 2009) that galaxies below a threshold in baryonic mass appear to lack the $v_{\rm los} > 0$ IS absorption component. In the $z \sim 2.3$ sample the mass threshold appears to be near $M_{\rm bar} \simeq 4 \times 10^{10}\,M_\odot$, below which essentially all IS absorption is blueshifted. We have seen that the probable range in dark matter halo mass (assuming correspondence between baryonic mass and halo mass) for the lower-$M_{\rm bar}$ half of the Hα sample is $4 \times 10^{11}\,M_\odot \lesssim M_{\rm halo} \lesssim 9 \times 10^{11}\,M_\odot$—a range in mass over which cold accretion is believed to be near its peak at $z \simeq 2$. Paradoxically, the subsample showing possible evidence for an accreting component of cool gas is the half with $M_{\rm halo} \gtrsim 10^{12}\,M_\odot$, i.e., close to the critical mass at which virial shocks begin to prevent cold gas from streaming to the central regions of the galaxy (e.g., Dekel & Birnboim 2006; Ceverino et al. 2010, but see Keres et al. 2009). Lower baryonic mass galaxies with similar SFRs show no evidence for an infalling component with significant covering fraction, at least as compared to that of outflowing material. The extended nature of the galaxies in whose spectra the IS lines are measured provides a spatially averaged IS absorption profile to detect both the coolest regions of inflowing material as well as more highly ionized gas (i.e., having $N({\rm H\,I})$ as low as 10^{14} cm^{-2}) that would present a larger covering fraction. It would be very hard to miss infalling cool gas, which would appear as redshifted absorption for $b = 0$ sightlines. Moreover, sightlines at $b \gg 0$ would produce lines too weak to be consistent with the W_0 versus b results from Section 6 due to the quieter velocity fields expected for infalling material; see Dekel et al. (2009).

With the possible exception of the $v > 0$ absorption in the more massive half of the current sample (which could have alternative explanations; see discussion in Section 2), the observations reveal an absence of evidence supporting cold flow accretion as currently envisioned. It is possible that the streams cover a much smaller fraction of 4π sr than the $\sim$20%–25% estimated from simulations (Goerdt et al. 2009; Dekel & Birnboim 2008) in order to remain undetected by the absorption probes; however, since the absorption line probes are sensitive to H I column densities as low as $N({\rm H\,I}) \lesssim 10^{15}$ cm^{-2}, they would be sensitive to much more than the coolest, most highly collimated regions of the accretion flow. In any case, there seems to be no way to reconcile the observed CGM absorption line strength and kinematics with the results of simulations which seem consistently to predict that accretion of cool gas should be dominant over outflow for galaxies with $M_{\rm tot} \sim 10^{12}\,M_\odot$. Taken at face value, it seems that the importance of cold accretion has been significantly overestimated—or at least that its observational signature must be more subtle than suggested by the early predictions. Of equal concern is that the influence

[26] Murray et al. (2005) point out that cool clouds entrained in a hot flow behave like momentum-driven winds whether the source of the flow is primarily momentum-driven or energy-driven.

of outflows, affecting large regions of the CGM of relatively massive galaxies, seems to have been seriously underestimated; in many cases, outflowing material has been completely ignored or deemed negligible for galaxies in the same mass range as in our sample. There is strong empirical evidence for high-velocity outflows whose influence extends to galactocentric radii of at least 125 kpc around an average galaxy in our sample—roughly the same range of r over which cold accretion is supposed to be most observable. It would clearly be interesting to understand how high-velocity outflows would interact with cool accreting gas in the case where both are occurring simultaneously in the same galaxies and where the relevant physics of both processes have been realistically modeled. At present, the bulk of the observational results do not support the direction in which the theory has been moving—a situation which clearly needs to be resolved.

8.5. Lyα Emission Revisited

In Section 5, we presented a simple one-dimensional model in an effort to understand the kinematics of Lyα emission in the galaxy spectra. The model assumed that the observed blueshifted IS absorption is providing information on the relevant gas-phase kinematics on the "far side" of the galaxy. We showed that the scattering of Lyα photons in circumgalactic gas having large bulk velocities and steep velocity gradients would produce redshifted Lyα emission similar to that observed. A somewhat more physically motivated CGM model was presented in Section 7. The outflowing material is multiphase, where the covering fraction of gas giving rise to a particular transition (rather than the optical depth) versus velocity and galactocentric radius modulates the line profile shapes and the line strength as a function of impact parameter. A more sophisticated model for Lyα emission, including photon diffusion in three-dimensional physical space as well as velocity space (e.g., Laursen & Sommer-Larsen 2007; Verhamme et al. 2008), would be needed for a detailed understanding of the Lyα morphology. Such modeling is beyond the scope of the present work; however, the multiphase gas involved in galaxy-scale outflows is likely to lead, qualitatively, to Lyα kinematics similar to the observations.

As discussed in Section 5, the high velocity and (more importantly) the large velocity range evident from the observed IS absorption lines allow Lyα photons initially produced by recombination in the galaxy H II regions to work their way outward in both real space and velocity space via multiple scattering events. Rather than a shell or a continuous medium of high H I optical depth, the velocity gradient due to the acceleration of the clumpy outflowing gas allows Lyα photons to migrate to larger radii and higher velocities until they are sufficiently redshifted that photons emitted toward an observer can escape the galaxy and its circumgalactic gas. Since we know that the clouds giving rise to low-ionization absorption lines typically extend to at least $r \simeq 70$ kpc, the model we have proposed implies that there should be a diffuse Lyα halo on the same physical scales. The total luminosity in the diffuse halo may, in some cases, represent a significant fraction of the galaxy's production of Lyα, albeit distributed over a projected surface area as much as $\gtrsim$1000 times larger than the galaxy continuum light. Of course, most of this Lyα emission would not be included in the narrow slit typically used for galaxy spectroscopy. It is possible that the diffuse emission has already been observed in very deep Lyα images in the form of Lyα "Blobs" (Steidel et al. 2000; Matsuda et al. 2004)—the most extreme examples—or as diffuse emission evident only after stacking spatial regions surrounding normal LBGs (Hayashino et al. 2004; C. C. Steidel et al. 2010, in preparation).

The main point is that the structure and kinematics of the CGM ultimately control the morphology of escaping Lyα emission, and the Lyα "photosphere" of a galaxy is expected to be roughly coincident with the distribution of gas responsible for the observed IS absorption features. This "prediction" of very extended Lyα halos on scales of ∼50–100 kpc is remarkably similar to recent predictions of cooling Lyα emission associated with cold accretion onto galaxies of very similar mass scale to those in the current sample (Goerdt et al. 2009; Dijkstra & Loeb 2009). Lyα emission is expected to be both redshifted and relatively axisymmetric for Lyα originating in the galaxy and scattering through the CGM, whereas Lyα emission from accreting gas should favor blueshifts and will be concentrated in a few dense filaments. However, it remains unclear how *observationally* distinct the extended Lyα emission arising from these two very different processes will be.

We intend to address these issues in greater detail in a separate paper.

8.6. Outflow Mass Flux and the Gas Content of the CGM

In principle, the type of outflow model described above can be used to estimate the outward mass flux $\dot{M}_{\rm out}$ as well as the total (cool) gas content of the CGM, $M_{\rm CGM}$. Mass outflow rates of cool gas have been estimated for nearby starbursts (e.g., Martin 2005), for rare individual examples of high-redshift galaxies (e.g., Pettini et al. 2000), and for composite spectra of star-forming galaxies at intermediate redshifts (Weiner et al. 2009). In all cases, the mass flux is estimated to be $\dot{M}_{\rm out} \gtrsim \dot{M}_*$ where $\dot{M}_*$ is the galaxy SFR. The calculations generally assume that the outflowing material is in a thin shell located at a galactocentric radius r just beyond the observed stars, traveling with outward velocity given by the centroid of the outflowing component of the IS absorption lines, where the total gas column densities have been estimated from the strength of low-ionization metal absorption lines (for $z < 1.6$) or from the observed N(H I) measured from the Lyα absorption, in the case of MS1512-cB58. The uncertainties in these calculations are very large even in the context of the simple shell model, since they depend on the assumed shell radius as r^2 and the total gas columns are poorly constrained even when N(H I) has been directly measured, due to unknown ionization corrections.

Unfortunately, the less-idealized model introduced above does not necessarily improve the situation; the IS absorption is produced by gas with a large range of both radius and velocity, rather than a shell at a single radius. This means that a galaxy spectrum contains information on the integral absorption along its line of sight, and therefore includes material deposited by both current and past winds. Since the depth of absorption lines is significant out to $R_{\rm eff} \sim 100$ kpc in our outflow model, gas that was launched up to $\gtrsim$100 Myr ago may still contribute to the line profiles, albeit diluted by a decreasing covering fraction with increasing r.

In the context our model, cool gas deposited by outflows to $r \sim 100$ kpc represents an appreciable fraction of the expected $M_{\rm bar,tot} \simeq 1.5 \times 10^{11}\ M_\odot$ associated with a typical dark matter halo mass of $\simeq 9 \times 10^{11}\ M_\odot$. If we assume for definiteness that $R_{\rm eff} \simeq 80$ kpc and that the asymptotic outflow velocity is $v_{\rm out} \simeq 750$ km s^{-1}, a packet of cool gas launched from $r_{\rm min} \sim$ 1–2 kpc will reach $r \simeq 80$ kpc after $t_{80} \sim 1.3 \times 10^8$ yr. If there is a steady-state flow with mass flux $\dot{M}_{\rm out}$, the total cool gas

content within $R_{\rm eff} = 80$ kpc deposited by the outflow would be given approximately by

$$\langle M_{\rm CGM}\rangle = \langle \dot{M}_{\rm out}\rangle t_{80}. \quad (19)$$

The model that best reproduces the radial behavior of f_c for low-ionization species in the CGM of typical galaxies implies cloud densities that increase with galactocentric radius as $\rho_c \propto r^{-2}$ (Section 7.3). If we assume that the initial number density of atoms in a typical cloud is n_0 cm^{-3} at the base of the flow $r_{\rm min}$, then the total cool gas mass between $r_{\rm min} \sim 1$ kpc and $r = 80$ kpc is

$$M_{\rm CGM}(r < 80) \simeq 3 \times 10^{10} n_0\, M_\odot, \quad (20)$$

$$\langle \dot{M}_{\rm out}\rangle \simeq \frac{\langle M_{\rm CGM}\rangle}{t_{80}} \simeq 230 n_0\, M_\odot\ {\rm yr}^{-1}. \quad (21)$$

Note that this estimate does not attempt to account for hot or highly ionized gas that is also likely to be associated with supernova-driven outflows (e.g., Strickland & Heckman 2009).

An estimate of n_0 follows from our earlier assertion that $R_{\rm eff}$ for low-ion species likely corresponds to a threshold $N({\rm H\,I}) \gtrsim 10^{17}$ cm^{-2} (i.e., an LLS). The neutral fraction for such H I column density gas ionized by the metagalactic radiation field is estimated to be $\sim 10^{-3}$ (e.g., Steidel 1990b), so that the total H column will be $\sim 10^{20}$ cm^{-2}. For a line of sight with $b \sim 80$ kpc, the corresponding average density $n_H(80) \sim 4 \times 10^{-4}$ cm^{-3}. In the case of the aforementioned r^{-2} density dependence,

$$n_0 \sim \left[\frac{R_{\rm eff}}{r_{\rm min}}\right]^2 n_H(80) \sim 1\ {\rm cm}^{-3}. \quad (22)$$

Adopting $n_0 = 1$ cm^{-3}, cool gas in the CGM would account for at least 20% of the total baryons associated with a typical galaxy, with mass comparable to the total $M_{\rm bar}$ (cold gas plus stars) in the central few kiloparsecs, which has $\langle M_{\rm bar}\rangle \simeq 4 \times 10^{10}\, M_\odot$ at $z = 2.3$ (Erb et al. 2006c). If one assumes that the typical stellar mass $M_* \simeq 2 \times 10^{10}\, M_\odot$ was formed over the same timescale (i.e., $t_{80} \simeq 1.3 \times 10^8$ yr), then $\langle {\rm SFR}\rangle \simeq 150\, M_\odot$ yr^{-1}. Thus, a crude (but largely independent) calculation yields the same qualitative result obtained with shell models in previous work, i.e., $\dot{M}_{\rm out} \gtrsim \dot{M}_*$.

In any case, it is difficult to escape the conclusion that the CGM contains a substantial fraction of galactic baryons at $z \sim 2$–3, and that the gas-phase kinematics and geometry points to a causal connection between rapid star formation and the presence of large amounts of gas at large galactocentric radius.[27]

9. SUMMARY AND CONCLUSIONS

We have used a relatively large sample of $1.9 \lesssim z \lesssim 2.6$ galaxies with accurate measurements of systemic redshift $z_{\rm sys}$ and reasonably high-quality rest-frame far-UV spectra to examine the relationship between galaxy properties and UV spectral morphology. Our main focus has been on the kinematics and strength of IS absorption and Lyα emission and their implications for the galaxy-scale outflows observed in all rapidly star-forming galaxies at high redshifts. Using this well-observed subset as a calibration, we then combined the rest far-UV galaxy spectra drawn from a much larger parent sample with additional spatial information for the same ensemble of galaxies provided by the spectra of background galaxies with small angular separations. Using these joint constraints, we constructed simple models of the kinematics and geometry of the "CGM"—the interface between star-forming galaxies and the IGM. Our principal conclusions are as follows.

1. We have used the Hα sample of $z \simeq 2$–2.6 galaxies together with their far-UV spectra to produce a revised calibration that allows deriving systemic redshifts for star-forming galaxies from their far-UV spectral features (strong IS lines and Lyα emission). In the absence of stellar photospheric absorption lines or nebular emission lines in the rest-frame optical, the most accurate estimates of the systemic redshift are derived from the centroids of strong IS absorption lines. Applying a shift of $\Delta v = +165$ km s^{-1} ($\Delta z = +0.0018$) at $z = 2.3$ to a measured absorption redshift provides an estimate of a galaxy's systemic redshift accurate to ± 125 km s^{-1}; redshifts measured from the Hα emission line (when available) have a precision of ± 60 km s^{-1}. Both methods for estimating redshifts have no significant systematic offset relative to the redshift defined by stellar (photospheric) absorption features.
2. Using only the Hα sample of BX galaxies, we found mean velocity offsets for the centroids of the strong IS lines and Lyα emission line of $\Delta v_{\rm IS} = -164 \pm 16$ km s^{-1} and $\Delta v_{{\rm Ly}\alpha} = +445 \pm 27$ km s^{-1}, respectively. We searched for significant correlations between the kinematics defined by the centroid velocities of IS and Lyα lines and other measured or inferred galaxy properties. Within the Hα sample, the only significant correlations found were between $\Delta v_{\rm IS}$ and galaxy mass estimated from the sum of inferred stellar and gas mass ($M_{\rm bar}$) as well as the independently estimated $M_{\rm dyn}$. The sense of the correlation is that $\Delta v_{\rm IS}$ is smaller (i.e., less blueshifted) in galaxies with larger masses.
3. Despite the trend described in point (2) above, the velocity $|v_{\rm max}|$ of the maximum blueshift observed in the absorption profiles is essentially identical for the subsamples of galaxies with $M_{\rm bar} > 3.7 \times 10^{10}\, M_\odot$ and $M_{\rm bar} < 3.7 \times 10^{10}\, M_\odot$, with $|v_{\rm max}| \simeq 800$ km s^{-1}. However, the higher-mass subset has both $\Delta v_{\rm IS}$ and $\Delta v_{{\rm Ly}\alpha}$ shifted toward positive velocities (i.e., more redshifted) by ~ 200 km s^{-1}. The differences in the composite IS and Lyα profiles can be explained by an additional component of absorption at $v \gtrsim 0$ that appears to be absent in the lower-mass subsample. The extra absorption, which has a peak near $v = 0$ and a centroid velocity of $v \simeq +150$ km s^{-1}, could conceivably be a signature of infalling gas or stalled winds falling back on the galaxy, but is most likely to be gas at small galactocentric radii based on the line profiles. In any case, the velocity centroids of the IS lines, which are commonly used as a proxy for the "wind velocity" for high-redshift galaxy samples, are actually modulated almost entirely by gas that is not outflowing.
4. The Lyα emission profile, like $\langle \Delta v_{\rm IS}\rangle$, is modulated by the covering fraction (or apparent optical depth) of material near $v \simeq 0$. We show that, by using the information on the covering fraction near $v \simeq 0$, the kinematics of blueshifted gas, and assuming spherical symmetry, the behavior of Lyα emission with respect to IS absorption can be reproduced using simple models. In general, the red wing of Lyα emission is produced by Lyα photons scattered from outflowing gas on the opposite side of the galaxy. The apparent redshift of the Lyα centroid is a manifestation of the fact that only photons scattering from material having a (redshifted) velocity large enough to take the photons off the

[27] See Ménard et al. (2009) for additional support for this causal connection.

Lyα resonance for any material between the last scattering and the observer can escape in the observer's direction. The spectral morphologies of Lyα emission and IS absorption are most easily understood if the highest-velocity material (either redshifted or blueshifted) is located at the largest distances from the galaxy, i.e., that $v(r)$ is monotonically increasing with r in a (roughly) spherically symmetric radial flow. The same geometric picture works well to reproduce both the line-of-sight ($b = 0$) absorption profiles and the absorption line strength as a function of impact parameter (see point (6) below).

5. We have demonstrated that the use of the far-UV spectra of galaxies within projected angular pairs (with discrepant redshifts) provides an opportunity to constrain the physical location of circumgalactic gas around typical galaxies. A set of 512 such galaxy pairs, on angular scales ranging from $1''$ to $15''$ ($\simeq$8–125 kpc), have been combined with the $b = 0$ spectra of the foreground galaxies in each pair. These are used together to measure each foreground galaxy's CGM along two independent lines of sight. Composite spectra stacked according to galactocentric impact parameter allow us to measure the dependence of the line strength of several ionic species on impact parameter b from 0 to 125 kpc (physical). These lines are strongly saturated, so their strength is determined by a combination of the covering fraction and the velocity spread in the absorbing gas. The falloff of W_0 with b implies $f_c(r) \propto r^{-\gamma}$, with $0.2 \leqslant \gamma \leqslant 0.6$, with Ly$\alpha$ and C IV having smaller values of γ compared to, e.g., Si II and Si IV. For each observed species, the strength of absorption declines much more rapidly beginning at $b \simeq$ 70–90 kpc, with the exception of Lyα which remains strong to $b \simeq 250$ kpc. Combining the known space density of the galaxies in our sample (i.e., including only those with apparent magnitude $\mathcal{R} \leqslant 25.5$) with the average cross section for absorption accounts for $\simeq$45% of all intergalactic C IV absorption with $W_0(1548) > 0.15$ Å and $\simeq$70% of LLSs at $z \sim 2$ observed along QSO sightlines.
6. We have proposed a simple model constrained by a combination of $W_0(b)$ from the galaxy pairs and the kinematics of IS species observed toward each galaxy's own stars ($b = 0$). The IS absorption line shapes depend on a combination of $v_{\rm out}(r)$, the radial dependence of outflow velocity which in turn depends on the cloud acceleration $a(r)$ and $f_c(r, v)$, the radial dependence of the covering fraction, which depends on cloud geometry and is inferred from $W_0(b)$. We show that a self-consistent model using parameterized forms of $a(r)$ and $f_c(r)$ can simultaneously reproduce the observed line shapes and strengths (apparent optical depth versus velocity) as well as the observed $W_0(b)$ relation from the galaxy–galaxy pair measurements. In the model, higher-velocity gas is located at larger galactocentric radii, and gas clouds are accelerated to $\simeq$800 km s^{-1} before the absorption strength (i.e., covering fraction) is geometrically diluted. There is little evidence in the line profiles for stalling or infalling wind material, and the transverse sightlines show metal-enriched gas to at least $\sim$125 kpc.[28] Taken together, these suggest that high-velocity outflows from $\simeq L^*$ galaxies at $z \sim$ 2–3 are able to deposit enriched material to very large radii. They also suggest that the observed metals are causally related to the observed galaxies, rather than remnants of winds generated by other (earlier) galaxies deposited in the nearby volume.
7. The observed $v_{\rm max} \simeq$ 800 km s^{-1} that appears to be a general property of the galaxies in our spectroscopic sample exceeds $v_{\rm esc}(r_{\rm vir})$ estimated for galaxy halo masses of $\simeq 9 \times 10^{11}\,M_\odot$, the average halo mass expected given the observed space density and clustering of the $z \simeq 2$ galaxies. Similarly, the galactocentric radius at which the strength of low-ionization absorption line species begins to decrease rapidly is similar to the estimated virial radius of $\simeq$80 kpc for the same halo mass.
8. We consider the observations in the context of "cold accretion" or "cold flows," which are believed to be active over the same range of galactocentric radii and redshifts, for galaxies in the same range of total mass as those in our sample ($4 \times 10^{11}\,M_\odot \lesssim M_{\rm tot} \lesssim 2 \times 10^{12}\,M_\odot$). There is possible evidence for the presence of infalling gas in the far-UV spectra of galaxies with greater than the median baryonic mass $M_{\rm bar} = 4 \times 10^{10}\,M_\odot$, while the lower-mass subsample shows no evidence for the expected redshifted components of IS absorption lines. The kinematics of Lyα emission also seem inconsistent with the expectations for accreting material, while they are as expected in the context of the picture of outflows we have presented. We expect that the same gas seen in absorption to $b \simeq$ 50–100 kpc also acts as a scattering medium for escaping Lyα photons initially produced in the galaxy H II regions. These Lyα "halos" are probably a generic property of all high-redshift LBG-like galaxies, the more extreme of which have probably already been observed as "Lyα Blobs" (Steidel et al. 2000; Matsuda et al. 2004). More typical LBGs likely exhibit this diffuse Lyα emission, which is of low surface brightness and therefore difficult to observe without extremely deep Lyα images.
9. The inferred mass of cool gas in the CGM (within $\sim$100 kpc) is comparable to the sum of cold gas and stars in the inner few kpc; together they account for $\gtrsim$50% of the total baryonic mass ($\sim 1.5 \times 10^{11}\,M_\odot$) associated with the average $M \sim 9 \times 10^{11}\,M_\odot$ dark matter halo. If the qualitative picture of the CGM we have proposed is correct, the wind material would still be traveling at $v_{\rm out} > v_{\rm esc}(r_{\rm vir})$ when it crosses the virial radius at $r \simeq$ 80 kpc. Even if $v_{\rm out} \simeq v_{\rm esc}$, the low-ionization wind material would reach $r \sim$ 100 kpc within $\sim$150 Myr of the onset of the star formation episode if it is slowed only by gravity and does not accumulate a large amount of swept-up ISM on its way. Since we have shown that the CGM is outflowing and itself comprises a large baryonic reservoir, it is possible that in most directions there is little to impede outflows from propagating ballistically into the IGM.

The use of resolved background sources for studying the CGM in absorption is qualitatively different from using QSO sightlines. It seems clear that the multiphase ISM observable in a number of ionic species indicates differential changes in covering fraction of the outflowing gas as a function of ionization level. This means that the radial behavior of the strength of saturated transitions is providing information on the "phase-space" density of gas having physical conditions amenable to the presence of each ion. Because absorption seen in the spectra of background *galaxies* averages over a $\simeq$2–3 kpc region, as compared to background QSOs, whose apparent

[28] Adelberger et al. (2003, 2005b) have argued that there is evidence that the metals affect regions of $\simeq$300 kpc (proper) based on C IV–galaxy cross-correlation, and that outflows would be expected to stall at approximately this distance due to a number of separate considerations.

angular sizes are ≃5 orders of magnitude smaller, statistics such as IS line strength, covering fraction, and velocity range versus impact parameter, are much less subject to large variance along a single sightline.

All of the galaxy spectra used in this paper were obtained as part of large surveys, and therefore have low-to-moderate spectral resolution and S/N. It is possible with current generation telescopes and instruments to obtain spectra of relatively high S/N and moderate resolution (e.g., Shapley et al. 2006) in 10–20 hr integration time (i.e., ∼10 times longer than most in the current samples). However, spectra similar to those currently possible only for strongly lensed galaxies ($R \sim 5000$, S/N $\gtrsim 30$) will be routine at $\mathcal{R} \simeq 24$–24.5 using future 30 m class telescopes equipped with state of the art multiobject spectrometers (Steidel et al. 2009). When such capability is realized, full observational access to the three-dimensional distribution of gas near to and between galaxies will revolutionize the study of baryonic processes in the context of galaxy formation. The results described above are intended as an illustration of the application of rest-far-UV galaxy spectra toward a better understanding of feedback processes and the CGM/IGM interface with the sites of galaxy formation. The feasibility of sharpening our understanding and interpretation with higher-quality data in the future is very encouraging.

This work has been supported by the US National Science Foundation through grants AST-0606912 and AST-0908805 (C.C.S.), and by the David and Lucile Packard Foundation (A.E.S., C.C.S.). C.C.S. acknowledges additional support from the John D. and Catherine T. MacArthur Foundation. D.K.E. is supported by the National Aeronautics and Space Administration under Award No. NAS7-03001 and the California Institute of Technology. We thank Juna Kollmeier and Joop Schaye for interesting and useful conversations, and Patrick Hall, Martin Haehnelt, and the referee for comments that significantly improved the final version of the paper. Kurt Adelberger played a major role in the early days of the survey used in this paper; his intellectual contributions have remained crucial though he has moved on to new challenges in the "real" world. Marc Kassis and the rest of the W. M. Keck Observatory staff keep the instruments and telescopes running effectively, for which we are extremely grateful. We extend thanks to those of Hawaiian ancestry on whose sacred mountain we are privileged to be guests.

REFERENCES

Adelberger, K. L., Shapley, A. E., Steidel, C. C., Pettini, M., Erb, D. K., & Reddy, N. A. 2005a, ApJ, 629, 636
Adelberger, K. L., & Steidel, C. C. 2000, ApJ, 544, 218
Adelberger, K. L., Steidel, C. C., Pettini, M., Shapley, A. E., Reddy, N. A., & Erb, D. K. 2005b, ApJ, 619, 697
Adelberger, K. L., Steidel, C. C., Shapley, A. E., Hunt, M. P., Erb, D. K., Reddy, N. A., & Pettini, M. 2004, ApJ, 607, 226
Adelberger, K. L., Steidel, C. C., Shapley, A. E., & Pettini, M. 2003, ApJ, 584, 45
Bergeron, J., & Boissé, P. 1991, A&A, 243, 344
Bouché, N., Murphy, M. T., Péroux, C., Davies, R., Eisenhauer, F., Förster Schreiber, N. M., & Tacconi, L. 2007, ApJ, 669, L5
Bowen, D. V., Blades, J. C., & Pettini, M. 1995, ApJ, 448, 634
Brooks, A. M., Governato, F., Quinn, T., Brook, C. B., & Wadsley, J. 2009, ApJ, 694, 396
Ceverino, D., Dekel, A., & Bournaud, F. 2010, MNRAS, 404, 2151
Charlot, S., & Fall, S. M. 1991, ApJ, 378, 471
Chen, H., Lanzetta, K. M., Webb, J. K., & Barcons, X. 2001, ApJ, 559, 654
Chen, Y., Tremonti, C. A., Heckman, T. M., Kauffmann, G., Weiner, B. J., Brinchmann, J., & Wang, J. 2010, arXiv:1003.5425
Colina, L., Arribas, S., & Monreal-Ibero, A. 2005, ApJ, 621, 725
Conroy, C., Shapley, A. E., Tinker, J. L., Santos, M. R., & Lemson, G. 2008, ApJ, 679, 1192
Danforth, C. W., & Shull, J. M. 2008, ApJ, 679, 194
Dekel, A., & Birnboim, Y. 2006, MNRAS, 368, 2
Dekel, A., & Birnboim, Y. 2008, MNRAS, 383, 119
Dekel, A., et al. 2009, Nature, 457, 451
Dijkstra, M., Haiman, Z., & Spaans, M. 2006a, ApJ, 649, 14
Dijkstra, M., Haiman, Z., & Spaans, M. 2006b, ApJ, 649, 37
Dijkstra, M., & Loeb, A. 2009, MNRAS, 400, 1109
Ellison, S. L., Ibata, R., Pettini, M., Lewis, G. F., Aracil, B., Petitjean, P., & Srianand, R. 2004, A&A, 414, 79
Erb, D. K. 2008, ApJ, 674, 151
Erb, D. K., Shapley, A. E., Pettini, M., Steidel, C. C., Reddy, N. A., & Adelberger, K. L. 2006a, ApJ, 644, 813
Erb, D. K., Shapley, A. E., Steidel, C. C., Pettini, M., Adelberger, K. L., Hunt, M. P., Moorwood, A. F. M., & Cuby, J. 2003, ApJ, 591, 101
Erb, D. K., Steidel, C. C., Shapley, A. E., Pettini, M., Reddy, N. A., & Adelberger, K. L. 2006b, ApJ, 647, 128
Erb, D. K., Steidel, C. C., Shapley, A. E., Pettini, M., Reddy, N. A., & Adelberger, K. L. 2006c, ApJ, 646, 107
Ferrara, A. 2003, Ap&SS, 284, 415
Förster Schreiber, N. M., et al. 2006, ApJ, 645, 1062
Franx, M., Illingworth, G. D., Kelson, D. D., van Dokkum, P. G., & Tran, K.-V. 1997, ApJ, 486, L75
Furlanetto, S. R., Schaye, J., Springel, V., & Hernquist, L. 2005, ApJ, 622, 7
Goerdt, T., Dekel, A., Sternberg, A., Ceverino, D., Teyssier, R., & Primack, J. R. 2009, arXiv:0911.5566
Grimes, J. P., et al. 2009, ApJS, 181, 272
Haiman, Z., Spaans, M., & Quataert, E. 2000, ApJ, 537, L5
Hansen, M., & Oh, S. P. 2006, MNRAS, 367, 979
Hayashino, T., et al. 2004, AJ, 128, 2073
Heckman, T. M., Armus, L., & Miley, G. K. 1990, ApJS, 74, 833
Kacprzak, G. G., Churchill, C. W., Ceverino, D., Steidel, C. C., Klypin, A., & Murphy, M. T. 2010, ApJ, 711, 533
Kennicutt, R. C. 1998, ApJ, 498, 541
Kereš, D., Katz, N., Fardal, M., Davé, R., & Weinberg, D. H. 2009, MNRAS, 395, 160
Kereš, D., Katz, N., Weinberg, D. H., & Davé, R. 2005, MNRAS, 363, 2
Kornei, K. A., Shapley, A. E., Erb, D. K., Steidel, C. C., Reddy, N. A., Pettini, M., & Bogosavljevic, M. 2010, ApJ, 711, 693
Lanzetta, K. M., Bowen, D. V., Tytler, D., & Webb, J. K. 1995, ApJ, 442, 538
Laursen, P., & Sommer-Larsen, J. 2007, ApJ, 657, L69
Law, D. R., Steidel, C. C., Erb, D. K., Larkin, J. E., Pettini, M., Shapley, A. E., & Wright, S. A. 2009, ApJ, 697, 2057
Lehnert, M. D., & Heckman, T. M. 1996, ApJ, 472, 546
Lehnert, M. D., Heckman, T. M., & Weaver, K. A. 1999, ApJ, 523, 575
Madau, P., Ferrara, A., & Rees, M. J. 2001, ApJ, 555, 92
Martin, C. L. 1999, ApJ, 513, 156
Martin, C. L. 2005, ApJ, 621, 227
Martin, C. L., & Bouché, N. 2009, ApJ, 703, 1394
Mas-Hesse, J. M., Kunth, D., Tenorio-Tagle, G., Leitherer, C., Terlevich, R. J., & Terlevich, E. 2003, ApJ, 598, 858
Matsuda, Y., et al. 2004, AJ, 128, 569
McLean, I. S., et al. 1998, Proc. SPIE, 3354, 566
Ménard, B., Wild, V., Nestor, D., Quider, A., & Zibetti, S. 2009, arXiv:0912.3263
Mori, M., Ferrara, A., & Madau, P. 2002, ApJ, 571, 40
Murray, N., Quataert, E., & Thompson, T. A. 2005, ApJ, 618, 569
Navarro, J. F., Frenk, C. S., & White, S. D. M. 1997, ApJ, 490, 493
Neufeld, D. A. 1991, ApJ, 370, L85
Pettini, M., Rix, S. A., Steidel, C. C., Adelberger, K. L., Hunt, M. P., & Shapley, A. E. 2002, ApJ, 569, 742
Pettini, M., Shapley, A. E., Steidel, C. C., Cuby, J., Dickinson, M., Moorwood, A. F. M., Adelberger, K. L., & Giavalisco, M. 2001, ApJ, 554, 981
Pettini, M., Steidel, C. C., Adelberger, K. L., Dickinson, M., & Giavalisco, M. 2000, ApJ, 528, 96
Quider, A. M., Pettini, M., Shapley, A. E., & Steidel, C. C. 2009, MNRAS, 398, 1263
Quider, A. M., Shapley, A. E., Pettini, M., Steidel, C. C., & Stark, D. P. 2010, MNRAS, 402, 1467
Rauch, M., Sargent, W. L. W., & Barlow, T. A. 1999, ApJ, 515, 500
Rauch, M., Sargent, W. L. W., & Barlow, T. A. 2001, ApJ, 554, 823
Reddy, N. A., Erb, D. K., Steidel, C. C., Shapley, A. E., Adelberger, K. L., & Pettini, M. 2005, ApJ, 633, 748
Reddy, N. A., & Steidel, C. C. 2009, ApJ, 692, 778

Reddy, N. A., Steidel, C. C., Fadda, D., Yan, L., Pettini, M., Shapley, A. E., Erb, D. K., & Adelberger, K. L. 2006, ApJ, 644, 792
Reddy, N. A., Steidel, C. C., Pettini, M., Adelberger, K. L., Shapley, A. E., Erb, D. K., & Dickinson, M. 2008, ApJS, 175, 48
Rupke, D. S., Veilleux, S., & Sanders, D. B. 2005, ApJS, 160, 115
Sanders, D. B., Mazzarella, J. M., Kim, D., Surace, J. A., & Soifer, B. T. 2003, AJ, 126, 1607
Sargent, W. L. W., Boksenberg, A., & Steidel, C. C. 1988, ApJS, 68, 539
Scannapieco, E., Ferrara, A., & Madau, P. 2002, ApJ, 574, 590
Schaerer, D., & Verhamme, A. 2008, A&A, 480, 369
Schaye, J., Carswell, R. F., & Kim, T. 2007, MNRAS, 379, 1169
Schwartz, C. M., Martin, C. L., Chandar, R., Leitherer, C., Heckman, T. M., & Oey, M. S. 2006, ApJ, 646, 858
Shapley, A. E., Steidel, C. C., Adelberger, K. L., Dickinson, M., Giavalisco, M., & Pettini, M. 2001, ApJ, 562, 95
Shapley, A. E., Steidel, C. C., Erb, D. K., Reddy, N. A., Adelberger, K. L., Pettini, M., Barmby, P., & Huang, J. 2005, ApJ, 626, 698
Shapley, A. E., Steidel, C. C., Pettini, M., & Adelberger, K. L. 2003, ApJ, 588, 65
Shapley, A. E., Steidel, C. C., Pettini, M., Adelberger, K. L., & Erb, D. K. 2006, ApJ, 651, 688
Springel, V., et al. 2005, Nature, 435, 629
Steidel, C. C. 1990a, ApJS, 72, 1
Steidel, C. C. 1990b, ApJS, 74, 37
Steidel, C. C. 1992, PASP, 104, 843
Steidel, C. C., Adelberger, K. L., Shapley, A. E., Pettini, M., Dickinson, M., & Giavalisco, M. 2000, ApJ, 532, 170
Steidel, C. C., Adelberger, K. L., Shapley, A. E., Pettini, M., Dickinson, M., & Giavalisco, M. 2003, ApJ, 592, 728
Steidel, C. C., Dickinson, M., & Persson, S. E. 1994, ApJ, 437, L75
Steidel, C. C., Giavalisco, M., Pettini, M., Dickinson, M., & Adelberger, K. L. 1996, ApJ, 462, L17
Steidel, C. C., Kollmeier, J. A., Shapley, A. E., Churchill, C. W., Dickinson, M., & Pettini, M. 2002, ApJ, 570, 526
Steidel, C. C., Martin, C., Prochaska, J. X., Pettini, M., Schaye, J., & Rakic, O. 2009, Astro2010: Astron. Astrophys. Decadal Survey, 286
Steidel, C. C., Pettini, M., & Adelberger, K. L. 2001, ApJ, 546, 665
Steidel, C. C., & Sargent, W. L. W. 1992, ApJS, 80, 1
Steidel, C. C., Shapley, A. E., Pettini, M., Adelberger, K. L., Erb, D. K., Reddy, N. A., & Hunt, M. P. 2004, ApJ, 604, 534
Strickland, D. K., & Heckman, T. M. 2009, ApJ, 697, 2030
Strickland, D. K., Heckman, T. M., Colbert, E. J. M., Hoopes, C. G., & Weaver, K. A. 2004, ApJ, 606, 829
Tremonti, C. A., Moustakas, J., & Diamond-Stanic, A. M. 2007, ApJ, 663, L77
Verhamme, A., Schaerer, D., Atek, H., & Tapken, C. 2008, A&A, 491, 89
Verhamme, A., Schaerer, D., & Maselli, A. 2006, A&A, 460, 397
Weiner, B. J., et al. 2009, ApJ, 692, 187
Zheng, Z., & Miralda-Escudé, J. 2002, ApJ, 578, 33